# Rydberg Ions in Motion

## Dissertation

Zur Erlangung des akademischen Grades
*Doktor der Naturwissenschaften*

am Fachbereich Physik, Mathematik und Informatik
der Johannes Gutenberg-Universität in Mainz

vorgelegt von
**Jonas Vogel**
geboren am 01.08.1992 in Köln

Mainz, Dezember 2021

1. Gutachter und Betreuer: Prof. Dr. Ferdinand Schmidt-Kaler
2. Gutachter: Prof. Dr. Niklaus Berger

# Abstract

Cold controlled atoms and ions are currently of great interest for applications in quantum information processing, simulation and sensing. Excitation of trapped ions to their Rydberg states offers a unique opportunity for combining advantages of precisely controllable trapped ions with long-range and tunable Rydberg interactions. Intrinsically large polarizabilities of Rydberg states result in enhanced electric field sensitivity and consequently altered trap frequencies as compared to electronically low-lying states. I studied this with experiments on a single $^{40}\mathrm{Ca}^+$ ion or ion crystals in a linear Paul trap. Energy shifts through occupation of phonon modes of the three dimensional harmonic oscillator are considered in a lineshape model for the Rydberg excitation spectrum and allow for a discussion of transition shifts and broadening as a function of principal quantum numbers between $n \in [38, 65]$. Moreover, phonon distributions for different harmonic oscillator modes can be shaped by the ion temperature and the confining fields. An external radio frequency field can excite the ion into a coherent motional state with $|\alpha| < 11$ and average phonon numbers $\bar{k} < 121$, which leads to a shift in transition frequency and allows to extract the polarizability of Rydberg states $49\mathrm{S}_{1/2}, 53\mathrm{S}_{1/2}$ and $57\mathrm{S}_{1/2}$, in full agreement with literature. Similarly, coherent states of motion in a two-ion crystal can be used to generate entanglement by utilizing state-dependent trap frequencies of Rydberg ions, as the ion crystal accumulates a phase in a displaced harmonic oscillator potential dependent on the initial confinement. This thesis proposes a two-ion entanglement operation by displacing the ion crystal for 1.8 µs with a field pulse of 29 V/m, readily achieved in current ion traps, where the operation speed might be further improved by use of optimized control pulses and additional displacements. Finally, the distance-dependent Van-der-Waals interaction of Rydberg ions within a four-ion crystal is studied, for that I propose to observe the excitation energy of two ions directly neighboring compared to two separated Rydberg ions. For ion crystals at finite temperature, I investigate site-dependent Rabi frequencies and site-dependent coupling to different harmonic oscillator motions, that lead to broadening of the excitation spectra and a reduction in contrast for detection of Van-der-Waals sensitive basis states. The presented experiments pave the road to the overarching goal of incorporating Rydberg excitations into the toolbox of quantum computing with trapped ions.

# Zusammenfassung

Kalte, kontrollierte Atome und Ionen sind derzeit von großem Interesse für Anwendungen in der Quanteninformationsverarbeitung, -simulation und -sensorik. Die Anregung von gefangenen Ionen in Rydberg-Zustände bietet eine einzigartige Möglichkeit, die Vorteile von präzise kontrollierbaren gefangenen Ionen mit weitreichenden, verstimmbaren Rydberg-Wechselwirkungen zu kombinieren. Die intrinsisch große Polarisierbarkeit von Rydberg-Zuständen führt zu einer erhöhten Empfindlichkeit gegenüber elektrischen Feldern und folglich zu unterschiedlichen Fallenfrequenzen im Vergleich zu elektronisch niedrig angeregten Zuständen. Ich untersuche die Polarisierbarkeiten experimentell an einzelnen $^{40}\mathrm{Ca}^+$-Ionen und Ionenkristallen in einer linearen Paul-Falle. Energieverschiebungen durch Besetzung des harmonischen Oszillators werden in einem Linienmodell für das Rydberg-Anregungsspektrum betrachtet und erlauben eine Diskussion von Übergangsverschiebungen und Verbreiterungen als Funktion der Hauptquantenzahl zwischen $n \in [38, 65]$, Phononenverteilungen und Feldgradienten. Durch Anlegen eines externen Hochfrequenzfeldes werden kohärente Bewegungszustände mit $|\alpha| < 11$ und durchschnittlichen Phononenzahlen $\tilde{k} < 121$ angeregt, und die resultierende Verschiebung der Übergangsfrequenz ermöglicht die Extraktion der Polarisierbarkeiten für die Rydberg-Zustände $49\mathrm{S}_{1/2}, 53\mathrm{S}_{1/2}$ und $57\mathrm{S}_{1/2}$ in voller Übereinstimmung mit der Literatur. Ähnlich können kohärente Bewegungszustände in einem Zwei-Ionen-Kristall zur Erzeugung von Verschränkung genutzt werden, da die akkumulierte Phase abhängig vom Einschluss in der Paul-Falle ist. Hier wird eine Verschränkungsoperation vorgeschlagen, bei welcher der Ionenkristall für 1.8 µs mit einem externen Feld von 29 V/m verschoben wird - erreichbar in aktuellen Ionenfallen - wobei die Dauer durch optimierte Feldpulse und zusätzliche Auslenkungen verringert werden kann. Außerdem schlage ich vor, die abstandsabhängige Van-der-Waals-Wechselwirkung von Rydberg-Ionen zu beobachten, welche die Anregungsenergie von zwei angrenzenden Ionen im Vergleich zu zwei getrennten Ionen verschiebt. Für Ionenkristalle bei endlicher Temperatur untersuche ich positionsabhängige Rabi-Frequenzen und Kopplung an die Oszillatorbewegungen, die zu einer Verbreiterung der Übergangsspektren und einer Verringerung der Nachweisempfindlichkeit für Van-der-Waals-Kräfte führen. Das übergreifende Ziel ist es, Rydberg-Anregung in die Quanteninformationsverarbeitung mit gefangen Ionen aufzunehmen.

# Contents

1 **Introduction** **3**

2 **Highly Polarizable Ion in Electric Fields** **7**
- 2.1 Rydberg Ions Confined in a Harmonic Paul Trap . . . . . . . . . . . . 8
- 2.2 Strong Interactions and Relevant Properties of Rydberg States . . . . 15
- 2.3 Excitation of Internal and External Degrees of Freedom . . . . . . . . 22

3 **The Experimental Apparatus** **29**
- 3.1 A Trap for Stable Rydberg Ions . . . . . . . . . . . . . . . . . . . . . . . . 29
- 3.2 Laser Sources for Electronic State Manipulation . . . . . . . . . . . . . 34

4 **Excitation of Rydberg States** **43**
- 4.1 Control of External and Internal Fields . . . . . . . . . . . . . . . . . . 44
- 4.2 Rydberg Excitation Lineshapes in the Presence of Ionic Motion . . . . 50
- 4.3 Towards Fast Rydberg Excitation . . . . . . . . . . . . . . . . . . . . . . 61

5 **Motional Excitation for Quantum Sensing** **67**
- 5.1 Coherent States and Rydberg Excitation of Strongly Oscillating Ions . 68
- 5.2 Determination of the Ion's Polarizability by Enlarging the Wave Packet 74

6 **Fast Motional Excitation for Quantum Computing** **79**
- 6.1 Displacement of Two Ions by a Fast Electric Kick . . . . . . . . . . . . 80
- 6.2 Phase Accumulation and State-Dependent Forces for Entanglement Generation . . . . . . . . . . . . . . . . . . . . . . . . . . . . . . . . . . . . . 85
- 6.3 Entanglement Error and Experimental Challenges . . . . . . . . . . . 92

7 **Van-der-Waals Forces between Trapped Rydberg Ions** **97**
- 7.1 Coulomb Crystals Interacting with a Laser . . . . . . . . . . . . . . . 98
- 7.2 Search for Correlated Quantum Jumps . . . . . . . . . . . . . . . . . . 102
- 7.3 Rydberg Excitation of Linear Ion Strings . . . . . . . . . . . . . . . . 109
- 7.4 Sensitivity for Measurements of Distance-Dependent Forces between Rydberg Ions . . . . . . . . . . . . . . . . . . . . . . . . . . . . . . . . . 114

8 **Outlook** **121**

**Bibliography** **129**

# 1

# Introduction

*Rydberg Ions in Motion* - A short, but accurate description of the content of this thesis. Ions oscillating in the harmonic potential of a Paul trap and excited to Rydberg states, experience a coupling of their motion to the electronic state and allow for the observation of rich physics, e.g. huge polarizabilities, long-range interactions and entanglement generation [Mü08]. The following section discusses and highlights research, that relates to this thesis or shows great advancement within the topic of Rydberg physics or trapped ions.

In the beginning, Rydberg atoms are introduced as a promising platform for quantum computation and simulation due to the long-range interactions for high principal quantum numbers. Trapped ions, however, are already widely used for quantum computing, due to the natural interactions mediated by the Coulomb force, and will be briefly discussed, before prospects for the combination of these two platforms are given. Finally, an outline of this thesis is presented.

## Rydberg Atoms

Rydberg states are highly excited electronic states of atoms, where the valence electron obtains an energy close to the ionization threshold, such that properties of Rydberg atoms are exaggerated compared to electronically low-lying states. The extension of the atomic wave function of a Rydberg state can reach orders of µm for high principal quantum numbers [Gal94]. Thereby, individual Rydberg atoms are very susceptible to electric fields and can be used as accurate field sensors [Ost99, Fac16]. The large extension of the wave function and consequent charge separation of valence electron and ionic core, leads to strong dipole-dipole interactions depending on the distance between the highly excited atoms. This long-range interaction results in an energy shift for the excitation of two Rydberg atoms, when atoms are sufficiently close, eventually prohibiting the excitation of more than one atom - the so called Rydberg blockade [Gaë09, Wil10]. The dipolar interaction, however, is tunable by

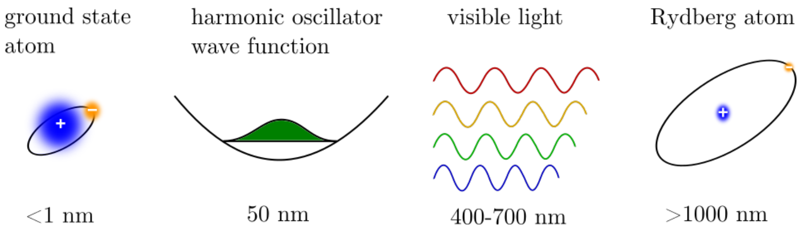

**Figure 1.1:** Length scales of the atomic wave function for a Rydberg atom and an atom in the electronic ground state compared to the wavelength of visible light and a typical harmonic oscillator used within this thesis.

the distance of two atoms and can be switched by excitation lasers, prerequisites for an application in quantum computing and simulation. Since individual trapping of neutral atoms in optical tweezers allows to create arrays of 1D- to 3D-structures of atoms at fixed interparticle distances, the application of Rydberg atoms for scalable quantum information processing is pursued [Saf10, Mal15, Lab16, Ber17, Bro20]. A comparison of length scales for atoms in the electronic ground state and Rydberg states is given in figure 1.1 and highlights the large extension of the atomic wave function, which enables strong dipole-dipole interactions.

## Trapped Ions

Positively charged ions can be spatially confined by electromagnetic fields and, similarly to trapped atoms, their internal and external dynamics, that is electronic and motional states, can be manipulated by lasers. Multiple ions trapped within the same potential interact due to the mutual Coulomb force and sufficiently cooled ions organize in crystals with fixed interparticle distance. All ions are coupled via common oscillations, which can be used for entanglement generation [Møl99, Cir00]. In a trapped ion quantum bit (qubit) the state is encoded in the electronic structure with an energy splitting, which can be either addressed optically or by radio-frequency. For $^{40}\mathrm{Ca}^+$ ions, the *optical qubit* is defined as the states of the $4\mathrm{S}_{1/2} \rightarrow 3\mathrm{D}_{5/2}$ transition, while the Zeeman substructure of the $4\mathrm{S}_{1/2}$ state in a magnetic field is called the *spin qubit*. independent of the choice of the qubit, single and two-qubit operations with high fidelity $F > 99.7\%$ are reproducibly achieved [Gae16, Pog21, Pij21]. Although technical improvements might even enhance the gate fidelity, especially for multi-qubit operations, the scalability of trapped ion quantum computers is challenging due to the number of vibrational modes and required individual addressing of each qubit. A possible pathway to scalability is a shuttling based architecture, where large qubit registers are realized by transport, split, merge and rotations on small ion crystals, while laser operations only address ions at dedicated interaction sites [Kie02, Wal12, Rus14, Kau17b]. The reconfiguration of the qubit register, however, consumes time not available to laser interaction and leads to long experimental sequences of a few ten ms, even for small number of ions [Hil21]. Consequently, the reduction of sequence time is desired and might be achieved by using advanced laser operation schemes for entangling gates, much faster than typical gate times in the order of 100 µs [WC17, Sch18]. Still, gates between trapped ions utilize the Coulomb interaction and the coupled motion, where individual addressing of oscillations becomes more difficult with increasing number of ions as more vibrational modes are present. Introducing Rydberg-specific features might extend the toolbox for gate operations in trapped ion systems. As a promising candidate, the dipole-dipole interaction between two Rydberg excitations is studied and first results show entangling between two ions by Rydberg blockade [Mü08, Zha20]. In this context, the high control of trapped ions with well established experimental techniques for state manipulation is combined with Rydberg states for the long-range interaction as well as their sensitivity to external fields.

## Trapped Rydberg Ions

Early successful Rydberg excitations of trapped ions show the effects of polarizability and residual electric fields by displacing the ion within the trap potential [Fel15, Hig17, Mok19]. In general, the prospect of realizable trapped Rydberg ions generated much interest in theory, to use the induced dipole moments and long-range interactions for quantum computing [Li13a, Li13b]. Recently, this led to the demonstration of a two-qubit gate with $^{88}\mathrm{Sr}^{+}$ ions using the Rydberg blockade [Zha20]. Since the dipole-dipole interaction between two Rydberg ions is not dependent on the motion, but rather the interparticle distance, gate operation shorter than one µs was achieved and confirms that the Rydberg blockade is applicable for scalable quantum computing. Moreover, the large polarizability of Rydberg states in combination with the trap fields (especially in a shuttling based architecture) allows to observe energy shifts, to propose new entanglement methods or to study the long-range interactions between multiple Rydberg excitations in ion crystals. To excite Rydberg states of trapped ions, the ion needs to be precisely positioned in the electric field minimum of the trap, since any residual field leads to significant quadratic Stark shifts. The Paul trap creates spatial confinement with the ion trapped in a field free position, where gradients define the confinement. These gradients, however, are probed by the highly excited ion and lead to state-dependent trap frequencies as a direct consequence of the huge polarizability of Rydberg states [Mü08, Li12].

This thesis describes reliable Rydberg excitation of trapped $^{40}$Ca$^{+}$ ions via a resonant two-photon process. The properties of high-lying electronic states in combination with finite ion temperatures and the coupling to the trap field are studied. Focus lies on the state-dependent confinement, which arises from the huge polarizability of Rydberg states as a measure of wave function extension and energy level spacing. The harmonic motion of single ions and crystals with up to four ions is investigated with respect to its influence on Rydberg excitation, especially for ions with either a thermal or a coherent phonon distributions. The latter allows to experimentally extract polarizabilities in an easy to implement sequence and prepares measurements on two-ion entanglement using ultra-fast electric pulses with durations in the order of µs and below. Moreover, the interaction of Rydberg ions in a linear string can be studied in terms of interparticle distance and coupled motion.

In section 2 the properties of trapped Rydberg ions are theoretically investigated and their possible applications are briefly discussed. Section 3 and 4 introduce the experimental setup and show initial measurements on Rydberg excitation, respectively, with main emphasis on external and internal field control. After introducing a model for the transition lineshape, the coherent motional excitation of a single ion is used to extract the Rydberg state polarizability in section 5. The state-dependent trap frequencies are used in section 6 to propose a laser-less entanglement scheme utilizing two Rydberg ions shuttled within electric fields. The distance-dependent Van-der-Waals force is studied in section 7 with linear crystals, before section 8 summarizes the results and gives an outlook onto planned experimental improvements and proposals to investigate with trapped Rydberg ions.

# 2

# Far Away from Home: Highly Polarizable Ions in Electric Fields

Rydberg states of atoms and ions are highly excited electronic states, that come with a large extension of their electronic wave function and are extremely sensitive to surrounding electric fields. Hence, a trapped ion excited to Rydberg states experiences additional forces due to its huge polarizability, but remains trapped in suitable electric potentials. There are many books and articles about trapping of charged particles in Penning traps or Paul traps [Pen36, Pau90, Met99, Nä00, Lei03], such that low-lying electronic states are only briefly discussed here. However, the field of trapped Rydberg ions is still young with contributions of a few groups from theory and even less from the experimental side, quite in contrast to the rich physics that might be explored [Mü08, SK11, Li12]. The excitation of Rydberg states within the electric trapping field modifies the ion dynamics, an effect already observable by a single ion. Additionally, Coulomb crystals of more than one ion experience switchable forces by excitation to Rydberg states, which are dependent on the interparticle distance.

This section is structured as follows: First, the trapping potential for a single ion is examined and the influence of the oscillating trap potential onto the ion is discussed. For more than one ion, the Coulomb repulsion leads to common oscillations and creates a fully connected ion crystal with fixed interparticle distance. Then, general properties and scaling laws of Rydberg states are introduced, before the case of a trapped ion excited to Rydberg states is studied. Here, the huge polarizability couples internal and external dynamics of the ion, or the ion crystal, such that state-dependent forces can be implemented. Finally, the Rydberg blockade between two ions in highly excited states with rotating dipole moments is presented. Rydberg ions utilizing a combination of the discussed ideas are suitable as a novel platform for fast quantum computing and simulation [Mü08, Li13b, Vog19] and have already been demonstrated in various ways [Fel15, Hig17, Zha20].

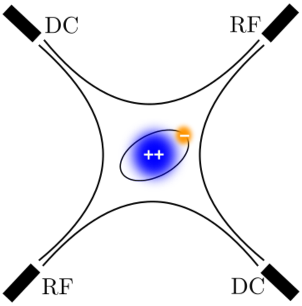

**Figure 2.1:** Scheme of the radial trap field confining a positively charged ion.

## 2.1 Rydberg Ions Confined in a Harmonic Paul Trap

Positively charged ions are accelerated by electric fields in the direction of field lines and, thereby, repelled by positively charged surfaces. However, it is impossible to trap a charged particle just with static electric fields in three directions, as the trap volume either becomes field free or the ion position is unstable for small perturbations. Two prominent trap designs overcome this obstacle by using a combination of static electric field with either a static magnetic field in Penning traps [Pen36] or an oscillating electric field in Paul traps [Pau90]. Here, an idealized linear Paul trap is discussed, which provides a radio-frequency (RF) field perfectly aligned along the radial directions $(x, y)$ and axial $(z)$ confinement by a static field. In real linear Paul traps, the RF field also has components along the $z$ axis, which lead to micromotion (c.f. section 4.1). In the idealized picture, the corresponding electric potential $\Phi(\mathbf{r}, t)$ with $\mathbf{r} = (x, y, z)$ at time $t$ can be written by

$$\Phi(\mathbf{r}, t) = \gamma_{\mathrm{RF}} \cos(\Omega_{\mathrm{RF}} t)[x^2 - y^2] - \gamma_{\mathrm{DC}} \left[(1+\epsilon)x^2 + (1-\epsilon)y^2 - 2z^2\right] \quad . \tag{2.1}$$

Here, $\gamma_{\mathrm{DC}}$ is the static field gradient and $\gamma_{\mathrm{RF}}$ the field gradient of the RF field with drive frequency $\Omega_{\mathrm{RF}}$. The electric potential is restricted to the harmonic confinement, which is a good approximation for hyperbolic shaped electrodes or if the ion's motion is restricted to a very small region of space, much smaller as compared to the dimension of the electrodes. The dimensionless parameter $\epsilon$ describes a radial asymmetry, which can be controlled by the trap geometry or the voltages on individual radial electrodes. A trapped ion in the radial field of a Paul trap is schematically shown in figure 2.1. For typical experiments the static field gradient is up to three orders of magnitude smaller compared to the RF field gradient and consequently, an ion is confined much stronger along radial directions.

Since the internal structure of the trapped ion is effectively described by a two-body system consisting of ionic core and valence electron, it is helpful to describe the external trapping field from equation 2.1 also in terms of ionic core $\mathbf{r}_\mathrm{c}$ and electron coordinates $\mathbf{r}_\mathrm{e}$. As the ionic core with mass $M$ is four orders of magnitude heavier than the electron with mass $m$, the coordinates are conveniently transformed into a center-of-mass system, where the ionic core is almost at rest with position $\mathbf{r}_\mathrm{c} \approx \mathbf{R} = (X, Y, Z)$ and the electron at position $\mathbf{r}_\mathrm{e} \approx \mathbf{R} + \mathbf{r}$. Combining internal energy of the ion with the quadrupole trapping field, evaluated at the respective electron and core position, results in the Hamiltonian for a single ion:

$$H(\mathbf{R}, \mathbf{r}, t) = \frac{\mathbf{P}^2}{2M} + \frac{\mathbf{p}^2}{2m} + 2e\Phi(\mathbf{R}, t) - e\Phi(\mathbf{R} + \mathbf{r}, t) + V(|\mathbf{r}|) + H_\mathrm{FS} \quad . \tag{2.2}$$

The first two terms are the kinetic energies of the ionic core and electron, respectively, while $V(|\mathbf{r}|)$ is the Coulomb interaction, and $H_\mathrm{FS}$ accounts for the spin-orbit coupling. Assuming a small distance between electron and ion ($\mathbf{r} \ll \mathbf{R}$), the potential contribution $\Phi(\mathbf{R} + \mathbf{r}, t)$ can be expanded around the position of the ionic core and simplifies to

$$\Phi(\mathbf{R} + \mathbf{r}, t) \approx \Phi(\mathbf{R}, t) + \frac{\partial \Phi(\mathbf{R}, t)}{\partial \mathbf{R}} \cdot \mathbf{r} + \frac{1}{2} \sum_{kl} \frac{\partial^2 \Phi(\mathbf{R}, t)}{\partial R_k \partial R_l} \cdot r_k r_l \tag{2.3}$$

$$= \Phi(\mathbf{R}, t) + \frac{\partial \Phi(\mathbf{R}, t)}{\partial \mathbf{R}} \cdot \mathbf{r} + \Phi(\mathbf{r}, t) \quad . \tag{2.4}$$

In total, the interaction of ion and oscillating trap potential can be separated into parts that are dependent on the center-of-mass position $\mathbf{R}$, the position of the valence electron $\mathbf{r}$ with respect to the center of mass, and a coupling term, which relates the change in center-of-mass coordinate to the moving electron. For stable ion trapping, the center of mass needs to be confined in all three directions. Due to the static field gradient, there is always a confining force along the axial direction, but oscillating field creates time-dependent confining and anti-confining forces along the two radial directions. Consequently, it is helpful to transform the Hamiltonian into a frame co-rotating with the quadrupole field using the unitary [Mü08]:

$$U(\mathbf{R}, t) = \exp\left(\mathrm{i} \frac{e\gamma_\mathrm{RF}}{\hbar \Omega_\mathrm{RF}} \left[X^2 - Y^2\right] \sin(\Omega_\mathrm{RF} t)\right) \quad , \tag{2.5}$$

such that the transformed Hamiltonian follows as

$$H'(\mathbf{R},\mathbf{r},t) = U(\mathbf{R},t)H(\mathbf{R},\mathbf{r},t)U^\dagger(\mathbf{R},t) + \mathrm{i}\hbar\frac{\partial U(\mathbf{R},t)}{\partial t}U^\dagger(\mathbf{R},t) \tag{2.6}$$

$$= H_{\mathrm{CM}}(\mathbf{R}) + H_{\mathrm{el}}(\mathbf{r}) + H_{\mathrm{CM\text{-}el}}(\mathbf{R},\mathbf{r},t) + H_{\mathrm{mm}}(\mathbf{R},t) \quad . \tag{2.7}$$

Note, to perform the unitary transformation one has to use the commutator algebra $[R_i, R_j] = [R_i, r_j] = [R_i, p_j] = 0$ and $[R_i, P_j] = \mathrm{i}\hbar\delta_{ij}$ with $\delta_{ij}$ the Kronecker delta. Equation 2.7 consists of time-dependent as well as time-independent parts, where individual contributions of center of mass, valence electron and coupling terms can be identified. For the center-of-mass coordinate the energy inside the quadrupole field is given by

$$H_{\mathrm{CM}}(\mathbf{R}) = \frac{\mathbf{P}^2}{2M} + \frac{1}{2}M\omega_x^2X^2 + \frac{1}{2}M\omega_y^2Y^2 + \frac{1}{2}M\omega_z^2Z^2 \quad . \tag{2.8}$$

This is the standard form of a harmonic oscillator in three dimensions with mode frequencies

$$\omega_x = \sqrt{\frac{2e^2\gamma_{\mathrm{RF}}^2}{M^2\Omega_{\mathrm{RF}}^2} - \frac{2e\gamma_{\mathrm{DC}}(1+\epsilon)}{M}} \quad , \tag{2.9}$$

$$\omega_y = \sqrt{\frac{2e^2\gamma_{\mathrm{RF}}^2}{M^2\Omega_{\mathrm{RF}}^2} - \frac{2e\gamma_{\mathrm{DC}}(1-\epsilon)}{M}} \quad , \tag{2.10}$$

$$\omega_z = \sqrt{\frac{4e\gamma_{\mathrm{DC}}}{M}} \quad . \tag{2.11}$$

The term $H_{\mathrm{CM}}$ characterizes confinement of the ion's center of mass within the oscillating and static fields, which combined generate a harmonic pseudopotential in three directions. For low temperatures, typically achieved by laser cooling, the trapped ion can be described as a quantum harmonic oscillator with its motion quantized in terms of the secular frequencies $\omega_{x,y,z}$. At the end of this section and - more detailed - in section 6.1, bosonic ladder operators are introduced to discuss the kinetic energy of an ion as quantum harmonic oscillator. Here, the motion of the ion is externally defined by the applied electric field gradients as well as the RF drive frequency. The two radial modes are non-degenerate due to $\epsilon$. Within this thesis, a finite $\epsilon$ stems from the axial confinement, as the trap electrodes are not infinitely long and more importantly, consist of several separated segments with individual control voltages. A detailed discussion of the implemented trap design, control voltages and resulting trap field gradients is given in section 3.1.

Moreover, the center-of-mass coordinate is contributing to the total energy by the time-dependent micromotion term $H_{\mathrm{mm}}$:

$$\begin{aligned} H_{\mathrm{mm}}(\mathbf{R},\mathbf{t}) = &- \frac{2e\gamma_{\mathrm{RF}}}{M\Omega_{\mathrm{RF}}} \sin\left(\Omega_{\mathrm{RF}} t\right)\left(XP_x - YP_y\right) \\ &- \frac{e^2\gamma_{\mathrm{RF}}^2}{M\Omega_{\mathrm{RF}}^2} \cos\left(2\Omega_{\mathrm{RF}} t\right)\left(X^2 + Y^2\right) \quad . \end{aligned} \tag{2.12}$$

Here, the RF field superimposes oscillations onto the harmonic motion of the ion with frequencies of $\Omega_{\mathrm{RF}}$ and $2\Omega_{\mathrm{RF}}$. Both terms describe intrinsic micromotion, which can not be reduced by any cooling method and is directly dependent on the RF amplitude and frequency. This corresponds to a driven harmonic oscillator with drive frequency far above the secular frequency, such that the motion gets modulated. Whenever the drive frequency equals multiples of the secular frequencies, additional nonlinear terms in the dynamic potential lead to high excitation and instability of the ion's motion. However, driving the Paul trap with high frequency $\Omega_{\mathrm{RF}}$, the effects of intrinsic micromotion can be neglected [Coo85]. Generally, one distinguishes between intrinsic micromotion, in which the secular motion of the ion leads to spatial crossings of the RF null, and excessive micromotion, which arise from an additional displacement off the center by static electric fields (e.g. by non-overlapping static- and RF-field nulls) [Ber98, Kel15]. A field generating excessive micromotion might be included in equation 2.12 by a term $e\mathbf{f}(t)$ that leads to a static displacement of the ion in all three trap directions. Influenced by a static field, the ion experiences first and second order Doppler shifts, which can be measured by various methods as presented in section 4.1. Experimentally, the excess micromotion can be compensated by dedicated control voltages to overlap static- and RF-field nulls.

Due to the huge ratio between core mass and electron mass $M/m$, the loosely bound valence electron does not contribute to the dynamics of the ion inside the trap. Though, the total energy of the ion is dependent on the position of the electron with respect to the center of mass given by

$$H_{\mathrm{el}}(\mathbf{r},t) = \frac{\mathbf{p}^2}{2M} + V(|\mathbf{r}|) + H_{\mathrm{FS}} - e\Phi(\mathbf{r},t) \quad . \tag{2.13}$$

The electronic part of the Hamiltonian contains the kinetic term, the Coulomb potential, the fine structure and the interaction of electron and trap field. Without the latter, these terms correspond to the energy levels of a free atom and is discussed with respect to highly excited Rydberg states. Here, the electronic states of $^{40}\mathrm{Ca}^+$ are studied, which are defined by the excitation of a single valence electron and described by the principal quantum number $n$, the orbital angular momentum quantum number $l$, the total angular momentum quantum number $j$ and the magnetic quantum number $m$. Therefore, the quantum state of the ion is given by the electronic wave function $|\Psi\rangle = |n, l, j, m\rangle$. Rydberg states are understood to be quantum states with high principal quantum number $n$, where the energy level is close to the ionization limit. For the experiments presented in this thesis principal quantum numbers between $n \in [35, 70]$ are of interest. For low angular momentum states ($l < 5$) the electron's spatial probability distribution is not well separated from the core position. The coupling of valence electron to the core dynamics as well as other electrons lowers the energy of the internal state. This concept is described by the *quantum defect* $\delta(l)$ [Gal94, Dje91], which can be numerically calculated or measured and results in an effective principal quantum number $n^* = n - \delta(l)$. Combining the Coulomb interaction between electron and ionic core $V(|\mathbf{r_e} - \mathbf{r_c}|)$ with the spin-orbit coupling for different total angular momentum states, the energy for Rydberg states is expressed by the Ritz-formula [Rit08, Mok20]:

$$E_{n,l,j} = I^{++} - \frac{R' Z^2}{(n^*)^2} + \frac{R' Z^4 \alpha_{\text{FS}}^2}{(n^*)^3} \left( \frac{3}{4n^*} - \frac{1}{j + {}^1\!/_2} \right) \quad . \tag{2.14}$$

Here, $I^{++}$ is the second ionization energy, $R'$ the reduced Rydberg constant, $Z$ the charge of the ionic core and $\alpha_{\text{FS}}$ the fine structure constant, respectively. For high $n$ the state energy approaches the second ionization energy and Rydberg states are sensitive to field ionization [Kor83]. Moreover, the electric field term $e\Phi(\mathbf{r}, t)$ in equation 2.13 evaluated at the position of the electron leads to an energy shift depending on the internal state of the ion. For low-lying electronic states the extension of the wave packet is small and the energy shifts are negligible. Rydberg states, however, experience significant coupling to static and oscillating fields. The relevant scaling laws are dependent on the overlap of atomic wave functions and will be discussed in section 2.2 in terms of principal quantum number and angular momentum states. The electronic Hamiltonian $H_{\text{el}}$ might be further extended to interactions with laser fields, such that internal state transitions (e.g. excitation to Rydberg states) can be included. The special case of a microwave driven dipole-dipole interaction between two trapped Rydberg ions is described at the end of this section.

The last contribution to the single ion Hamiltonian (equation 2.7) describes the coupling between center-of-mass motion and electronic state and is given by

$$\begin{aligned} H_{\text{CM-el}}(\mathbf{R}, \mathbf{r}, t) = &- 2e\gamma_{\text{RF}} \cos(\Omega_{\text{RF}} t)(Xx - Yy) \\ &- 2e\gamma_{\text{DC}} \left((1+\epsilon)Xx + (1-\epsilon)Yy - 2Zz\right) \quad . \end{aligned} \tag{2.15}$$

Here, the position of the valence electron relates to the center-of-mass coordinates and generate state-dependent energy shifts of the harmonic oscillator. Similar to $\Phi(\mathbf{r}, t)$, the effect of equation 2.15 is negligible for ions with low principal quantum number, but can become significant with larger extensions of the electronic wave function as shown in section 2.2. Due to the asymmetry of the trap axes, all three directions are affected by a different amount and need to be individually considered for high-lying electronic states. Specifically, manipulating the oscillator states can have a substantial effect on the excitation of high-lying electronic states as presented in section 5.1.

## Coulomb Crystals of More Than One Ion

So far, the Hamiltonian of a single trapped ion was discussed without quantifying the influence of Rydberg states. However, one fundamental concept and driving force for many theoretical studies of Rydberg states is the dipole-dipole interaction, which is utilized in systems of neutral atoms to achieve quantum gates and entanglement between several atoms [Wil10, Ber17]. For multiple ions confined in a Paul trap the Coulomb interaction between the ions intrinsically enables common vibrational modes, which can be used for the same purposes. The interplay of Coulomb interaction and trap fields generates stable configurations of ion crystals with fixed interparticle distances dependent on the trap fields and the number of charges. Here, the Hamiltonian for an ion exposed to an electric quadrupole field is extended to multiple ions with positions given by $(\mathbf{R}_i, \mathbf{r}_i)$. For each ion, the individual contributions to the Hamiltonian in equation 2.7 are evaluated at the corresponding ion positions. Additionally, the Coulomb interaction between all ionic cores and electrons is included. For typical ion trap experiments the distance between two ionic cores $|\mathbf{R}_i - \mathbf{R}_j| = R_{ij}$ is much larger than the core-electron distance $\mathbf{r}_i$. Hence, the Coulomb interaction can be treated by a multipole expansion to account for electronic excitation, yielding for two ions:

$$\begin{aligned} V(\mathbf{R}_i, \mathbf{R}_j, \mathbf{r}_i, \mathbf{r}_j) = \frac{e^2}{4\pi\epsilon_0} \Bigg[ \frac{1}{R_{ij}} &+ \frac{(\mathbf{R}_i - \mathbf{R}_j)(\mathbf{r}_i - \mathbf{r}_j)}{R_{ij}^3} \\ &+ \frac{r_i^2 + r_j^2 - 3(\mathbf{n}_{ij} \cdot \mathbf{r}_i)^2 - 3(\mathbf{n}_{ij} \cdot \mathbf{r}_j)^2}{2R_{ij}^3} \\ &+ \frac{\mathbf{r}_i \cdot \mathbf{r}_j - 3(\mathbf{n}_{ij} \cdot \mathbf{r}_i)(\mathbf{n}_{ij} \cdot \mathbf{r}_j)^2}{2R_{ij}^3} \Bigg] \quad , \end{aligned} \tag{2.16}$$

with $\mathbf{n}_{ij} = {}^{\mathbf{R}_i - \mathbf{R}_j}/_{R_{ij}}$. The first term, scaling with ${}^1/_{R_{ij}}$ is the Coulomb repulsion between the two ionic cores, which leads to the large interparticle distances in the Paul trap and allows for the creation of ion crystals with defined ion equilibrium positions. The second and third term correspond to a charge-dipole and charge-quadrupole interaction, respectively. Note, that the interactions involving dipole and quadrupole terms are dependent on the electronic excitation and thereby create state-dependent energy shifts. Combining the charge-dipole term with the core-electron interaction from equation 2.15 accounts for all couplings between internal and external dynamics. The charge-quadrupole term can be evaluated for each ion individually and creates a position-dependent variation of the static trap field gradient. Thereby, the energy levels of highly excited states with $l > 0$ become sensitive to the position of the ion within the crystal, but corresponding energy shifts are not relevant for this thesis. The last term of equation 2.16 accounts for the dipole-dipole interaction. As the configuration of an ion crystal is governed by the Coulomb interaction, the effective electric field for the individual ions is the same and the ions do not exhibit a permanent dipole moment, because every ion is at the center of a local electric quadrupole field [Mü08]. Thereby, the dipole-dipole term is typically negligible for trapped ions and the related energy shift can be approximated by a Van-der-Waals force scaling with the interparticle distance $\propto {}^{1}/_{R_{ij}^{6}}$. Even though the atomic wave function of Rydberg ions is substantially larger compared to ions in low-lying electronic states, the Van-der-Waals force between Rydberg ions remains small and highly sensitive experiments are necessary to resolve energy shifts of this distance-dependent interaction, as shown in section 7.1. However, inducing a rotating dipole moment to Rydberg ions by microwave dressing, strongly enhances the dipole-dipole terms and can lead to entanglement between several ions as discussed at the end of this section.

The multipole expansion of equation 2.16 is presented for two ions, but more ions can be included analogously by summation over the respective ion positions. Within a linear Paul trap the axial and radial trap frequencies are typically chosen to be non-degenerate and the axial confinement is much weaker compared to the radial confinement. Therefore, a crystal consisting of only a few ions orients itself in a linear configuration along the RF null and the interparticle distance is given by the force equilibrium between harmonic confinement and Coulomb repulsion. For identical ions the crystal is symmetric to the crystal center with interparticle distances, which are increasing from the inner to the outermost ions [Jam98]. With larger ion numbers (or ratio of axial to radial trap frequencies), the ions form a 2D or 3D crystal, where motion is no longer separable into the three directions of the trap axes. Generally, a crystal of $N$ ions is vibrating along $3N$ harmonic oscillator modes, which split into $N$ modes along each trap direction for a linear ion string. As the mode frequencies are given by the trap field gradient in combination with the Coulomb repulsion between the ions, for radial modes the common trap frequencies are typically lower compared to the ones of a single ion, while the common axial modes are higher in frequency. The center-of-mass motions, where all ions oscillate in phase are found along each trap direction and their frequencies coincide with the trap frequencies of a single ion.

The transition between linear and 2D/3D crystal configuration is determined by the anisotropy parameter $\mathcal{A} = ({}^{\omega_z}/{\omega_r})^2 \approx 2.53N^{-1.73}$ [Sch93, Fis08], where $\omega_r$ is the lower frequency mode of both radial center-of-mass motions. For degenerate trap frequencies along the radial directions a 3D crystal rotates around the RF null, while for unequal radial trap frequencies the ions form a 2D or 3D crystal, which is compressed along the direction of the higher field gradient [Rei02]. A stable 2D crystal can be oriented in a *zigzag* configuration, where ions are alternately positioned on either side of the RF null and the extension into the radial direction is given by the compression of the Coulomb crystal due to the axial confinement. Dynamically changing the anisotropy parameter for a string of ions towards formation of a zigzag crystal can help to study phase transitions and defect formation in crystals [Ulm13]. Moreover, state-dependent anisotropy parameters and, thereby, state-dependent crystal configurations might be explored by implementing Rydberg ions [Li12].

## 2.2 Strong Interactions and Relevant Properties of Rydberg States

The electronic state of an atom or ion is described by the set of quantum numbers $|\Psi_{n,l,j,m}\rangle = |n,l,j,m\rangle$. The Rydberg states within this thesis are described by principal quantum numbers $n > 35$, such that the electronic state is well separated from energy levels $n \in \{3,4,5\}$ close to the ground state of typical trapped ion experiments (e.g. for ${}^{40}\mathrm{Ca}^+$: $|4,\mathrm{S},{}^1/{}_2,m\rangle$). As Rydberg states vary over a large range of principal quantum numbers it is helpful to discuss properties of Rydberg atoms and ions in terms of scaling laws as a function of $n$. Equation 2.14 discusses the energy of Rydberg states, which approach the second ionization energy for large values of $n$. Also the reduction of the energy level by the quantum defect is introduced, as the bound electron has partial overlap with the ionic core potential for low angular momentum states $l < 5$. Additionally, ions in a magnetic field experience an energy shift for different magnetic quantum numbers $m$ due to the Zeeman shift. From equation 2.14 follows a scaling of energy levels with the principal quantum number by $n^{-2}$ and the energy difference between Rydberg levels of adjacent principal quantum number decrease with $\Delta E_{n,n+1} \propto n^{-3}$. States with different angular momentum might be even closer to each other, such that coupling of energy levels need to be considered and result in large susceptibility to external fields.

Another property of highly excited states and driving force of most of the interactions between multiple Rydberg ions, or a Rydberg ion and an electric field, is the large extension of the electronic wave function. Generally, the wave function is described by a radial part depending on $n, l$ and an azimuthal part depending on $l, j, m$, which can be separated to simplify calculation of overlap integrals. The latter requires numerical tools and is not relevant for the results of this thesis, thus the overlap integrals are not evaluated in detail. Nevertheless, certain scaling laws according to [Mü08] are given. For high-lying Rydberg states the extension of the radial wave packet $\langle r \rangle \propto n^2$ can be orders of magnitude larger compared to electronically low-lying states. Intuitively, the interaction between two *huge* ions or the sensitivity of one of these to external fields has to be large. Rydberg ions trapped in the harmonic potential of a Paul trap are affected by the oscillating and static fields (c.f. equation 2.13), both causing quadrupole shifts depending on the principal quantum number. For high-lying states with $l = 0$, that is $n$S-Rydberg states, the wave function is isotropic and no quadrupole shifts are present. Contrary, for angular momentum states with $l > 0$, both static and oscillating part of the trap field give rise to shifts proportional to the radial matrix elements estimated by $\left|\langle n, l|r^2|n, l\rangle\right| \approx a_0 n^4$, where $a_0$ is the Bohr radius. The static quadrupole shift for $n$P-Rydberg states can be summarized by:

$$\Delta E_{\mathrm{P},j,m} = \frac{2}{15} e\gamma_{\mathrm{DC}} \left|\langle n, 1|r^2|n, 1\rangle\right| \left[2|m| - j - \frac{9}{2}\right] \quad . \tag{2.17}$$

Here, one assumes that the energy splitting to neighboring levels as well as the fine structure splittings are large enough and the static field of the Paul trap does not couple different electronic states. Contrary, the oscillating field with drive frequency $\Omega_{\mathrm{RF}}$ is in the order of the Zeeman splitting for different $m$ states ($\approx$ 10 MHz), such that quadrupole transitions with $|\Delta m| = 2$ are strongly coupled for states with equal total angular momentum, giving rise to energy shifts of

$$\Delta E_{\mathrm{osc}} \approx e\gamma_{\mathrm{RF}} a_0^2 n^4 \cos(\Omega_{\mathrm{RF}} t) \quad . \tag{2.18}$$

For states with $j < 3/2$ this effect can be neglected, as the energy difference to the next Rydberg states is much larger than the drive frequency $\Omega_{\mathrm{RF}}$. To reduce the complexity of calculating level shifts for the excitation of Rydberg states in trapped ions, the high electronic excitations discussed within this thesis are limited to $j = 1/2$.

For Rydberg $n\mathrm{S}_{1/2}$- or $n\mathrm{P}_{1/2}$-states of single ions the energy is largely unaffected by the electric field of the trap and the transition frequency for laser excitation can be calculated by the energy difference between the desired Rydberg state and the initially prepared electronically low-lying state $|g\rangle$. Estimating the squared transition matrix element $|\langle g|r|n,l,j,m\rangle|^2 \propto n^{-3}$ implies, that higher Rydberg states are more difficult to excite, as more laser power is required and the transition wavelength decreases. The excitation of a trapped ion into Rydberg states by a single photon demands energies of $\approx 10\,\mathrm{eV}$ and highly sophisticated laser systems [Wal01, SK11]. Following the selection rules for electric dipole transitions, a $^{40}\mathrm{Ca}^{+}$ ion, initialized in the metastable state $|g\rangle = 3\mathrm{D}_{5/2}$, can be excited by a single photon to $n$P- or $n$F-Rydberg states with $j \geq 3/2$, where large quadrupole shifts arise as discussed in equations 2.17 and 2.18. Instead, addressing $|g\rangle$ by two photons allows for excitation of $j = 1/2$ states, while requiring less demanding and commercially available laser sources. Using laser frequencies close to an atomic resonance enhances the coupling between electronically low- and high-lying states, such that resonant two-photon excitation is the *state-of-the-art* excitation method in trapped Rydberg ion experiments [Hig17, And21].

Once a trapped ion is in a Rydberg state its interaction with the environment, given by other ions and electric fields, is strongly enhanced until it is either deexcited by another laser pulse or spontaneously decays into a low-lying electronic state. This state decay follows a lifetime scaling $\tau \propto n^3$ and is in the order of 1 to 100 µs [Glu13]. The scaling can be easily derived by expressing the decay as a summation over Einstein coefficients $\mathcal{A}_{n,n'}$ for spontaneous decay from level $n$ to $n'$ for all final states $n'$ [Gal88].

$$\frac{1}{\tau_n} = \sum_{n'} \mathcal{A}_{n,n'} \propto \sum_{n'} \nu^3_{n,n'} \left|\langle n'|r|n\rangle\right|^2 \tag{2.19}$$

As the Einstein coefficient is proportional to the cube of the transition frequency $\nu_{n,n'}$, the decay to the lowest level - and consequently largest frequency difference - is dominating. However, the transition matrix element to the lowest energy level scales with $\propto n^{-3/2}$ (contrary to $\propto n^2$ for transitions between Rydberg states) and results in a lifetime scaling $\tau_n \propto n^3$. Using circular states, namely states with maximal angular momentum, the lifetime of highly excited states can be further prolonged [Sig17]. Since the orbital angular momentum can only change by one for dipole allowed transitions, a maximum angular momentum state effectively prohibits channels for spontaneous emission except the one to the next lower Rydberg state and leads to a lifetime scaling $\propto n^5$. For ions in a Paul trap the excitation of high angular momentum states is challenging by the large quadrupole shifts and couplings between electronic levels.

Even if the probability to find the electron close to the ionic core is large, that is for low angular momentum, the wave packet of a Rydberg state is extended much further compared to electronically low-lying states and the ion experiences significant energy shifts by electric fields. In a Paul trap the electric field results in a charge separation between the electron and the ionic core for large extensions of Rydberg states and it is challenging to engineer the electric fields in such a way, that no stray fields shift the ion out of its equilibrium position. The coupling strength of the ion interacting with a (time averaged) electric field $E_{\text{RMS}}$ is given by the polarizability $\mathcal{P} \propto n^7$ [Ovs11, Kam14] and can become sizable even for Rydberg states with moderate $n$. The energy shift for a highly polarizable ion within electric fields is given by the Stark effect [Sta14] with

$$\Delta E_{\text{Stark}} = -\frac{1}{2}\mathcal{P}E_{\text{RMS}}^2 \quad . \tag{2.20}$$

Note, only the second order Stark effect contributes to the energy shift of Rydberg states since ions confined in a Paul trap do not show a permanent dipole moment. The Stark effect may arise from residual electric fields within the Paul trap but also electric fields originating from lasers. Especially, transitions into Rydberg states need high intensity light fields to counter the $n^{-3/2}$ scaling of the transition matrix element and, thereby, shift the energy levels of the trapped ion depending on the state's polarizability.

## State-Dependent Trap Frequencies

Considering the principal quantum number scaling of the polarizability, it is important to investigate the confinement of highly excited ions within the Paul trap. Here, two complementary approaches to study the coupling of Rydberg states to the trap field are discussed. On the one hand, the approach follows a quadratic Stark effect due to a time averaged oscillating field, while on the other hand the coupling of internal and external states of the trapped ion in the presence of near electronic levels is shown.

Firstly, the ion is affected by the trap potential $\Phi(\mathbf{R}, t)$ given in equation 2.1 with an electric field $E_\Phi = -\nabla\Phi$ yielding a time-dependent Stark shift of

$$\begin{aligned}\Delta E_{\text{Stark}} &= -\frac{1}{2}\mathcal{P}\left[-\nabla\Phi(\mathbf{R}, t)\right]^2 \\ &= -2\mathcal{P}\Big[\left(\gamma_{\text{RF}}\cos(\Omega_{\text{RF}}t) - \gamma_{\text{DC}}(1+\epsilon)\right)^2 X^2 \\ &+ \left(\gamma_{\text{RF}}\cos(\Omega_{\text{RF}}t) + \gamma_{\text{DC}}(1-\epsilon)\right)^2 Y^2 + (2\gamma_{\text{DC}})^2 Z^2\Big] \quad .\end{aligned} \tag{2.21}$$

The quadratic Stark shift itself takes the form of a three dimensional harmonic oscillator. Obviously, the ion acquires an energy shift scaling with the polarizability and the square of the trap field gradient along each trap direction, which modifies the center-of-mass motion of the ion and leads to state-dependent trap frequencies. Typically, the differences in confinement and trap field gradients within the Paul trap is reflected by much larger variations in radial trap frequencies. As the RF field is fast compared to the vibration of the ion, one can time average the Stark effect obtaining

$$\begin{aligned}\langle \Delta E_{\text{Stark}} \rangle_T = -\mathcal{P}\Big[ &\left(\gamma_{\text{RF}}^2 + 2\gamma_{\text{DC}}^2 (1+\epsilon)^2\right) X^2 \\ &+ \left(\gamma_{\text{RF}}^2 + 2\gamma_{\text{DC}}^2 (1-\epsilon)^2\right) Y^2 + 8\gamma_{\text{DC}}^2 Z^2 \Big] \quad . \end{aligned} \tag{2.22}$$

Secondly, the interaction between Rydberg ion and oscillating trap field is studied by treating the coupling Hamiltonian $H_{\text{CM-el}}$ from equation 2.15 by second order perturbation theory. As the dynamics on the electronic levels are much faster compared to the center-of-mass motion, a Born-Oppenheimer approximation is valid, where the ionic core is fixed in space and the overlap integrals between electronic states are independent of the core's position. As the splitting between different energy levels with $j = {}^{1}\!/_{2}$ is large and dominant effects may only arise from the coupling of one Rydberg state to the nearest other Rydberg state, the overlap of a $n\text{S}_{1/2}$-state and the corresponding $n\text{P}_{1/2}$-state is discussed. The second order energy shift is given by:

$$E_n^{(2)} = \sum_{n'} \frac{\left|\langle \Psi_n | H_{\text{CM-el}} | \Psi_{n'} \rangle\right|^2}{E_n^{(0)} - E_{n'}^{(0)}} \approx \sum_{m} \frac{\left|\langle \Psi_{n,\text{S},0} | H_{\text{CM-el}} | \Psi_{n,\text{P},m} \rangle\right|^2}{E_{n,\text{S}}^{(0)} - E_{n,\text{P}}^{(0)}} \tag{2.23}$$

The summation over all final Rydberg states $n'$ is reduced to only the nearest adjacent state and the remaining sum accounts for different orientations of the $\text{P}_{1/2}$-state, while the energy difference in the denominator is given by the unperturbed energies of the electronic states. Since also $H_{\text{CM-el}}$ is separable in $X, Y, Z$, equation 2.23 can be individually evaluated, such that the second order energy shift for $X$ yields:

$$E_n^{(2,X)} = \frac{4e^2}{3} \left(\gamma_{\text{RF}} \cos(\Omega_{\text{RF}} t) - \gamma_{\text{DC}} (1+\epsilon)\right)^2 X^2 \frac{\left|\langle n, \text{S} | r | n, \text{P} \rangle\right|^2}{\Delta E_{n\text{S},n\text{P}}} \tag{2.24}$$

Analogous results are obtained along the directions $Y$ and $Z$. Following the time averaging in equation 2.22, the second order energy shift is given as a function of overlap between neighboring energy levels, which are approaching each other for high-lying Rydberg states. Successively comparing the energy shifts for the Stark effect with the level couplings due to the interaction Hamiltonian, the polarizability for Rydberg $S_{1/2}$-states is approximated by:

$$\mathcal{P} \approx -\frac{2e^2}{3}\frac{|\langle n,\mathrm{S}|r|n,\mathrm{P}\rangle|^2}{\Delta E_{n\mathrm{S},n\mathrm{P}}} \propto \frac{\left(n^2\right)^2}{n^{-3}} = n^7 \quad . \tag{2.25}$$

Considering the scaling of the transition dipole moment and the energy splittings between Rydberg states, the corresponding principal quantum number scaling for the polarizability $\mathcal{P} \propto n^7$ intuitively follows from the comparison of quadratic Stark effect and second order perturbation theory. Finally, one can include the polarizability-related energy shifts on the trapped ion to identify state-dependent trap frequencies:

$$\omega_x = \sqrt{\frac{2e^2\gamma_{\mathrm{RF}}^2}{M^2\Omega_{\mathrm{RF}}^2} - \frac{2e\gamma_{\mathrm{DC}}(1+\epsilon)}{M} - \frac{2\mathcal{P}\left(\gamma_{\mathrm{RF}}^2+\gamma_{\mathrm{DC}}^2(1+\epsilon)^2\right)}{M}} \quad , \tag{2.26}$$

$$\omega_y = \sqrt{\frac{2e^2\gamma_{\mathrm{RF}}^2}{M^2\Omega_{\mathrm{RF}}^2} - \frac{2e\gamma_{\mathrm{DC}}(1-\epsilon)}{M} - \frac{2\mathcal{P}\left(\gamma_{\mathrm{RF}}^2+\gamma_{\mathrm{DC}}^2(1-\epsilon)^2\right)}{M}} \quad , \tag{2.27}$$

$$\omega_z = \sqrt{\frac{4e\gamma_{\mathrm{DC}}}{M} - \frac{16\mathcal{P}\gamma_{\mathrm{DC}}^2}{M}} \quad . \tag{2.28}$$

For low-lying electronic states the polarizability is negligible and the secular frequencies of equations 2.9-2.11 are recovered. However, if the ion is excited to Rydberg states, the confinement along all trap directions changes depending on the principal quantum number. Analogous to the picture of a large ion interacting with electric fields one could rephrase the state-dependent secular frequencies as an effective mass change of the trapped ion by excitation into Rydberg states. For experiments in linear Paul traps, the Rydberg states predominantly alter the radial trap frequencies, although the $n^7$ scaling affects the axial mode for highly excited motional states as well. Within the range of experimental parameters used throughout this thesis, frequency differences of ${}^{\delta\omega}/_{\omega} = 10^{-4}\cdots 10^{-1}$ are possible and can be explored via various concepts.

Theoretically, state-dependent trap frequencies allow for the direct study of structural phase transitions, where a Coulomb crystal trapped in a linear Paul trap is changing its geometric shape. By exciting a designated ion out of a zigzag crystal to the Rydberg state, the ions will transition into a linear string [Li12]. As the configuration of the ion crystal is dependent on the anisotropy parameter $\mathcal{A}$ given by the ratio of secular frequencies, a sudden change in the effective mass of the central ion can change the shape of the ion crystal as presented in figure 2.2. Depending on the principal quantum number and the magnitude of the polarizability, the structural phase

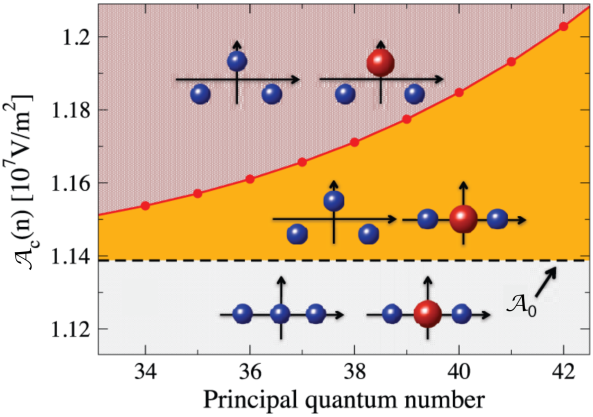

**Figure 2.2:** Proposal for observation of a structural phase transition via state-dependent trap frequencies in a linear ion string mediated by Rydberg excitation (red). For a given anisotropy parameter and principal quantum number, the Rydberg excitation of the central ion leads to a change in crystal shape, where for each shaded region the initial shape is always shown on the left hand side and the final shape on the right hand side. Image taken from [Li12].

transition within the ion trap can be explored. Already moderate principal quantum numbers allow for a large range of anisotropy parameter, where the ion crystal changes shape upon excitation of the Rydberg state. Another proposal uses a long linear ion crystal and position-dependent Rydberg excitation to create smaller sub-crystals with decoupled motion as shown in figure 2.3 [Li13a]. The normal mode spectrum of all trapped ions is divided into smaller sections at the positions of Rydberg excitations, such that individual laser operations may be performed on the decoupled sub-systems with well localized motional modes. Typically, the individual addressing of ion motion is not possible, as all ions are coupled by the Coulomb forces and for an ion crystal consisting of several tens of ions, the mode spectrum becomes very dense. Decoupling the vibrational modes by Rydberg excitation may lead to a scalable trapped ion processor for quantum simulation and computing, where entangling gates might be performed on sub-crystals of two ions. A reconfiguration of the ion processor is possible by time-dependent Rydberg excitation at different positions within the ion string. Further ideas to use the state-dependent trap frequencies involve engineering motional modes in hexagonal plaquettes for spin-spin interactions [Nat15] or exploration of non equilibrium dynamics [Gam20]. Within this thesis, the state-dependent trap frequencies are utilized for measuring polarizabilities by coherent motional excitation in section 5.1 and proposing a new scheme for an ultra-fast entangling gate by

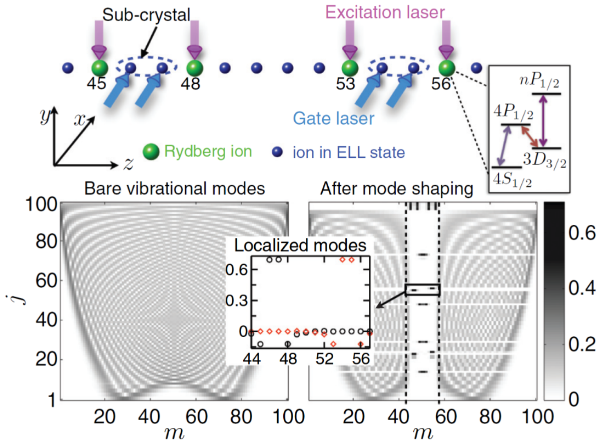
Sub-crystal
Excitation laser
45
48
53
56
Gate laser
y
x
z
Rydberg ion
ion in ELL state
nP1/2
4P1/2
3D3/2
4S1/2
Bare vibrational modes
After mode shaping
Localized modes
j
m
0.6
0.4
0.2
0

**Figure 2.3:** Mode shaping by Rydberg excitation (green) in a long ion string. The Rydberg excitation decouples localized sub-crystals from the motion of the surrounding ions and enables gate operation on smaller crystals compared to the initial long ion string. The lower panel shows coupling for ion number $m$ to vibrational modes $j$ before (left) and after (right) mode shaping. Image taken from [Li13a].

electric kicks in section 6.1.

## 2.3 Excitation of Internal and External Degrees of Freedom

A trapped ion inside the harmonic potential of the Paul trap can be described by an internal state, the electronic excitation, and by the occupation of vibrational energy levels called the external state. If cooled to very low temperatures below a few mK by lasers, the motion is well described by a quantized harmonic oscillator with energy spacing of $\hbar\omega_{x,y,z}$ for each of the three trap directions. Dynamics between these vibrational energy levels, corresponding to adding and removing energy quanta named phonons, can be described by creation $a$ and annihilation operators $a^\dagger$ given by:

$$a_i = \sqrt{\frac{M\omega_i}{2\hbar}}\left(R_i + \frac{\mathrm{i}}{M\omega_i}P_i\right) \quad , \tag{2.29}$$

$$a_i^\dagger = \sqrt{\frac{M\omega_i}{2\hbar}}\left(R_i - \frac{\mathrm{i}}{M\omega_i}P_i\right) \quad . \tag{2.30}$$

The index $i \in \{x, y, z\}$ denotes the direction of the ion's motion. For a one-dimensional quantized harmonic oscillator the Hamiltonian reduces to $H_{1\mathrm{D}} = \hbar\omega(a^\dagger a + {}^1\!/\!_2)$ with the occupation number of motional excitation $k = a^\dagger a$. The latter can be also represented as the state vector $|k\rangle$ with $k = 0$ being the motional ground state. The operator acting on the external state by $a\,|k\rangle = \sqrt{k}\,|k-1\rangle$ and $a^\dagger\,|k\rangle = \sqrt{k+1}\,|k+1\rangle$ lowers and raises the motional excitation by one phonon, respectively. Because of this, the operators are often called *ladder operators*, as they allow to navigate through the external energy levels. It is convenient to describe the interaction between ion and external forces, e.g. additional electrical fields, by creation and annihilation operator to directly relate the force to the ion's motional excitation. Since the total energy of a three dimensional harmonic oscillator is determined by the phonon number in each of the vibrational modes, the motional excitation provides a complete basis for characterization of the external state. One fundamental interaction of a trapped ion with external forces is a displacement of the ion by a constant electric field. The corresponding shift operator, also called displacement operator $\mathcal{D}(\alpha)$, is an important concept in quantum optics for the description of coherent states and also repeatedly used within this thesis.

$$\mathcal{D}(\alpha) = \exp\left(\alpha a^\dagger - \alpha^* a\right) \tag{2.31}$$

Here, $\alpha$ is the amount of displacement in phase space, which is the space spanned by position and momentum coordinates of the ion. Applying an external electric field effectively kicks the ion out of its equilibrium position and modifies the occupation of the vibrational energy levels. Depending on the initial phonon distribution a displacement of the ion can lead to large coherent states [Alo16] with classically evolving expectation values and will be further discussed in section 5.1.

Once the ion is trapped in the quadrupole field, the external and internal energy levels can be addressed by resonant electromagnetic radiation. For low-lying electronic states the internal energy levels are typically separated by frequencies in the optical domain and lasers can be used to excite the ion by absorption of a photon with frequency matching the atomic transition. Following the stimulated absorption process, excited states decay with a state-dependent lifetime $\tau$ and release the energy by spontaneous emission of a photon. Utilizing the Doppler effect and an atomic dipole transition with large decay rates, the ion can be cooled by repeatedly exciting the internal state with a detuned laser, where the laser frequency is lower than the resonance frequency. Depending on the ion's velocity, respective their kinetic energy and temperature, the laser frequency is Doppler shifted and eventually matches the atomic resonance and gets absorbed by the ion. A successive spontaneous decay leads to a net loss of energy of the ion, which is limited to the recoil of the ion by isotropic emission of individual photons. The optimal laser detuning $\Delta = {}^{\Gamma}\!/_{2}$ is depending on the linewidth $\Gamma = {}^{1}\!/_{\tau}$

of the excited state and leads to a minimal temperature after Doppler cooling for a two-level system:

$$T_{\mathrm{Doppler}} = \frac{\hbar\Gamma}{2k_{\mathrm{B}}} \quad , \tag{2.32}$$

where $k_{\mathrm{B}}$ is the Boltzmann constant. For $^{40}\mathrm{Ca}^{+}$ ions and cooling on the $4\mathrm{S}_{1/2} \rightarrow 4\mathrm{P}_{1/2}$ transition a minimal temperature of $T_{\mathrm{Doppler}} = 0.55\,\mathrm{mK}$ is assumed after Doppler cooling and the external state of the ion is given by a thermal phonon distribution. Note, that in reality the cooling limit is larger due to the presence of Zeeman splitting or fine structure. Also spontaneous decay into one of the metastable 3D states and finite laser linewidth of the cooling laser needs to be accounted for. To reach the motional ground state, in which no vibrational level is occupied, further cooling methods as *polarization-gradient cooling* [Dal89, Li21], *electromagnetically-induced-transparency cooling* [Mor00, SK01], or *sideband cooling* [Die89] need to be employed. The latter is used for some of the presented experiments and will be further discussed below.

Apart from stimulated absorbing and spontaneously emitting a photon, also controlled manipulation of the ion's internal states is possible by driving narrow atomic transitions with small bandwidth laser sources. The Rabi frequency $\Omega$ describes the oscillation frequency between two internal states addressed by the laser, where the state population evolves as $\propto \sin^2(\Omega t)$ with $t$ being the duration of the laser pulse. However, if the ion is trapped in a harmonic potential with vibrational frequencies $\omega$, the laser interaction gets modulated and sidebands with fixed detuning $\Delta = \pm j\omega$ to the atomic resonance are accessible ($j \in \mathbb{N}$). Driving such a sideband transition subtracts or adds $j$ vibrational quanta to the energy of the harmonic oscillator. Relating the ladder operators to phonon changing transitions imply, that the Rabi frequency for transition on the red sideband ($\Delta = -\omega$) is weaker compared to transition on the blue sideband ($\Delta = +\omega$). The red sideband is not present for ions in the motional ground state. Generally, the Rabi frequency on the carrier transition ($\Delta = 0$) is also dependent on the phonon number $k$ and reads:

$$\Omega_k = \Omega_0(1 - \eta^2 k) \quad . \tag{2.33}$$

Here, $\Omega_0$ is the Rabi frequency of the motional ground state and $\eta = {}^{2\pi}/_{\lambda}\sqrt{{}^{\hbar}/_{2M\omega}}$ is the Lamb-Dicke parameter, which relates the wavelength $\lambda$ to the spatial extension of the lowest harmonic oscillator state. Equation 2.33 holds for the so called Lamb-Dicke regime with $\eta^2(2k+1) \ll 1$, where the atomic wave packet is much smaller than the transition wavelength. Rabi oscillations for carrier transition and sidebands are illustrated in figure 2.4 for an average phonon number of $\bar{k} = 0.2$.

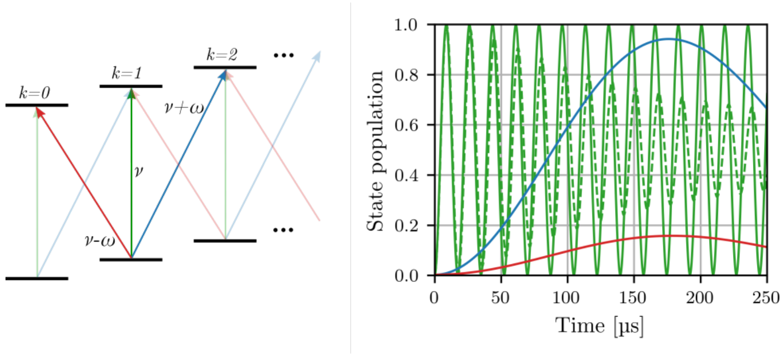

**Figure 2.4:** Excitation scheme of phonon changing transitions (left) and Rabi oscillations (right) as a function of laser illumination time. Solid lines depict the carrier, red and blue sideband transitions for an average phonon number of $\bar{k} = 0.2$ in green, red and blue, respectively. The green dashed line illustrates the carrier transition for an average phonon number $\bar{k} = 15$.

The coherent evolution of a two-level system coupled by a narrow laser source can be described by the parameters Rabi frequency $\Omega$ and detuning $\Delta$. Furthermore, one can include finite state lifetime $\tau$, laser linewidth $\Gamma_{\mathrm{Laser}}$ and other coherence limiting factors as electric and magnetic field fluctuations, but numerical methods have to be used [Mar11]. In section 4.1 multi-level Bloch equations are employed to calculate the depopulation rate of an initial state via two-photon Rydberg excitation and allow for a comparison with experimental data to extract principal quantum number scalings. In this thesis, incoherent effects as state lifetime and transition linewidth are found to be the dominant parameters next to the Rabi frequency for modeling the evolution of internal states. However, the coherent evolution between Rydberg states coupled by a microwave field is discussed in the following, which give rise to the large dipole-dipole interaction.

## Dipole-Dipole Interaction by Microwave Dressing

For neutral atoms the excitation of Rydberg states within a certain distance from each other is suppressed due to the Rydberg blockade, where the large dipole moments of two neighboring Rydberg atoms give rise to energy shifts of a few MHz [Saf10]. In systems of trapped ions, the individual ions do not exhibit permanent dipole moments and the switchable interaction by Rydberg states between two ions next to each other is much weaker compared to their neutral counterpart. However, Rydberg ions can be dressed by a microwave field to enable rotating dipole moments and generate strong dipole-dipole interactions for quantum computing and simulation [Li13b, Zha20]. A theoretical description of the dipole-dipole interaction requires two electronically high-lying levels coupled by a microwave and an initial transition into the Rydberg state. For instance, $^{40}\mathrm{Ca}^{+}$ ions are excited by a two-photon process to a $n\mathrm{S}_{1/2}$-state with a given detuning $\Delta_{\mathrm{S}}$ from two-photon resonance and immediately dressed by a microwave field to a different angular momentum state (here, a $n'\mathrm{P}_{1/2}$-state). The microwave has a Rabi frequency $\Omega_{\mathrm{MW}}$ and detuning $\Delta_{\mathrm{P}}$ to the resonance frequency. For the two coupled Rydberg states an interaction Hamiltonian for ion $j$ is obtained [Li13b]:

$$^{H_{\mathrm{MW}}(\mathbf{r}_j)}/_{\hbar} = \Delta_{\mathrm{S}} \left|\mathrm{S}\right\rangle_j \left\langle\mathrm{S}\right| + \Delta_{\mathrm{P}} \left|\mathrm{P}\right\rangle_j \left\langle\mathrm{P}\right| + \frac{\Omega_{\mathrm{MW}}}{2} \Big( \left|\mathrm{S}\right\rangle_j \left\langle\mathrm{P}\right| + \left|\mathrm{P}\right\rangle_j \left\langle\mathrm{S}\right| \Big) \quad . \tag{2.34}$$

The coupling strength of the microwave field is related to $\Omega_{\mathrm{MW}} \propto \langle \mathrm{S}|r|\mathrm{P}\rangle$ which scales with the principal quantum number $\propto n^2$. Both detunings of the laser and microwave fields can be individually adjusted. This leads to dressed states $|\pm\rangle$ for both ions:

$$\left|\pm\right\rangle_j = \frac{1}{\sqrt{1+C_{\pm}^2}} \Big( C_{\pm} \left|\mathrm{P}\right\rangle_j + \left|\mathrm{S}\right\rangle_j \Big) \quad , \tag{2.35}$$

$$C_{\pm} = \frac{\Delta_{\mathrm{P}} - \Delta_{\mathrm{S}} \pm \sqrt{\Omega_{\mathrm{MW}}^2 + \left(\Delta_{\mathrm{P}} - \Delta_{\mathrm{S}}\right)^2}}{\Omega_{\mathrm{MW}}} \quad . \tag{2.36}$$

In general, the dressed state experiences a mixture of angular momentum $l = 0$ and $l = 1$ character, as both angular momentum states are in a superposition and create a rotating dipole with Rabi frequency $\Omega_{\mathrm{MW}}$. An ion crystal of two ions in these dressed states experiences a dipole-dipole interaction (c.f. equation 2.16):

$$V_{\mathrm{dd}}(\pm) \approx \frac{e^2 \left\langle \mathrm{S}|r|\mathrm{P}\right\rangle}{4\pi\epsilon_0 R_{ij}^3} \left( \frac{C_-}{1+C_-^2} \left|--\right\rangle \left\langle--\right| + \frac{C_+}{1+C_+^2} \left|++\right\rangle \left\langle++\right| \right) \quad . \tag{2.37}$$

Intuitively, the projectors onto the dressed ion-pair states describe the Rydberg blockade. As soon as both ions are excited to Rydberg states by the same laser and microwave source, the total energy of the pair-states is shifted. If the Rabi-frequency of the Rydberg excitation laser is smaller than the dipole-dipole interaction strength, an excitation of both ions is strongly suppressed. The tunable parameter in this scenario is the interparticle distance $R_{ij}$. Ions far away from each other or single ions can still be excited to a dressed Rydberg state as distance scaling and the interaction with low-lying electronic states lead to negligible energy shifts. The projectors of the mixed states $|+-\rangle$ are not present in equation 2.37 as the excitation of both ions into separate dressed states would require position-dependent laser fields with individual detunings for each ion.

Dressing the Rydberg state of ions by a microwave field has an additional application, as the polarizabilities of Rydberg S-states $\mathcal{P}_{n\mathrm{S}}$ and Rydberg P-states $\mathcal{P}_{n'\mathrm{P}}$ have opposite sign and the polarizability of the dressed state is given by

$$\mathcal{P}_{\pm} = \frac{1}{\sqrt{1+C_{\pm}^2}} \left( C_{\pm}^2 \mathcal{P}_{n'\mathrm{P}} + \mathcal{P}_{n\mathrm{S}} \right) \quad . \tag{2.38}$$

Driving microwave transitions between Rydberg states of trapped ions allows to engineer the magnitude and sign of the polarizability by the detuning of laser and microwave fields. A large polarizability can be utilized for accurately sensing electric fields and leads to large quadratic Stark shifts, while zero polarizability suppresses the modification of trap frequencies for Rydberg excitation [Pok20]. Especially the latter is crucial for lineshapes of Rydberg excitation, as shown in section 4.2, and realizing coherent Rydberg excitation without the need of motional ground state cooling [Zha20]. Thereby, the Rydberg blockade could be employed to a Doppler cooled ion string as entanglement method for quantum computation and simulation.

# 3

# All About Fields: The Experimental Apparatus

Following on the theoretical foundations of trapping Rydberg ions, the experimental apparatus is described. Generally, the ions are confined in a linear Paul trap and can be manipulated by electric fields and resonant laser sources. As Rydberg states are inherently sensitive to any external disturbances, e.g. electric fields, background pressure, black body radiation, etc., it is crucial to consider highly excited states already when designing the experimental apparatus. To minimize interactions of trapped ions with the background gas, the trap is placed in a vacuum vessel, which isolates the ions from the laboratory environment.

The first part of this section describes the ultra-high vacuum system including the segmented ion trap and its control electronics, while the second part focuses on laser sources for ion cooling, state-detection, -preparation and -manipulation. The relevant level scheme for two-photon excitation of Rydberg states in ionized Calcium is discussed and the frequency stabilization of both Rydberg lasers to a high finesse cavity is shown, which will improve future experiments.

## 3.1 A Trap for Stable Rydberg Ions

Obviously, the ion trap is a necessity for experiments on Rydberg ions to investigate state-dependent trap frequencies and distance-dependent interactions. Apart from reliable trapping of ion crystals, the Paul trap needs to have optical access, such that manipulation of the ion's internal and external degrees of freedom is possible. Electric field gradients in a linear Paul trap are generated by a combination of RF and DC voltages at dedicated electrodes, which are typically endcap electrodes for static axial confinement and a pair of two opposite radial electrodes for the oscillating field. Here, a segmented ion trap is employed, where the axial confinement is generated by individually controlled segments on the radial electrodes not used for the RF field. Analogous traps are well established [Wal12, Rus14, Kau17b] and shuttling based quantum computing is one of the promising approaches for realization of a scalable quantum computer [Kie02, Hil21]. In such a system, ion crystals are manipulated by electric fields that shuttle, split, merge and swap ions within the trap volume. Thereby, it is possible to perform all laser operations on a sub-system of small ion crystals, while other ions are stored in interaction free areas. The established control of electric fields for a shuttle-based quantum computer is extremely helpful to manipulate the position of a Rydberg ion inside the trap, to mitigate - or specially engineer - energy shifts due to the quadratic Stark effect.

The employed linear segmented Paul trap consists of 11 gold-coated electrode pairs for ion trapping by DC voltages and one electrode pair for the RF drive, symmetrically arranged around the trap axis [Fel16]. The electrodes are alternately oriented in a X-configuration, where the angle between electrodes is 90° and the distance of opposing electrode surfaces is 1500 µm. Throughout this thesis, an euclidean coordinate system is fixed to the trap axis with $x(y)$ referring to directions along the DC(RF) electrodes and $z$ lies along the trap axis. Due to symmetry, the confining effects on the ion are often generalized to radial $(x, y)$ and axial $(z)$ directions. The segments on the DC electrodes are separated by insulating gaps of 30 µm, while the width of the segments itself varies from 500 µm for the inner five segments to 1000 µm for each of the outer three segments on either side. A picture of the trap is shown in figure 3.1, where one DC and one RF electrode are visible. The gold coating on the electrodes leads to a high reflectivity, such that the insulating gaps of the DC electrode appear to be on the RF electrode as well, even though only a single conducting plane is present. However, the RF electrodes are cut in the same shape as the neighboring DC electrodes to generate as symmetric trap fields as possible. Additionally, the trap is equipped with compensation electrodes along the radial directions (shown in green), such that the ion can be positioned anywhere in the radial plane. Pierced endcaps (purple) terminate the trap volume along the axis, but allow optical access and can be individually controlled to provide axial confinement, which does not interfere with electric fields along the radial directions. The hole for optical access has a diameter of 1000 µm, which is smaller than the distance between two opposing electrodes and effectively shields the radial parts of the ion trap from any stray light shining along the axial direction. This prevents the intense laser for two-photon Rydberg excitation described in section 3.2, to generate electron-hole pairs in the gold coating of the radial electrodes leading to uncontrolled electric stray fields. Typically, the confining potentials are generated by

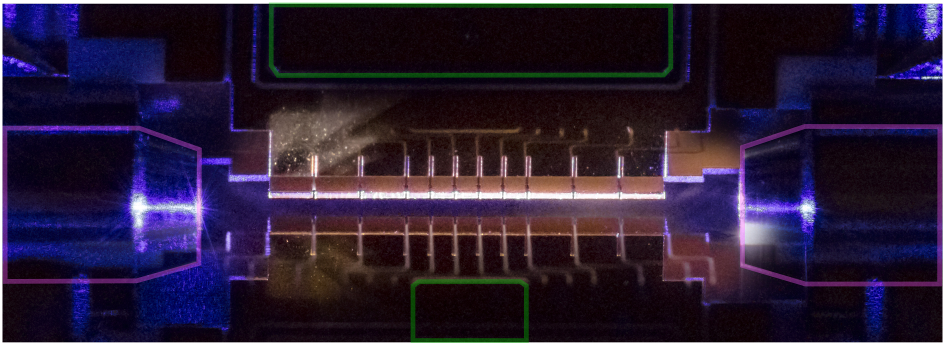

**Figure 3.1:** Radial view on the segmented ion trap with focus on DC (bottom) and RF (top) electrodes. Because of the reflective gold-coating, the RF blade appears to be separated by insulating gaps, but only the cutouts are real to provide a high radial symmetry. The segment sizes vary between the inner and outer regions of the trap, as described in the text. Compensation electrodes and endcaps for additional electric field control in all directions are highlighted in green and purple, respectively.

the segments, and the endcaps are rarely used to shift the ion position along the trap axis.

The ion trap is separated into an experimental zone spanned by the inner five segments and two dedicated loading zones consisting of three segments each at either side of the experimental zone. Neutral Calcium atoms are brought into the trap volume by resistive heating of a thin walled tube, which is filled with Calcium granule and pointing towards the trap center. However, the neutral Calcium might stick to the electrodes upon impact and create shorts by bridging the insulation gaps on the RF and DC electrodes or at least create electric stray fields due to surface inhomogeneities. This is mitigated by a set of two apertures, such that the neutral Calcium can only reach the trap volume via the outer segments, where it is ionized by a set of lasers described in section 3.2. To further reduce electric stray fields inside the trap by Calcium deposit, the flux of atoms can be blocked by a stainless steel sheet attached to a rotary feedthrough on the vacuum vessel. Once the neutral atoms are ionized, they can be trapped by the outer segments and successively shuttled into the experimental zone via suitable voltage ramps on the DC electrodes.

## Voltage Control for Ion Trap Operation

Confining and shuttling ions in this trap as well as performing more complex operations on ion crystals require high control over the applied electric fields. The asymmetric RF drive (applied only to the RF-electrodes) is provided by an analog frequency generator and impedance matched to the Paul trap by a helical resonator. In between, the amplitude of the RF field is adjusted by a voltage controlled attenuator and a high power amplifier to reach peak-peak amplitudes up to $U_\mathrm{RF} = 350\,\mathrm{V_{pp}}$ at a drive frequency of $\Omega_\mathrm{RF} \approx 2\pi \cdot 15\,\mathrm{MHz}$. The latter is measured by a capacitive divider at the output of the helical resonator and can be used in the future for voltage stabilization of the applied RF drive. A continuous switching of RF amplitudes is used throughout this thesis for different electric field configurations, which allow fast ion loading, successive transport and strong confinement for Rydberg excitation. Resulting radial trap frequencies $\omega_{x,y} > 2\pi \cdot 2\,\mathrm{MHz}$ are possible, but the segmented trap geometry leads to separated mode frequencies with typically $\omega_y > \omega_x$. In general, the splitting of the two radial frequencies can be tuned by an overall offset voltage applied to all DC electrodes, such that also degenerate mode frequencies are possible.

The segmented DC electrodes are controlled by an arbitrary waveform generator (BERTHA), developed in-house [Kau20]. This allows for up to 80 individual output channels with voltages of $\pm 40\,\mathrm{V}$ at a resolution limit of $1.3\,\mathrm{mV}$. Voltage updates are possible every 480 ns, which is sufficient for fast transport of ion crystals between different segments. However, the time resolution is no concern for most of the experimental results presented in this thesis and additionally, the applied voltages are filtered by custom 50 kHz low-pass filters. This attenuates high frequency disturbances close to the vacuum vessel to reduce ion heating by electrical noise [Sed18]. In vacuum, every DC electrode is additionally filtered to reduce the amount of RF signal picked up and fed back to the voltage control. BERTHA allows for individual addressing of all DC electrodes, but typically symmetric voltages on the segments are used for trapping ions, such that electrode pairs on opposing blades have the same voltage. Additionally the static field confining the ions is adjusted by adding a constant voltage on all DC electrodes to tune the ratio of radial trap frequencies. Applying a voltage with opposite sign on opposing blades allows to move the ion along the radial plane and to overlap static- and RF-field nulls, which becomes important for state preparation and Rydberg excitation, see section 4.1. Typical operation voltages are $-15\,\mathrm{V}$ on both opposing electrodes corresponding to the trapping segment, which generates an axial trap frequency of $\omega_z \approx 2\pi \cdot 1\,\mathrm{MHz}$. All other trap electrodes are supplied with a constant voltage of 20 V to enhance the symmetry of radial modes, and around $\pm 40\,\mathrm{V}$ are applied on the dedicated compensation electrodes. The endcaps are connected to prevent floating reference potentials, but kept at 0 V.

Note, after initial trapping and first successful experiments one of the segment electrodes shortened to ground, such that additional requirements for voltage control

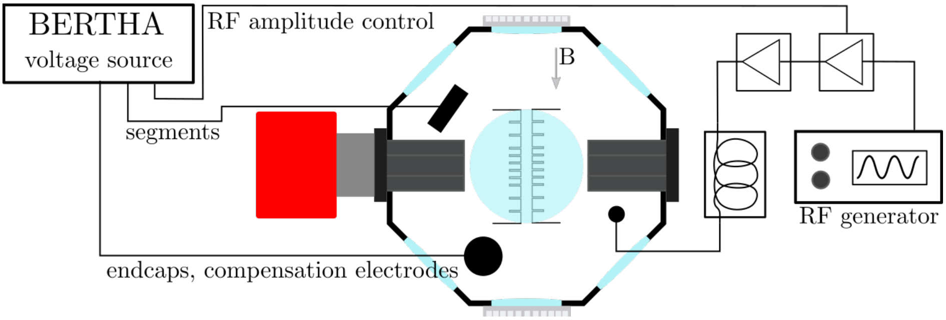

**Figure 3.2:** Schematic view of the ion trap inside the vacuum vessel with all relevant electrical connections for generation of the trap fields. The permanent magnets (light gray) combined with the ion pump (red, gray) provide a magnetic field along the trap axis. See text for details.

became necessary. The electrode is positioned next to one of the loading regions and consecutively shuttling the ion above the grounded electrode needs support from neighboring segments. Anyway, efficient shuttling of the ion from one side to the other side of the grounded electrode with modified voltage ramps is possible and the short does not permit the initial experiments on two-photon Rydberg excitation. Using this trap for more elaborate measurements for quantum simulation or performing quantum gates with high fidelity still needs to be evaluated.

## The Vacuum Vessel

Stable trapping of ions over extended periods of time is only possible if the ions are undisturbed from the environment and do not collide with any particles. Therefore, the ion trap is placed inside a vacuum vessel for ultra high vacuum, such that the lifetime of a trapped ion is not limited by background gas collisions. Such a vacuum system requires especially good optical access for state detection and manipulation with lasers, while providing necessary feedthroughs for applying control voltages. The trap is oriented within the vacuum chamber, such that the trap axis is aligned with two opposing viewports as presented in figure 3.2. This configuration allows individual laser addressing of the ion's radial and axial modes. The vacuum inside the chamber is maintained by a passive ion-getter pump (NEXTorr Z200, SAES) and a chemically active carbon filter (CapaciTorr Z200, SAES) for hydrogen adsorption. The background pressure is typically $< 2 \cdot 10^{-11}$ mbar. Having the ion-getter pump close to the ion comes with the disadvantage of a high parasitic magnetic field. A magnetic field at the ion is necessary to create sufficient Zeeman splitting to resolve individual quadrupole

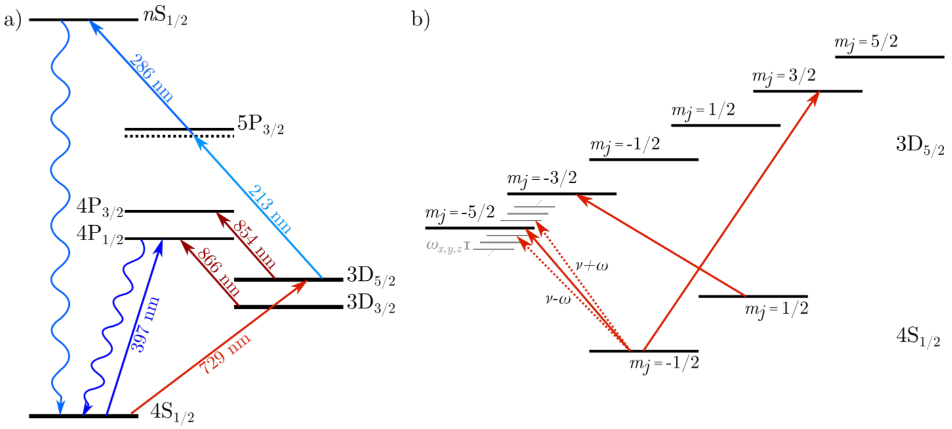

**Figure 3.3:** Energy diagram of the relevant electronic states of $^{40}$Ca$^+$. a) Shows laser transitions for cooling, state detection, state preparation and Rydberg excitation. b) Zeeman structure on the narrow $4S_{1/2} \rightarrow 3D_{5/2}$ transition for coherent control including motional sidebands (gray). Frequently used transitions are highlighted as red arrows.

transitions, while the direction of the magnetic field modulates the coupling of polarized light to the trapped ion. The magnetic quantization axis is provided by two sets of permanent magnets outside of the vacuum chamber in combination with the pump assembly. A total magnetic field of $B_z \approx 5.5\,\mathrm{G}$ points dominantly along the trap axis and is measured directly with the ion in section 4.1.

## 3.2 Laser Sources for Electronic State Manipulation

Ions are loaded into the trap by photo-ionization of the neutral Calcium beam from the oven. Respective laser sources near 423 nm and 375 nm are blocked after successful ionization by a mechanical shutter to avoid stray light in the trap volume. The level scheme of $^{40}$Ca$^+$ with the wavelengths used for cooling, state detection, state preparation, and Rydberg excitation is presented in figure 3.3a). Figure 3.3b) presents the Zeeman substructure of the $4S_{1/2} \rightarrow 3D_{5/2}$ transition driven by a laser near 729 nm.

### Cooling and Detection

Once the ion is trapped inside the 3D harmonic potential it can be cooled to low temperatures using various techniques. Here, Doppler cooling is employed with a laser near 397 nm close to the atomic $4S_{1/2} \rightarrow 4P_{1/2}$ transition and the angle of 45° between the laser and all trap axes allows for cooling of all motional modes of the

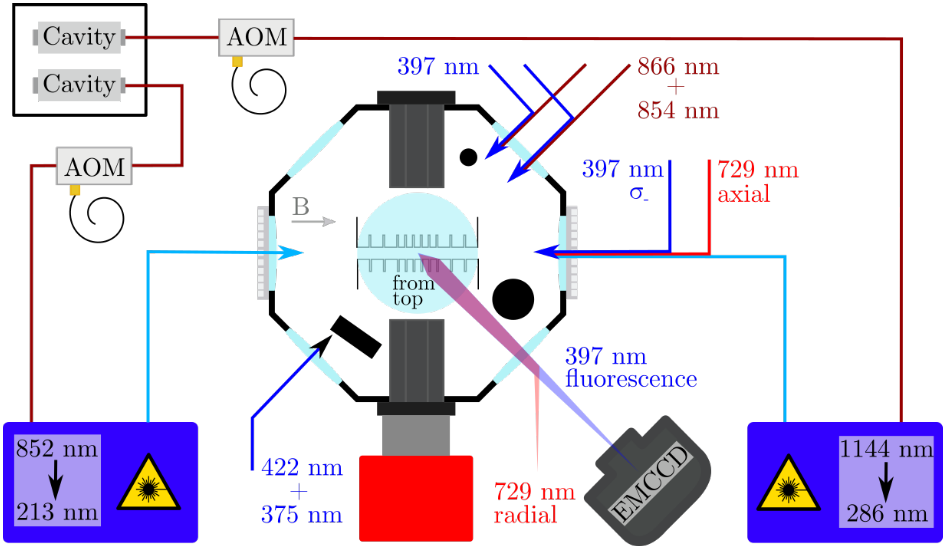

**Figure 3.4:** Schematic view of the relevant lasers for cooling, state detection, state preparation and Rydberg excitation of $^{40}\mathrm{Ca}^+$ and their directions with respect to the ion trap. The imaging setup is accessing the ion trap by the top viewport of the vacuum vessel. The fundamental wavelengths of the Rydberg excitation lasers are frequency stabilized via RF driven AOMs to a low finesse cavity.

single ion at once, see figure 3.4. Spontaneously emitted photons from the $4\mathrm{P}_{1/2}$ state with a lifetime of 6.9 ns [Het15] are imaged onto an electromagnetic charge coupled device (EMCCD) camera, such that the trapped ion can be monitored in real time. Details of the imaging resolution for larger ion crystals are given in section 7.1.

Additionally, a light field near 866 nm depopulates the $3\mathrm{D}_{3/2}$ state. This is required for permanent Doppler cooling and fluorescence induced ion detection as population trapped in the metastable state interrupts cycling on the cooling transition. Similarly, a laser near 854 nm depopulates the metastable $3\mathrm{D}_{5/2}$ state. During Doppler cooling this laser source illuminates the ion, but is switched off for state detection. Hence, a bright ion is visible if the ion is in the electronic ground state $4\mathrm{S}_{1/2}$ and no fluorescence is observed for an ion in $3\mathrm{D}_{5/2}$. Doppler cooling and state detection take a few ms during the experimental sequences.

As the trap geometry allows for separate loading and experimental zones, two parallel beam paths of cooling lasers are used to individually address ions in the outer trap segments or the central segments, respectively. Although the ions are cooled and emit fluorescence in the loading zone before they are shuttled away, only ions in the central region of the trap are observable by the EMCCD camera without adjustments of the imaging system. A successful loading event can therefore only be detected after suitable voltage ramps on the electrodes.

## State Preparation and Qubit Control

For a given magnetic field the energy levels with different magnetic quantum number are split by the Zeeman effect. Direct transitions between different Zeeman sub-states of two electronic levels can be driven by using $\sigma_+$- or $\sigma_-$-polarized light, which change the magnetic quantum number by $\Delta m = \pm 1$. However, state selection is very sensitive to the overlap of magnetic field direction and laser propagation direction [Roo00] and constrains the experimental setup. Optical pumping with a $\sigma_-$-polarized laser near 397 nm drives the transition $4\mathrm{S}_{1/2,+1/2} \rightarrow 4\mathrm{P}_{1/2,-1/2}$. After several absorption and emission cycles, which only last a few µs, the ion is most probably found in state $4\mathrm{S}_{1/2,-1/2}$. Note, to avoid population being trapped in one of the dark states both infrared lasers are switched on during the optical pumping process.

With the possibility to initialize the ion in the sub-state $4\mathrm{S}_{1/2,-1/2}$ it is convenient to define this as one of the qubit states, namely $|0\rangle$. Consistently, one of the dark $3\mathrm{D}_{5/2}$ sub-states can be defined as $|1\rangle$ and the quadrupole transition near 729 nm coherently transfers population between states $|0\rangle$ and $|1\rangle$. The laser is locked to a high finesse cavity, such that the laser linewidth is below 1 kHz and individual transitions between different Zeeman sub-states can be resolved, which is depicted for the most relevant transitions within this thesis in figure 3.3b). The coupling strengths of the transitions with $\Delta m = 0, \pm 1, \pm 2$ are dependent on the angle between magnetic field, laser propagation direction and laser polarization [Roo00]. For the presented experiments two geometries are realized. On the one hand the light is propagating axially along the magnetic field direction and can thereby address transitions with $\Delta m = \pm 1$. This laser is sensitive to phonons along the axis but not affected by vibration along the two radial modes. On the other hand a second beam path is counter propagating the imaging system and entering the trap volume from a purely radial direction. The polarization of the beam is chosen, such that only transitions $\Delta m = \pm 2$ are accessible, as this allows for sideband cooling without constant reinitialization (see section 4.3). The latter geometry comes with two additional advantages, which are the access to radial phonon modes unperturbed by axial motion and the focus of the laser beam via the imaging objective. Thereby, focus sizes of $< 4$ µm individually address single ions in larger ion crystals. Repeatedly exciting the $\Delta m = -2$ transition from $4\mathrm{S}_{1/2,+1/2}$ with consecutive repump by 854 nm light can be used to prepare an ion in the $4\mathrm{S}_{1/2,-1/2}$ ground state.

## Rydberg Excitation

After successful initialization in the $3D_{5/2,-5/2}$ state by light near 729 nm a resonant two-photon process excites different Rydberg states depending on the transition frequency. Here, light fields near 213 nm and 286 nm couple transitions $3D_{5/2} \rightarrow 5P_{3/2}$ and $5P_{3/2} \rightarrow nS_{1/2}, nD_{3/2}, nD_{5/2}$, respectively. Both wavelengths are considered as deep ultraviolet (UV) radiation and are not produced by standard diode lasers as other wavelengths used in the experiment. They are commercially available, though. To generate light at such high energies two frequency doubling cavities for each laser setup are employed, which quadruple the light frequency from fundamentals of 852 nm and 1144 nm, respectively. Additionally, tapered amplifier systems before the first frequency doubling stages allow for final output power up to 15 mW for 213 nm and 100 mW for 286 nm. Both lasers are counter propagating along the axial direction with beam waists of $\approx$ 10 µm. This configuration is necessary to reduce the momentum transfer to the ion by absorbing one photon of each laser beam, such that the Doppler effect is almost canceled out. Also, propagation along the magnetic field direction allows for the use of $\sigma_+$-polarized light to enhance the excitation strength when starting from the $3D_{5/2,-5/2}$ state.

## Laser Control

In general, all light sources for manipulating the $^{40}\mathrm{Ca}^+$ ion are frequency stabilized either by locking the laser to an external resonator or directly reading out and adjusting the wavelength via a wavelength meter and software. The first method uses a fixed length spacer in vacuum with high reflectivity mirrors on either side, such that a light field is build up inside this resonator if the frequency of an incident laser matches the resonator mode. By modulating the incident light field and observing the back-reflected light it is possible to stabilize the laser. Details of setup and operation of such a resonator can be found in the Bachelor thesis of Ron Moller [Mol19], demonstrating the stabilization of both fundamental Rydberg excitation lasers. Additionally, all laser frequencies are measured by a wavelength meter to tune the lasers initially close to the atomic resonances and, for light near 423 nm and 854 nm, stabilize the laser frequencies via a digital PID regulation. The other laser sources require better frequency stabilization than the accuracy of the wavemeter (High Finesse, WSU-30, $\approx$ 30 MHz).

Relative frequency control with respect to the stabilized light field is obtained by the use of acousto-optical modulators (AOMs), which also allow for fast switching of laser pulses on µs to ms timescales. Within these devices the laser beam transverses a crystal (e.g. Quartz), onto which a RF is applied perpendicular to the laser propagation direction and builds a sound wave inside the crystal. Fulfilling the Bragg condition, the outgoing diffracted laser field is separated spatially and frequency wise from the undiffracted beam and can be modulated by the applied RF. Set up in a double-pass configuration, the diffracted laser beam is back-reflected by a mirror and transmits the crystal a second time. This has the advantage, that the AOM is used for fast and efficient light switching and the undiffracted part can be filtered out twice as good, such that no spurious light permanently illuminates the ion. Also, the RF drive of the AOMs allow a fine tuning of the laser frequency onto atomic transitions and the double pass increases the tunability, while no beam-pointing is observed on the ion. Apart from the deep UV lasers, all AOMs are set up in double-pass configuration. Here, the frequency control of the fundamental light for Rydberg excitation is emphasized, as the light is stabilized via double-pass AOMs onto a low finesse resonator. The AOMs allow for a detuning of the master laser and, therefore, an output frequency change for the UV beams of eight times the applied RF, such that systematic frequency scans of up to 400 MHz are possible. A summary of the laser configurations and the frequency stabilization of the Rydberg excitation lasers is shown in figure 3.4 and the first Rydberg excitation spectrum is shown in section 4.2.

## High Finesse Cavity for Rydberg Excitation

Stabilization of the fundamental wavelengths to a low finesse cavity merely minimizes drifts of the wavelength but does not reduce the laser linewidth below the diode bandwidth. Although both laser sources are already equipped with state of the art diode heads and current controls, the frequency quadrupling leads to final laser linewidths of 1 MHz each and limits future coherent excitation into Rydberg states. After the results of this thesis have been measured a new setup for frequency stabilization of both Rydberg fundamental wavelengths was constructed and characterized, such that future experiments will benefit from much reduced laser linewidth and improved long term reproducibility. Here, a commercial resonator with specified finesse $\mathcal{F} > 100\,000$ is implemented consisting of a set of mirrors with reflectivity of $R = 99.9998\%$ for 852 nm and $R = 99.9996\%$ for 1144 nm, respectively. The mirrors are spaced by a 10 cm glass-ceramic block with ultra low thermal expansion coefficient, such that the length of the cavity is fixed and the light field inside the mirrors (one planar and the other one curved with radius of curvature 50 cm) can be amplified due to the high reflectivity. The set of mirrors and spacer are supported by a thermal and vibration isolating structure and placed in a temperature stabilized vacuum chamber with pressures below $10^{-7}$ mbar. Light of both fundamental wavelengths is coupled into the cavity from the planar side and locked via the Pound-Drever-Hall method [Dre83] by modulating the current of the master oscillator with frequencies around 20 MHz. Furthermore, the AOMs for frequency scanning in the low finesse cavity setup are replaced by fiber coupled electro-optical-modulators (EOMs). These modulate the phase of the transmitted light field and generate additional sidebands at the drive frequency, typically up to several GHz. The EOM comes with the advantage, that the modulation bandwidth is larger than the free spectral range of the cavity, such that different Rydberg states can be accessed by choosing according drive frequencies and locking the modulated sideband to the cavity. Similarly, frequency scanning of the two-photon transition is possible by adjusting the drive frequency and does not require additional AOMs as in the low finesse cavity setup.

The high finesse cavity is characterized in two ways prior to Rydberg excitation with stabilized lasers. On the one hand, the temperature of the cavity is varied to measure the zero expansion temperature of the glass-ceramic spacer and on the other hand the finesse of the cavity is estimated by using the ring-down method [Gal20]. For both measurements at least one of the fundamental Rydberg laser sources has to be stabilized to the cavity and for simplicity light near 852 nm is used, as the available optical power meters, photo diodes and cameras to monitor the beam are more sensitive at the lower wavelength. The fundamental wavelength probe beam exits the laser enclosing and is split into a beam for wavelength measurement and the stabilization branch directed to the high finesse cavity, which is guided by the fiber-coupled EOM. Before entering the vacuum chamber to the high finesse cavity the beam passes a retardation plate and a polarizing beam splitter cube for the Pound-Drever-Hall technique. Additionally, a set of lenses match the beam shape to the cavity mode determined by curvature and spacing of the cavity mirrors, which results in a beam waist at the planar mirror of 230 µm. Referencing the beam to the cavity mode, the fundamental light obtains a linewidth given by the finesse of the cavity and is stabilized to the fixed mirror distance. Variations in the spacer length arise mainly due to small temperature changes, but the choice of material can reduce the coefficient of thermal expansion close to zero for a given temperature. This is found by changing the temperature of the cavity system and probe the frequency variation of the stabilized light field. Typically, one would use a high accuracy wavelength meter for this task, but the absolute accuracy of the available device is much worse than expected frequency shifts of a few MHz, such that the trapped ion is used as a frequency reference. For any

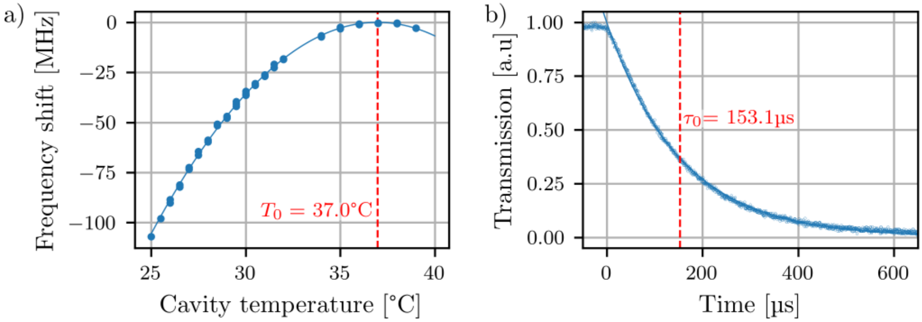

**Figure 3.5:** a) Measurement of the zero expansion temperature $T_0$ by varying the cavity temperature and measuring the atomic 3D→5P transition with the fundamental beam at 852 nm locked to the high finesse cavity. b) Ring-down measurement of the light field inside the cavity with decay constant $\tau_0$ to estimate the finesse.

cavity temperature, the $3D_{5/2} \rightarrow 5P_{3/2}$ transition (see section 4.2) is measured using the UV-AOM and shifting the laser frequency by the EOM drive frequency. This method is extremely sensitive as the temperature-dependent shift of the stabilized frequency is multiplied by the frequency quadrupling of the UV laser system. Figure 3.5a) depicts the measurement of the zero expansion temperature resulting in an optimal working point of 37.0(2)°C, larger than room temperature and controllable by heating elements. As the temperature controller specifies a temperature stability within 10 mK, the long term fluctuation of UV frequencies should be reduced to less than 22 kHz, limited by the uncertainty of the zero expansion temperature.

In a second measurement the finesse of the cavity is estimated by the ring-down method [Gal20]. Here, the decay of the light field inside the cavity is observed, when the incident beam is either blocked or shifted non-resonant to the cavity. A high finesse of the cavity correlates with a long lifetime of the light field, which is traveling between the high reflectivity mirrors. As the optical power inside the cavity is not accessible without immediately absorbing the light, one uses the resonant transmission signal, which is proportional to the leakage of the curved mirror. Only if the light frequency is resonant to one of the cavity modes, the optical field inside the cavity is enhanced and the transmitting field can be measured by a fast photo diode. Figure 3.5b) shows the exponential decay of the cavity light field after shifting the laser frequency, initially stabilized to the cavity mode. A fit of the decay constant yields an experimental finesse of $\mathcal{F}_{\text{exp}} = 1.441(2) \cdot 10^6$ below the estimated finesse of $\mathcal{F}_{\text{design}} = {}^{\pi\sqrt{R}}/_{1-R} = 1.8 \cdot 10^6$, given by the specified reflectivity. Deviations can be explained by mirror coatings showing a smaller reflectivity than designed or a roughness of the mirror surfaces. Also, imperfect alignment of the cavity mirrors might reduce the finesse. Overall, the achieved finesse is much better than the specified finesse of $\mathcal{F} > 100\,000$ and the linewidth of both laser sources for Rydberg excitation can be drastically reduced below the natural linewidth of Rydberg states for future experiments.

# 4

# How to Become Huge: Excitation of Rydberg States and Observation of Non-Negligible Polarizability

The dynamics of a trapped ion is given by the Paul potential with laser sources controlling internal and external degrees of freedom. Excitation of Rydberg states leads to modifications of trap frequencies and systematic energy shifts depending on applied electric fields, which allow for an extraction of Rydberg state properties. For unperturbed spectroscopy (see section 4.2), a single experiment is realized by repeating the same sequence multiple times and averaging the result, before one parameter is varied and the sequence starts anew. Scan parameters are - among others - specific laser frequencies, pulse times or applied voltages to trap electrodes. Individual steps within such a sequence can be fine tuned and some parameters need permanent adjustments to optimize the final result, while other parameters are kept constant for longer times. However, to systematically compare measurements from different days it is necessary to have certain calibration methods for the most sensitive parts of the experiment.

In this section fluctuations of electromagnetic fields by external and internal sources of the ion trap are discussed and characterized. Residual fields are compensated using external measurement tools or the ion itself as a sensor and the stability of laser operations are optimized by pulse shaping and optimized trap potentials. Controlling external sources, the excitation of the intermediate $5P_{3/2}$ state and successive transition into Rydberg states is presented, such that the principal quantum number scaling of the depopulation rate via Rydberg excitation can be extracted. Energy shifts for Rydberg states are included to model the resulting Rydberg transition lineshapes and discussed in terms of the ion confinement within the Paul trap. Afterward the excitation efficiency is enhanced by sideband cooling and further experiments show that the timescale for excitation can be reduced below the Rydberg state lifetime, possibly leading to observation of strong Rydberg interactions between multiple ions.

## 4.1 Control of External and Internal Fields

Electromagnetic fields inside the ion trap determine the dynamics of ionic motion and electronic state transfer by lasers. The internal fields relate to the electric fields provided by the Paul trap and magnetic fields originating from permanent magnets and ion-getter pump. However, the lab environment contains numerous electronic parts, power supplies, magnetic materials and people moving in the vicinity of the experiment, such that external fluctuations of electromagnetic fields need to be considered. By suitable application of electric and magnetic fields the external fluctuations can be compensated for. Due to the dimensions of the used ion trap, the experienced fields are strongly dependent on the axial position of the ion and the results are presented only for the central trapping zone, but similar measures are implemented for ions in the loading zone.

### Compensation of Magnetic Field Drifts

The quantization axis of the trapped ion is given by the magnetic field, which is mainly originating from permanent magnets attached to the outside of the vacuum chamber and the ion-getter pump. Fortunately, the magnetic field directions of both magnet configurations overlap to a large degree and the magnetic field is coarsely aligned with the axis of the trap, which is confirmed by measurements with $\sigma$-polarized light. However, due to the close proximity of vacuum pump and ion it is very difficult to quantify the angle of magnetic field with respect to the trap axis. Both, direction and magnitude of the magnetic field influence the trapped ion and the coupling strength between quadrupole transition and ion is modulated by the overlap of beam propagation direction, laser polarization and quantization axis. For the two laser propagation directions presented, transitions with a difference in magnetic quantum number of $|\Delta m| = 1, 2$ are possible, while $\Delta m = 0$ is strongly suppressed. The magnitude of the magnetic field shifts the energy levels of the trapped ion by the Zeeman effect in the order of $\approx$ 10 MHz. As the linewidth of the atomic $4\mathrm{P}_{1/2}$ state is even larger ($\approx$ 22 MHz), transitions for cooling and repumping are not strongly affected by the Zeeman structure and efficient cooling with a single frequency laser field is possible. Contrary, the narrow transition near 729 nm resolves transitions between individual Zeeman sub-levels.

For state preparation, typically several laser pulses near 729 nm are employed, therefore it is important to control the stability of the magnetic field at the ion. External sources of magnetic fields, e.g. power supplies, elevators, other experiments or the

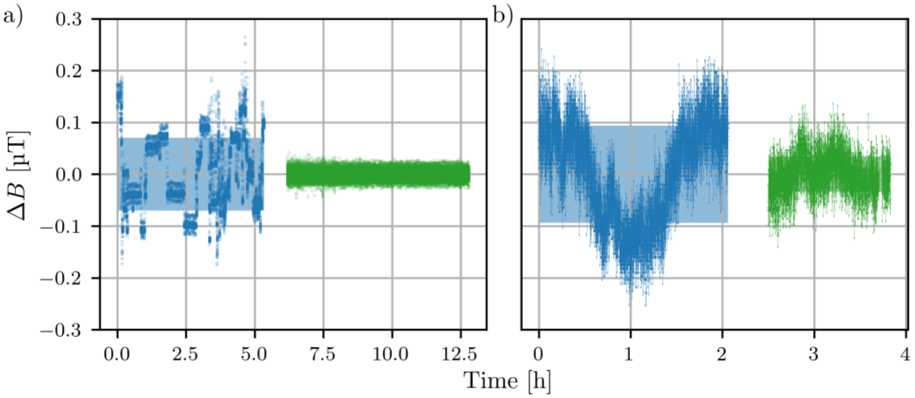

**Figure 4.1:** a) Magnetic field variations $\Delta B$ along $z$ measured by a flux gate sensor without (blue) and with (green) active stabilization by Helmholtz Coils. Shaded area denote the standard error, which is smaller than the spread for the green data points. In b) the field fluctuations are measured directly by the ion using a Ramsey method as described in the text. a) And b) were recorded at different days.

earth magnetic field need to be considered and compensated. Within the Bachelor thesis of Jean Philip Filling [Fil21] a set of three square Helmholtz coils was placed around the experiment, each with an axis length of around 2 m. The coil current is regulated by a Raspberry Pi equipped with a magnetic three axis flux gate sensor, which is placed next to the vacuum vessel. A digital PID control enables individual feedback of the coil current onto the flux gate sensor reading along the respective direction. Limited by the time resolution to set the coil currents at 2 Hz, the magnetic field at the sensor position can be stabilized. In figure 4.1a) the sensor measurement along $z$ is presented without (blue) and with (green) stabilization, where an improvement of magnetic field stabilization (here, standard deviation $\sigma$) is found:

$$\frac{\sigma_{\text{unstabilized}}}{\sigma_{\text{stabilized}}} = \frac{0.070\ \mu\text{T}}{0.010\ \mu\text{T}} = 7.0 \quad .$$

The magnetic field fluctuations measured by the flux gate sensor show regions, where the magnetic field drifts over time, but also suddenly jumps between temporary stable magnetic field values. Both effects are suppressed by regulating the coil current onto the sensor reading, such that the magnetic field along the quantization axis of the ion is stabilized.

Also, the ion itself can be used as a sensor to measure the magnitude of the magnetic field. The ion is most sensitive to variations of the magnetic field along $z$, pointing to a good overlap of quantization axis and trap axis. By resolving two transitions between the $4S_{1/2}$ and $3D_{5/2}$ electronic states and extracting the Zeeman shift, the magnetic field strength can be directly measured. Additionally, small frequency differences due to magnetic field inhomogeneity can be probed accurately using the Ramsey method [Rus17], where a phase accumulation due to external fields is projected onto the qubit states $|0\rangle$ and $|1\rangle$. In detail, such a measurement consists of 2 sequences starting with a $\pi/2$-pulse on the $4S_{1/2,-1/2} \rightarrow 3D_{5/2,-5/2}$ transition followed by a waiting time of several µs. Afterward a second $\pi/2$-pulse, phase shifted ±90° with respect to the first pulse, manipulates the internal state and the phase evolution can be read out by the bright/dark state probability. The difference in population measured for the two laser phases ±90° is related to the detuning from the resonance frequency and therefore a suitable measurement for the frequency stability. By adjusting the waiting time in between the two laser pulses, the sensitivity to magnetic field fluctuations can be tuned. Repeating the same sequence at a given laser frequency allows to extract fluctuations in magnetic field strength at the ion position and confirms a stabilizing effect of the external magnetic field regulation on the trapped ion as shown in figure 4.1b). The regulation of the magnetic field allows to stabilize the qubit transition frequency to $\sigma_{\text{stabilized}} = 0.9$ kHz. Even though data from the flux gate sensor and the ion are recorded at two different days, the fluctuations are in the same order of magnitude. The periodic behavior of the non-stabilized magnetic field measured by the ion is originating from a different experiment in the institute working with high magnetic fields, but the regulation is able to compensate for external varying fields.

Apart from stabilizing the magnetic field and thereby stabilizing the transition frequencies of the quadrupole transition, the population transfer between the $4S_{1/2}$ and $3D_{5/2}$ states may be further enhanced by pulse shaping of the laser field near 729 nm. Throughout most of the experiments presented here, the initialization into the dark state is done by a rapid adiabatic passage (RAP) pulse [Vit01]. This modulates the frequency and amplitude of the laser throughout the pulse duration, which is less sensitive to fluctuations compared to a square pulse.

## Trap Heating by Varying the RF Drive Amplitude

As the ion is trapped inside the harmonic pseudo potential spanned by the static and oscillating electric fields, the vibrational mode frequencies of the ion are suitable to measure long term stability of the trapping potential. All static voltages for segments, surrounding compensation electrodes and end caps are supplied by BERTHA and no fluctuations on the axial vibrational frequency are observed, even after switch-

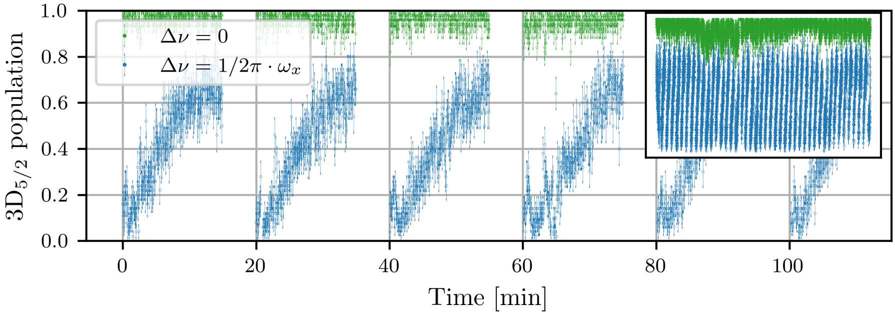

**Figure 4.2:** Excitation probabilities of the blue sideband for mode $\omega_x$ (blue) and resonant $4S_{1/2,-1/2} \rightarrow 3D_{5/2,-5/2}$ transition (green) for systematic variation of the RF drive amplitude $V_{\mathrm{RF}}$, see text for details. A difference in excitation strength for the sideband is caused by the varying vibrational mode frequency throughout the experiment and a thermalization is observed for every cycle of 20 minutes. The inset shows the reproducibility of this scan over several hours.

ing between different DC configurations back and forth. Generally, the axial confinement can be fine tuned by static voltages and continuously controlled between $\omega_z/2\pi \in [0.15, 1.05]$ MHz. The radial confinement is dominated by the applied RF and the vibrational frequencies along radial directions tend to drift over time, especially when varying the amplitude for short periods. Figure 4.2 shows a stability measurement of one of the radial frequencies by systematically varying the RF amplitude between two voltage sets (schematically shown in black). Here, a typical RF voltage for single ion experiments is applied for 15 min and afterward the amplitude reduced 5 min to the voltage set for ion loading. Due to low secular frequencies the measurement method is not sensitive in the latter potential setting and only high RF amplitude data is presented. The frequency stability is recorded by probing the $4S_{1/2,-1/2} \rightarrow 3D_{5/2,-5/2}$ transition with pulse timing of 20 µs and a frequency detuning of $\Delta\nu = \omega_x/2\pi$, namely the first blue sideband of the radial mode along $x$. For a Doppler cooled ion the probability to find the ion in a dark state after such a laser pulse is expected to be around $50\% - 60\%$, but the measured probability only matches the expectations after several minutes within the desired electric potential. To attribute this effect to shifts in the secular frequency, the blue sideband (blue) is probed interleaved with the resonant transition (green), which shows almost full population transfer throughout the measurement. Although, the ratio between the used voltage sets varies for different experiments, usually the RF amplitude applied for loading is approximately three times smaller compared to the RF amplitude used for experiments including

Rydberg excitation. The repeating pattern in the presented graph can be explained by temperature changes in the RF circuit, consisting of the amplifier, the helical resonator or the trap blades itself. Specifically, whenever the amplitude is switched to lower voltages the heat load for the RF-blades, surrounding support structure and cables decreases and the electric field confining the ion gets altered. Reverting the RF amplitude leads to a slow recovering of the initial mode frequency and this cycle is reproducible for long times, as shown in the inset of figure 4.2 with data recorded over several hours. Further measurements indicate that reducing the time, where only a low RF amplitude is applied to the trap, also reduces the fluctuations in vibrational frequency. Concluding, the ion trap itself seems to operate stable as long as the drive parameters are not constantly varied. Even if the RF amplitude is reduced for ion loading, the experiments can be conducted with unchanged parameters after a certain wait time depending on the loading speed.

## Compensation of Excess Micromotion

Additional to electric field stability, it is crucial to place the ion at the center of the harmonic potential, where the nulls of RF and DC fields overlap and excess micromotion of the ion is negligible. This is especially important when exciting ions to Rydberg states, as it reduces the experienced quadratic Stark shift as well as phonon changing transitions [Hig19], but also ions in low-lying electronic states are affected by a modulation of the light-matter interaction [Kel15]. The periodic motion of the ion inside the oscillating quadrupole field gives rise to first order Doppler shifts $\Delta\nu = \beta\Omega_{\mathrm{RF}}$, effectively varying the phase of laser sources exciting the ion. For a modulation index $\beta > 0$ sidebands on the laser transitions arise with a detuning of $\Omega_{\mathrm{RF}}$ and the resolved sideband method allows to measure the residual electric field amplitude $E_{\mathrm{RF}}$ at the position of the ion:

$$E_{\mathrm{RF}} = \beta \frac{\lambda M \Omega_{\mathrm{RF}}^2}{2\pi Q} \quad . \tag{4.39}$$

Here, $M$ and $Q$ are the ion's mass and charge, $\lambda$ is the wavelength probing the micromotion sideband. The ratio of excitation strength of the first micromotion sideband $\Omega_{\mathrm{MM}}$ compared to the carrier transition $\Omega_0$ determines the modulation index

$$\beta = 2\frac{\Omega_{\mathrm{MM}}}{\Omega_0} \quad . \tag{4.40}$$

Note, the resolved sideband method requires access to a narrow laser transition with the laser propagation parallel to the axis of micromotion. Within the presented setup

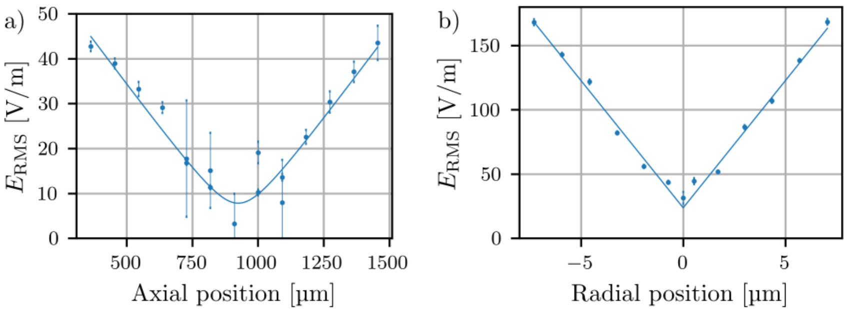

**Figure 4.3:** Measured residual electric field along a) axial and b) radial direction by displacing the ion inside the trap volume. Solid lines show fits to the data, see text for details.

a laser near 729 nm allows to extract residual electric fields along the axial and radial directions, where for the latter fields along $x$ and $y$ are combined. To compensate in the radial direction perpendicular to the 729 nm laser, either another laser beam or a different method has to be employed. Here, the first order Doppler shift on the dipole transition near 397 nm is utilized, where an increase in excess micromotion leads to an enhanced fluorescence emitted from the ion. A combined measurement of the modulation index and the emitted fluorescence, while moving the ion radially through the trap via the compensation electrodes, allows to compensate excess micromotion along both radial trap axes.

For axial compensation, the ion is moved along the trap axis by corresponding voltages at the segments and measuring residual field strengths using the resolved sideband method. To quantify the extracted residual electric field at each ion position, a function $E = \sqrt{a(z - z_0)^2 + E_0^2}$ is fitted to the data [Roo00]. Results are found in figure 4.3a), where the ion position for minimal axial micromotion is found about $z_0 = 0.925(4)$ mm away from the geometrical trap center. With segment sizes of 500 µm in the experimental region, the ion is trapped almost two full segments away from the designed trap center. This asymmetry and the finite residual field might originate from slight misalignment of the trap electrodes with respect to each other, e.g. an off-centered end cap or an angled RF blade. Also, it could be an effect of the observed ground connection for one segment electrode, which is located on the opposite site at approximately $-z_0$. Repeating the measurements for different ion confinements and with several months in between, indicates, that the axial micromotion is stable and independent of the static trap field. Once compensated, the residual RF field along the axial direction is almost negligible for the linear Paul trap and *root-mean-squared* (RMS)-fields below 10 V/m are observed over a range of more than 100 µm with a minimal residual electric field of $E_{\mathrm{RMS}}^{(\mathrm{ax})} = 7.8(5)$ V/m. Thereby, also larger ion crystals do not experience considerably different micromotion for individual ion positions of a long ion string. Note, displacing the ion along the axis allows for a controlled modification of the trap potential and enables polarizability measurements of Rydberg states in electric fields [Mok19].

Along the radial direction a full measurement of the residual radial field is analogously recorded and presented in figure 4.3b). As radial field gradients are typically 1-2 orders of magnitude larger than the axial field gradients, excess micromotion can become significant even for small radial displacements of the ion from the RF null. By varying the ion position, a minimal residual electric field of $E_{\mathrm{RMS}}^{(\mathrm{rad})} = 24(1)$ V/m is extracted from the fit. However, the radial ion position varies up to 1 µm on timescales of a few hours, such that residual electric field fluctuations of +100% are observed and a routine for fast and systematic radial compensation is necessary. Firstly, the ion is illuminated by a laser near 397 nm to find minimal fluorescence due to the Doppler effect along the laser direction. Secondly, the direction perpendicular to the Doppler cooling laser is probed by the resolved sideband method using the radial 729 nm laser. A combined measurement allows for compensation of residual electric fields along both radial directions within a few minutes. In total, both methods for axial and radial field compensation reduce the residual electric fields below 25 V/m. This minimizes modulation of the interaction between laser and ion as well as the quadratic Stark effect, which shifts the energy levels of Rydberg states in the order of MHz due to the large polarizability.

## 4.2 Rydberg Excitation Lineshapes in the Presence of Ionic Motion

In ionic systems the valence electron is bound much stronger to the positively charged core compared to their neutral atomic counterpart and consequently much more energy is required to excite Rydberg states. This energy is $\Delta E \approx 10\,\mathrm{eV}$ for $^{40}\mathrm{Ca}^{+}$ and corresponds to a laser with wavelength near 122 nm. Even though experiments with so called vacuum-ultraviolet light have been performed and successful Rydberg excitation was observed [Fel15, Bac16], maintenance of the laser system and limitations to beam guiding and beam optics advocate the use of a resonant two-photon excitation scheme. Here, deep UV laser fields near 213 nm and 285-289 nm couple the transitions $3\mathrm{D}_{5/2} \rightarrow$

$5P_{3/2}$ and $5P_{3/2} \rightarrow nS_{1/2}$, respectively, where the tunable wavelength of the second laser field allows for individual addressing of Rydberg states. From there, the ion decays predominately into the $4S_{1/2}$ ground state. In this way, we reveal a successful Rydberg excitation, if the $3D_{5/2}$ state is depopulated and we detect the state dependent fluorescence, either dark for $3D_{5/2}$ or bright for $4S_{1/2}$.

Assisted by the intermediate $5P_{3/2}$ state, high excitation rates and strong coupling to Rydberg states can be achieved with commercially available laser sources. However, an actual excitation of the intermediate state needs to be avoided, as the lifetime is much shorter (34.8 ns [Saf11]) than subsequent excitation into Rydberg states with the current Rabi frequencies in the order of a few MHz. For a successful transition into Rydberg states scattering from $5P_{3/2}$ is suppressed by either choosing a sufficient frequency detuning of the first excitation laser from the atomic resonance or by modifying the pulse shape of the laser sources, e.g. by *stimulated rapid adiabatic passage* (STIRAP) [Ber19]. Varying the laser frequency of the second light field allows to excite Rydberg states and observe the transition lineshape to study their properties with respect to the ion's motional state, interactions to neighboring ions and to surrounding trap fields. A second approach to measure transition frequencies into Rydberg states utilizes the resonant coupling of light to the atomic levels and probes the corresponding energy shift. This method is referred to as *quantum interference* (QI) and will be discussed in more detail later. The results of this section are published in ”Rydberg series excitation of a single trapped $^{40}Ca^{+}$ ion for precision measurements and principal quantum number scaling” [And21].

Prior to interaction with the deep UV lasers, the ion is Doppler cooled for several milliseconds. In a first step, the electronic ground state $4S_{1/2,-1/2}$ is populated by a series of $\pi$-pulses on the transition $4S_{1/2,1/2} \rightarrow 3D_{5/2,-3/2}$ and consecutive quenches by light near 854 nm. Afterward, a single RAP pulse excites the ion into the metastable qubit state $|0\rangle = 3D_{5/2,-5/2}$ with an efficiency $> 95\%$ dependent on parameters as trap configuration or ion temperature. Before exciting Rydberg states, the intermediate $5P_{3/2}$ state is probed. The laser near 213 nm is illuminating the ion along the trap axis and can be switched by a single-pass AOM. High optical intensities and correspondingly strong excitation rates are achieved by focusing the laser to a beam waist of 5 µm at the ion position. To tune the laser frequency onto the atomic resonance, the fundamental wavelength near 852 nm is controlled via two methods. For larger frequency variations, the length of the reference cavity is tuned by a piezoelectric actuator glued to the cavity mirror itself, which leads to a frequency change of the stabilized light field. However, these actuators tend to drift for long times after a change of the control

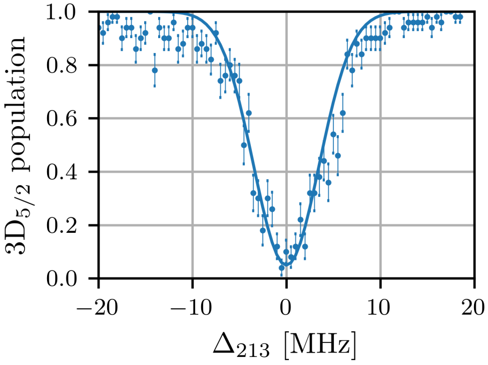

**Figure 4.4:** Depopulation of the $3D_{5/2}$ state by excitation of the intermediate $5P_{3/2}$ state as a function of laser detuning $\Delta_{213}$ from the atomic resonance. An excited ion decays to the electronic ground state and can be observed via fluorescence detection.

voltage, such that calibrated and reliable frequency variation of the UV laser is not possible. Directly modulating the RF to drive the double-pass AOM before the reference cavity allows to tune the 852 nm light with a precision of 20 kHz, much smaller than the stabilized laser linewidth. Scan ranges up to 400 MHz can be achieved by frequency modulation of the AOM. In total, illuminating the ion by the laser near 213 nm for a short time between a few µs up to 1 ms probes the $3D_{5/2} \rightarrow 5P_{3/2}$ transition. Scanning the fundamental laser and correcting for energy shifts like Zeeman shifts or AOM frequencies, the resonant transition frequency is found to be [And21]:

$$\Delta E(3D_{5/2} \rightarrow 5P_{3/2}) = 1\,817\,081.257(30)\,\text{GHz} \quad .$$

The state measurement is indirect by observing the population decay to the ground state. Figure 4.4 shows the measured depopulation of $3D_{5/2}$ plotted as a function of detuning from the atomic resonance $\Delta_{213}$. Once the deep UV laser is resonant with the atomic transition, ions are excited to the intermediate state $5P_{3/2}$ and decay to the electronic ground state. A fluorescence measurement with light near 397 nm shows a bright ion and indicates successful excitation, whereas a ion residing in the dark $3D_{5/2}$ state does not interact with the detection laser. The full width at half maximum of the observed atomic resonance $\Gamma_{5P} = 2\pi \cdot 8.2(2)$ MHz is dominated by the natural lifetime of the electronic state and an additional Doppler broadening due to absorption of a high energy photon. The influence of the laser linewidth of $\approx 1$ MHz is negligible compared to the other broadening mechanisms.

## Transition Frequencies and Excitation into Rydberg States

Including the second deep UV laser into the excitation scheme, the state population can be transferred into the Rydberg state for a direct excitation, or coupling the respective energy levels to avoid an excitation by utilizing the QI method. Both schemes require accurate knowledge of the transition frequencies, which have not been measured for high-lying Rydberg states in $^{40}\mathrm{Ca}^{+}$. The article [And21] presents Rydberg $n\mathrm{S}_{1/2}$- and $n\mathrm{D}_{5/2}$-series excitation of a single trapped Calcium ion for principal quantum numbers $n \in [38, 65]$. The Rydberg-series spectroscopy was performed using a high accuracy wavemeter (High Finesse, WS8-2), which allowed for determination of the second ionization energy in Calcium with 60-fold improved accuracy compared to the accepted value. Also, an experimental realization of high-lying Rydberg states challenges theory to provide more accurate descriptions of quantum defect values as well as calculations of static and tensor polarizabilities [Paw20].

The Rydberg ion exhibits many interesting properties, such as sensitivity to external fields, state-dependent lifetimes or strong interactions with neighboring Rydberg ions. One property of highly excited ions is the susceptibility to blackbody induced ionization events, where the electronic state population is cascaded into the continuum by the strong interactions between different Rydberg Stark states [Mü08, Ovs11]. Unfortunately, a doubly ionized Calcium is still trapped in the oscillating quadrupole field but not accessible by the used laser sources. The doubly ionized Calcium has to be removed from the trap by releasing the confining potential and subsequent reloading of another ion to restart the experimental sequences. For measurements of transition frequencies into Rydberg states it is convenient to circumvent double ionization events without losing the sensitivity for Rydberg properties that shift the energy level of the highly excited state. The QI method employs a coupling of electronic levels by resonant laser fields, such that transition frequencies are shifted and a difference in excitation probabilities can be observed. Here, the first excitation laser (probe) near 213 nm is resonantly exciting the intermediate $5\mathrm{P}_{3/2}$ state and illuminates the ion with optical intensities close to saturation. Detecting the state of the ion without the second deep UV laser (coupling) or with the second laser far off the resonance, the final state population is dominated by decay via the intermediate state and a bright ion can be observed. Tuning the frequency of the coupling beam near 286 nm onto the atomic resonance, the probability to detect a bright ion decreases and the ion remains in the initialized $3\mathrm{D}_{5/2}$ state. The resonant coupling of the second laser field to the electronic states leads to an energy shift on the $5\mathrm{P}_{3/2}$ state and an effective detuning for the probe laser. Coupling strength and the respective transition linewidth is dependent

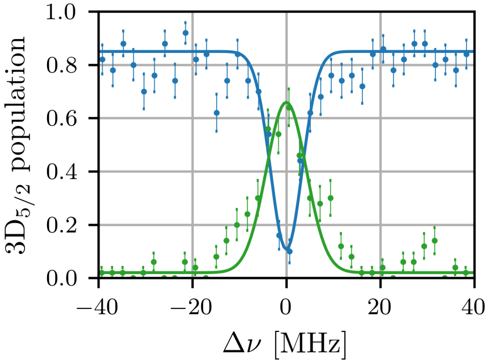

**Figure 4.5:** $55S_{1/2}$ excitation spectrum probed by residual population in the $3D_{5/2}$ state as a function of two-photon detuning $\Delta\nu$ for direct excitation (blue) and the QI method (green). Error bars depict the quantum projection noise and solid lines are Gaussian fits to the data to extract transition frequency and linewidth, where the full width at half maximum is 7.9(7) MHz for the direct excitation spectrum and 10(9) MHz for the QI spectrum.

on both laser intensities, where high coupling power increases the energy shift and generates a broad resonance. Contrary, high probe power saturates the first transition and leads to a decreased visibility of the energy shift, but allows for a more refined determination of transition frequency as the effective linewidth decreases [Fle05].

Another way of measuring transition frequencies is the direct excitation of the ion's electronic state, such that the two-photon resonance condition is fulfilled. To avoid population transfer to the ground state via the intermediate $5P_{3/2}$ state, the laser near 213 nm is detuned from the atomic resonance, typically between $\Delta_{213} = 50\,\text{MHz} - 200\,\text{MHz}$. Due to finite widths of the transition and the laser source, the ion is still off-resonantly excited with probabilities of a few percent. Varying the frequency of the laser near 286 nm and fulfilling the two-photon resonance condition, the ion is excited to the Rydberg state and decays into the ground state on timescales of few µs. Afterward, observing the ion's fluorescence indicates a successful Rydberg excitation. Figure 4.5 shows the two-photon resonance spectra of the $55S_{1/2}$ Rydberg state for different two-photon detunings of a direct Rydberg excitation (blue) compared to a the QI method (green). The linewidth of the excitation spectrum is fundamentally limited by the natural linewidth of the Rydberg state given by the inverse lifetime, but Doppler broadening, laser linewidth, as well as effects due to the high polarizability dominate the observed lineshapes. These effects, which shift the energy level of the probed Rydberg state, are observed even if the QI method is used.

## Modeling Transition Lineshapes for Rydberg Excitation

The spectral lineshape of an optical transition is typically given by a Lorentzian function with resonance frequency $\nu_0$. Decoherence mechanisms such as spontaneous decay or finite laser linewidths add up to define the width of this Lorentzian. Here, the Rydberg state decays within $\tau_\mathrm{R} \approx 5\,\mathrm{\mu s}$ [Saf11] to yield a natural linewidth of $\Gamma_\mathrm{R} = {}^1\!/\!_{\tau_\mathrm{R}} \approx 20\,\mathrm{kHz}$, which is orders of magnitude smaller compared to experimental limitations as laser linewidth or Doppler broadening. As the linewidth of the deep UV lasers is not reduced by the frequency stabilization and an individual linewidth below $\Gamma_\mathrm{UV} = 1\,\mathrm{MHz}$ is specified, a combined linewidth of $\Gamma_\mathrm{Laser} < 2\,\mathrm{MHz}$ is assumed for the uncorrelated laser sources. Future stabilization of the fundamental wavelengths to high finesse cavities ($\mathcal{F} > 100\,000$) will reduce the Lorentzian linewidth, ultimately limited by the natural lifetime of the Rydberg states. The Doppler broadening is effectively reduced by using counter-propagating laser beams and results in

$$\sigma_\mathrm{Doppler} = \frac{\nu_0}{c}\sqrt{\frac{8k_\mathrm{B}T\ln 2}{M}} \approx 1\,\mathrm{MHz} \quad , \tag{4.41}$$

with the speed of light $c$, the Boltzmann constant $k_\mathrm{B}$ and the ion temperature $T$, which is assumed to be at the Doppler limit of $T = 0.55$ mK. Analogously, co-propagating deep UV lasers would lead to a Doppler broadening of $\sigma_\mathrm{Doppler} \approx 6.5\,\mathrm{MHz}$. The broadening due to ion temperature is an incoherent effect and does not add to the Lorentzian width of the lineshape, but is more accurately described as Gaussian broadening. For an ion, which is not cooled to the motional ground state the lineshape is modeled by a convolved Lorentzian and Gaussian distribution, namely a Voigt profile [Wer74].

The centroid frequency of this Voigt profile is determined by the energy difference between initial and final state, where energy shifts have to be considered. Apart from the Zeeman effect, which affects both the $3\mathrm{D}_{5/2}$ state as well as the highly excited state, the polarizability $\mathcal{P}$ of Rydberg states shifts the energy due to the surrounding trapping field. The positioning of a Rydberg ion within a non-zero electric field leads to a quadratic Stark shift as given in equation 2.20, which is minimized by compensation of micromotion. For a residual electric field $E^{(\mathrm{rad})}_\mathrm{RMS} = 24(1)\ {}^\mathrm{V}\!/\!_\mathrm{m}$ the $55\mathrm{S}_{1/2}$ state experiences an energy shift of $\Delta E_\mathrm{Stark} = -1.24(10)\,\mathrm{MHz}$ by the shift between static and quadrupole field nulls. Moreover, the Rydberg state itself modifies the effective confinement of the ion and the ion's secular frequencies (see equation 2.28). This leads to two effects: On the one hand the ion's equilibrium position within the harmonic

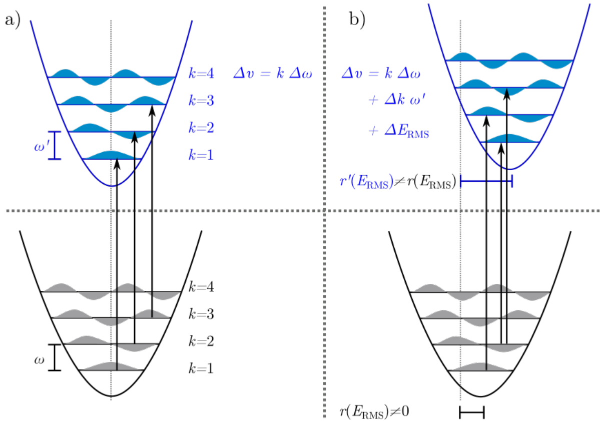

**Figure 4.6:** Schematic view of transition frequency shifts due to a state-dependent trap frequency $(\omega, \omega')$ and huge polarizability of Rydberg states (in blue) compared to electronically low-lying states (gray). a) And b) show possible motion assisted Rydberg transitions for zero and finite residual electric fields, respectively. The transition frequency shift $\Delta\nu$ depends on the overlap of motional states in the effective harmonic potentials and the quadratic Stark shift, as given by the equilibrium position $r(E_{\mathrm{RMS}})$ and $r(E_{\mathrm{RMS}})'$.

potential changes for non-perfect residual electric field compensation, again leading to an increased quadratic Stark shift and driving of phonon number changing transitions [Hig19]. On the other hand, even if perfectly compensated, the transition frequency changes for each individual occupation of the motional states, as the state-dependent trap frequency adds to the total energy in the system. A schematic view of Rydberg excitation in the presence of occupied motional modes in an 1D harmonic oscillator is shown in figure 4.6a) and b) for the case of perfect and imperfect residual field compensation, respectively. For the discussion below it is assumed, that the residual electric field is negligible for all lineshape modifications and phonon number changing transitions do not occur.

As the trap field gradient is much larger along the radial directions compared to the axial direction, the radial motion of the ion is dominating the energy shift. After Doppler cooling, the occupation of vibrational modes in the harmonic oscillator follows a thermal distribution, but more elaborate phonon statistics will be discussed in section 5.1. Close to the Doppler limit, the residual ion temperature can be described in terms of phonons along the three trap axes, where each motion is decoupled from each other. The occupation of the ion's motional states is given by the Bose-Einstein statistics and the probability $p^{(\mathrm{th})}(k)$ to find the ion within a certain phonon state $k$ in mode $\omega$ is described as:

$$p^{(\mathrm{th})}(k) = \left(1 - \exp\left(-\frac{\hbar\omega}{k_{\mathrm{B}}T}\right)\right) \exp\left(-\frac{k\hbar\omega}{k_{\mathrm{B}}T}\right) \quad . \tag{4.42}$$

That means, even for high temperatures the ion is found in the zero phonon state with maximum probability, but large phonon numbers $k \gg 10$ are non-negligible. Also, a variation of the trap frequency changes the slope of the phonon distribution, such that for higher secular frequencies, the lower phonon numbers become more probable. Ion temperatures close to zero lead to a phonon distribution, which approaches the motional ground state and, therefore, it is convenient to relate the temperature and trap frequency by the average phonon number $\bar{k}$ with

$$\bar{k} = \frac{1}{\exp\left(\frac{\hbar\omega}{k_{\mathrm{B}}T}\right) - 1} \quad . \tag{4.43}$$

For any thermal state, the average phonon number $\bar{k} > 0$ can be used to describe the deviation from the motional ground state. A single trapped ion confined by frequencies $\{\omega_x, \omega_y, \omega_z\} = 2\pi \cdot \{0.95, 1.27, 0.55\}$ MHz and cooled to the Doppler limit has average phonon numbers $\{\bar{k}_x, \bar{k}_y, \bar{k}_z\} = \{11.6, 8.6, 20.2\}$. To reach occupations $\bar{k} \to 0$ at these trap frequencies, additional cooling methods need to be applied, before the oscillation of the ion can be approximated by the motional ground state. This would simplify calculation on the sub-space of vibrational levels and lead to more precise measurements of transition frequencies.

Finally, the depopulation lineshape of the $3\mathrm{D}_{5/2}$ state by Rydberg excitation can be modeled including broadening mechanisms and energy shifts. The Voigt profile $\mathcal{L}(\nu, \Gamma, \sigma)$ consists of a Lorentzian distribution determined by laser linewidth $\Gamma_{\mathrm{Laser}}$ and natural linewidth of the Rydberg state $\Gamma_{\mathrm{R}}$, while Doppler broadening $\sigma_{\mathrm{Doppler}}$ relates to the Gaussian width. The centroid frequency is shifted by $\Delta E_{\mathrm{Stark}}$ and $\Delta E_{\mathrm{Zeeman}}$ for residual electric and magnetic fields, respectively. Thermal phonon distributions along the radial direction shift the centroid frequency too, since the state-dependent trap frequencies lead to an energy shift of $\Delta\omega$ for each phonon. Therefore, individually shifted resonance lineshapes for phonon states $k$, weighted by the probability $p^{(\mathrm{th})}(k)$ are summed up to generate the transition lineshape model:

$$\mathcal{L}_{\mathrm{R}}(\nu) = \sum_{k_x, k_y = 0}^{\infty} p^{(\mathrm{th})}(k_x) p^{(\mathrm{th})}(k_y) \mathcal{L}\left(\nu - \Delta\nu, \Gamma_{\mathrm{R}} + \Gamma_{\mathrm{Laser}}, \sigma_{\mathrm{Doppler}}\right) \tag{4.44}$$

with

$$\Delta\nu = \Delta E_{\mathrm{Stark}} + \Delta E_{\mathrm{Zeeman}} + k_x \Delta\omega_x + k_y \Delta\omega_y \quad . \tag{4.45}$$

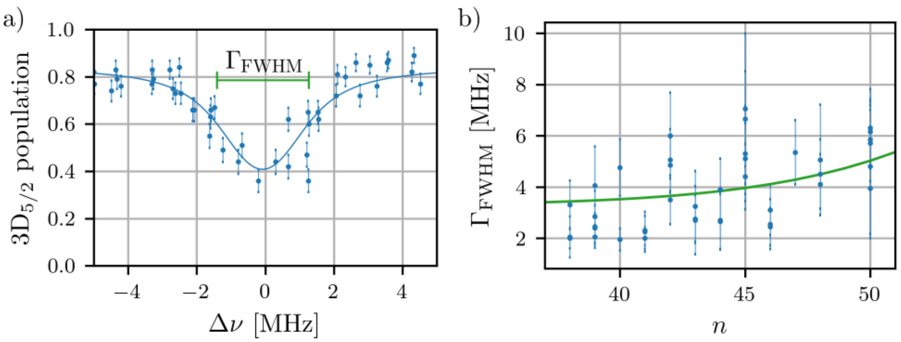

**Figure 4.7:** a) Depopulation of the $3D_{5/2}$ state for Rydberg excitation into $39S_{1/2}$, where the solid line shows a fit of the lineshape model with the ion temperature as a free parameter. b) Modeled excitation linewidth $\Gamma_{\text{FWHM}}$ (green) as a function of principal quantum number and comparison to experimental data (blue).

Especially, phonon-dependent shifts due to the huge polarizability have a major impact on the lineshape, leading to asymmetries for ions at finite temperature. Additionally to the presented shifts, the Rydberg excitation is modulated by the oscillating trapping fields for larger ion temperatures and residual electric fields, resulting in sidebands at frequencies $\Delta\nu = \pm\Omega_{\text{RF}}$. Although these sidebands have been previously observed for Rydberg excitation of trapped ions [Mok19], they are not relevant for this thesis and will not be further discussed.

Equation 4.44 allows for the prediction of a transition lineshape for Rydberg excitation, if phonon distribution and polarizability are specified. As long as the electric field is accurately compensated and constant during Rydberg excitation, the quadratic Stark shift is constant and can be omitted for measurements of the relative transition frequency. The same holds true for the Zeeman shift. After Doppler cooling, the mean phonon number along radial directions is dependent on the trap frequencies given by the field gradients of the Paul trap. Similarly, the frequency difference for Rydberg states is dependent on the trap field gradients and the polarizability. Although theoretically investigated by Kratzer-Fues model potential calculations [Kam14] the polarizability is not yet experimentally verified for highly exited Calcium ions. Assuming a fixed ion temperature one expects an increasing excitation linewidth as a function of principal quantum number due to larger polarizabilities for high-lying Rydberg states as shown in figure 4.7. Here, the transition lineshape to the $39S_{1/2}$ state is shown and fitted by the lineshape model to yield a full width at half maximum $\Gamma_{\text{FWHM}} = 3.3(9)\,\text{MHz}$. The uncertainty in linewidth is dominated by the temperature estimation of the cooled ion. An imperfect initialization leads to an offset in the $3D_{5/2}$ population and a loss in contrast for detection of Rydberg excitation. Nevertheless, the transition to the Rydberg state is resolved and a fit with the lineshape model allows for an extraction of Rydberg state properties related to the polarizability and excitation strength (see below). For a given ion temperature, the polarizability of high-lying Rydberg states manifests itself in a shift of phonon-conserving transition frequencies and an asymmetric broadening of the transition line. Comparing the transition linewidth by the lineshape model (green) with no free parameter to the extracted width of individual Rydberg transitions (blue) indicates a good understanding of the frequency shifts, as presented in figure 4.7b). In total, a mean ion temperature of 3(2) mK is extracted from individual measurements, which is larger than the expected temperature after Doppler cooling for a two-level system. Additional deviations from the Doppler limit can be explained by the low vibrational frequencies, which are sensitive to electrical noise on the trap voltages or insufficient control of the laser cooling due to field inhomogeneities inside the trap. As shown in section 4.3 an increase in vibrational frequencies by a factor of two allows to drastically decrease the ion temperature and observe motion close to the vibrational ground state. Also, the ion temperature might be overestimated for the presented measurements, as additional broadening of the excitation spectrum by residual electric fields or phonon changing transitions are not included in the lineshape model.

## Principal Quantum Number Scaling of the Depopulation Rate

When exciting trapped ions to Rydberg states and investigating ion-ion interaction or using state-dependent forces for sensing applications, a narrow transition lineshape is preferred as the required laser intensities for state transfer are related to the total area of the lineshape. The probability to excite Rydberg states is distributed over a range of two-photon detunings given by the ion temperature, trap frequencies and the polarizability. Larger excitation strengths at a fixed detuning are achieved by increasing the total laser power that drives the optical transition and the excitation strength of the Rydberg state scales by the two-photon Rabi frequency $\Omega_\mathrm{R}$:

$$\Omega_\mathrm{R} = \frac{\Omega_{213}\Omega_{286}}{2\Delta_{213}} \quad , \tag{4.46}$$

where $\Omega_{213}$ and $\Omega_{286}$ are the Rabi frequencies of the lasers near 213 nm and near 286 nm, respectively. Moreover, the Rabi frequency of each individual Rydberg excitation laser is related to the transition dipole moment $d$ and the electric field of

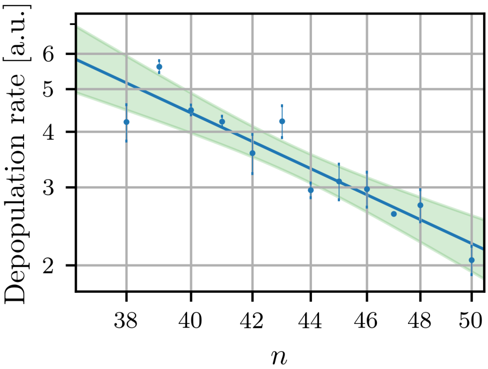

**Figure 4.8:** Depopulation rate as a function of principal quantum number $n$. Here, the total lineshape integral for individual Rydberg excitations is rescaled by the used laser intensities and intermediate state detunings, and averaged for each $n$. The solid line shows a power law fit to the data, yielding a scaling of $n^{3.0(4)}$ with confidence band highlighted in green.

the laser $E$ with $\Omega = dE \propto d\sqrt{P}$, where $P$ is the laser power. As the measurement of transition lineshapes is a projective measurement on the low-lying electronic states $3D_{5/2}$ and $4S_{1/2}$, a successful Rydberg excitation is observed by depopulating the initialized $3D_{5/2}$ state. Relating the total lineshape integral to the individually used laser power allows to extract a state-dependent depopulation rate. In figure 4.8 this state-dependent depopulation rate is given in arbitrary units, as the exact values of transition dipole moments between electronically low-lying and high-lying states are not known. In general, the transition dipole moments for excitation into Rydberg states scale with principal quantum number $d \propto n^{-3/2}$ such that the excitation strength decreases for high-lying Rydberg states. Also, the polarizability of Rydberg states combined with the Doppler effect broadens the transition lineshape for ions at finite temperature. Overall, the depopulation rate fits a power law $n^{-3.0(4)}$, which disagrees with the expected scaling originating from the transition dipole moment. In the following, numerical simulations are utilized to interpret the obtained results.

Within the framework of multilevel Maxwell-Bloch equations [Mar11] the excitation scheme is simulated with no free parameters but the excitation strength $\Omega_R$ to Rydberg states. Coupling of the electronic ground state and the metastable $3D_{5/2}$ state is achieved by lasers near 213 nm and near 286 nm, exciting the $5P_{3/2}$ and $n S_{1/2}$ state, respectively. The lineshape model is used as input for the excitation linewidth and broadening due to finite laser linewidths is included. Similarly, the state decay to the ground state with a Rydberg state lifetime scaling with $n^3$ is considered [Glu13]. Within the calculations, the two-photon detuning is varied around the resonance condition and allows for the calculation of a lineshape integral. Here, the maximum excitation rate out of the initial $3D_{5/2}$ state was chosen to be 40% by adjusting $\Omega_R$ and adapting the initial simulation parameters to match the experimental results. Independently varying the principal quantum number and evaluating the corresponding lineshape integral allows for an extraction of state-dependent depopulation rate $\propto n^{-3}$, which agrees with the experimentally observed one. Furthermore, the simulations allow to predict population dynamics for various ion temperatures, laser linewidths and Rydberg state lifetimes. Experiments investigating Rydberg-Rydberg interactions require coherent control of the Rydberg state population by excitation and de-excitation using short laser pulses. Apart from a narrow laser linewidth, the population transfer between states can be enhanced by applying time-dependent amplitude modulation on the excitation lasers [Ber19]. Nevertheless, the observation of coherent population dynamics is not limited by laser powers in the presented setup, but the discussed broadening mechanisms by laser linewidth and ion temperature.

## 4.3 Towards Fast Rydberg Excitation

The Rydberg excitation spectra of the previous section were recorded with laser pulses on timescales of 1 ms and only depopulation of the initial $3D_{5/2}$ is observed. As a prerequisite to study many interactions between Rydberg ions, coherent excitation and de-excitation of the Rydberg state becomes necessary. Limited by the Rydberg state lifetime, these laser pulses need to be as short as 1 µs and require high intensities of both deep UV lasers. Similarly, a reduction of the transition linewidth effectively enhances the excitation rates for resonant laser pulses. The thermal excitation of the ion is discussed as one of the reasons for a large linewidth. Using sub-Doppler cooling methods, the ion temperature along different directions can be addressed and controlled to a high degree, thereby allowing to manipulate the phonon distributions prior to Rydberg excitation.

### Cooling the Ion to the Motional Ground State

There are various ways to cool the ion below the Doppler limit [Esc03] and to reduce the average phonon number of the thermal phonon distribution along each of the uncoupled trap axes. For temperatures close to zero, the oscillation of the ion is well approximated by the motional ground state. Here, only the lowest energy level of the harmonic oscillator is occupied and phonon-dependent variation of laser-ion interaction can be neglected. If there are residual phonons, transitions between electronic states are altered by a phonon-dependent Rabi frequency as given in equation 2.33 and acquire sidebands at detuning of the trap frequencies $\pm\omega$. For a $^{40}\mathrm{Ca}^+$ ion, the quadrupole transition near 729 nm can be excited at its motional sidebands to further decrease the ion temperature. Intuitively, exciting the ion with an energy difference corresponding to the vibrational frequency $\pm\omega$ results in raising or lowering its external motion by a single quanta. Continuously driving the red sideband and thereby lowering the motional occupation of this vibration can lead to an asymptotic cooling to the motional ground state. Experimentally, the ion is illuminated by single pulses on the red motional sidebands of the $4\mathrm{S}_{1/2,-1/2} \rightarrow 3\mathrm{D}_{5/2,-5/2}$ transition followed by a quench with infrared light near 854 nm, similar to state initialization. As the quadrupole laser needs a projection onto the vibrational mode, either radial or axial sideband cooling can be applied in the presented setup. The dominant contribution for the observed broadening of Rydberg excitation lineshapes are radial phonons, such that typically only radial sideband cooling is applied.

To reduce the complexity of sideband cooling, the vibrational frequencies should be as high as possible, as the initial average phonon numbers decrease and less cooling cycles become necessary. Also, counteracting effects on the ion temperature, e.g. the heating rate, are frequency dependent and expected to be less crucial for higher frequency modes [Sed18]. Consequently, the trap field gradients are increased to yield vibrational frequencies close to $\{\omega_x, \omega_y, \omega_z\} = 2\pi \cdot \{1.9, 2.2, 1.0\}$ MHz. At the same time, the ion has to stay trapped within the harmonic potential, such that $\omega_{x,y} \ll \Omega_{\mathrm{RF}}$. For larger radial trap frequencies, the ion temperature after Doppler cooling increases, which might hint to instabilities in the ion confinement or the drive electronics for high RF amplitudes. At the given frequencies the sideband cooling is optimized by probing the excitation strength of red ($\Delta\nu = -\omega$) and blue sidebands ($\Delta\nu = +\omega$) on the quadrupole transition (c.f. figure 2.4). The Rabi frequency scales as $\Omega_{\mathrm{red}} \propto \sqrt{k}$ and $\Omega_{\mathrm{blue}} \propto \sqrt{k+1}$ for red and blue sidebands, respectively, and allows to extract the average phonon number. After tens of consecutive pulses (with slightly increasing pulse times) on the corresponding red sidebands, average phonon numbers below $\bar{k}_{y,z} < 1$ are observed along directions $y$ and $z$. This shows successful sideband cooling with final occupation close to the motional ground state. However, direction $x$ showed only little effect by sideband cooling and is usually not cooled below average phonon numbers of $\bar{k}_x < 5$. Note, probing the temperature along $x$ also yields higher average phonon numbers compared to direction $y$ after Doppler cooling, although the frequencies are similar and the projection onto the cooling laser is geometrically the same. An imperfect cooling along one radial direction is most likely due to electrical noise on the electrode structure or imperfections during trap fabrication. Both statements are supported by findings of other measurements, e.g. the grounded DC electrode or the off-centered position for axial micromotion compensation, which is not fully understood. Nevertheless, sideband cooling along direction $x$ is optimized by adding an overall offset voltage to the DC segments, which leads to larger vibrational frequencies $\omega_x$ while reducing $\omega_y$. To mitigate off-resonant excitation for short laser pulses, a degeneracy of vibrational modes needs to be avoided. For typical pulse lengths of the quadrupole laser between $5 - 15\,\mu\mathrm{s}$ the desired frequency splitting of the vibrational modes should be $|\Delta\omega| > 2\pi \cdot 200\,\mathrm{kHz}$. Best overall performance of sideband cooling was found for vibrational frequencies $\omega_x = 2\pi \cdot 2.2\,\mathrm{MHz} > \omega_y = 2\pi \cdot 1.9\,\mathrm{MHz}$ with both $\bar{k}_{x,y} < 1$ at an offset voltage of $38\,\mathrm{V}$, which is close to the voltage limit of BERTHA.

In total, sideband cooling with more than 100 pulses could prepare a single ion close to the motional ground state along both radial directions, see section 5.1. However for successive probe pulses and long sequences including Rydberg excitation it is necessary that the ion stays cold. Experiments performing high fidelity gates for quantum computing [Kau17a] as well as the proposal to use motional excitation of Rydberg ions for entanglement, presented in section 6.1, rely on the ion being in the motional ground state. To quantify limits for experimental duration and final average phonon numbers, the heating of the ion's motion due to electrical noise, collisions of the ion with background gas, etc., is measured. Varying the time between sideband cooling and probing the phonon number, heating rates $\dot{\bar{k}}_{y,z} \approx 20\ {}^{\mathrm{ph}}/_{\mathrm{s}}$ are obtained along direction $y$ and $z$, which are comparable to similar fabricated traps [Wol19]. Contrary, the heating rate $\dot{\bar{k}}_x \approx 2\ {}^{\mathrm{ph}}/_{\mathrm{ms}}$ is two orders of magnitude larger compared to the other two trap directions. For sequences longer than a few 100 µs, the ion's motion gets excited and phonon-dependent variations of Rabi frequency and transition lineshapes need to be considered. Large motional occupation along $x$ is also a possible explanation of the observed Rydberg excitation linewidths in figure 4.7, which resulted in an ion temperature larger than the expected Doppler limit. As the order of magnitude for the heating rate was found independent on trap parameters and no external reduction of noise sources improved $\dot{\bar{k}}_x$, an exchange of the trap seems to be inevitable to reach better and more reproducible motional ground state cooling.

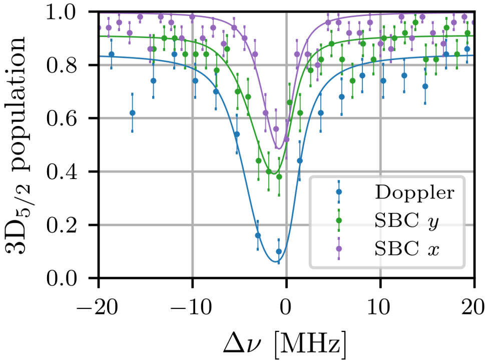

**Figure 4.9:** Depopulation of the $3D_{5/2}$ state for Rydberg excitation into $55S_{1/2}$ as a function of two-photon detuning $\Delta\nu$. Different initial ion temperatures are probed by Doppler cooling (blue), additional sideband cooling (SBC) on $\omega_y$ (green) and on $\omega_x$ (purple). Lines are fits with the lineshape model to extract temperature-dependent linewidths of the Rydberg transition.

## Rydberg Excitation of a Cold Ion

Heterogeneous heating along the two radial trap directions leads to difficulties in predicting the Rydberg excitation lineshape and limit the experimental duration before the ion needs to be cooled again. The state-dependent frequency shift relies on the thermal phonon distributions within modes with secular frequency $\omega$. For ions far away from the motional ground state, the lineshape model predicts large line broadening as the principal quantum number increases. Applying sideband cooling on both radial modes, the linewidth modulation is independent of the Rydberg state polarizability, but limited by the combined deep UV laser linewidth of 2 MHz and a residual Doppler broadening for motion along the trap axis of 1 MHz. Figure 4.9 shows excitation spectra of the $55S_{1/2}$ state with and without sideband cooling along both radial modes, respectively. The presented transition spectra are fitted with the lineshape model to extract a temperature-dependent linewidth for a Doppler cooled (blue) ion, with sideband cooling along $y$ (green) and along $x$ (purple). The full width at half maximum is effectively reduced by implementing sideband cooling, but, as expected, motion along $x$ is the dominant source of linewidth broadening. Compared to the Doppler cooled excitation linewidth of $\Gamma_{\mathrm{FWHM}} = 6.6(8)$ MHz, an additional sideband cooling of mode $\omega_y$ results in the width $\Gamma_{\mathrm{FWHM}} = 5.5(7)$ MHz. The minimal achieved linewidth of $\Gamma_{\mathrm{FWHM}} = 3.9(10)$ MHz by cooling the mode along $x$ agrees with the limit for laser linewidth and Doppler broadening. Again, the measurements indicate, that the ion

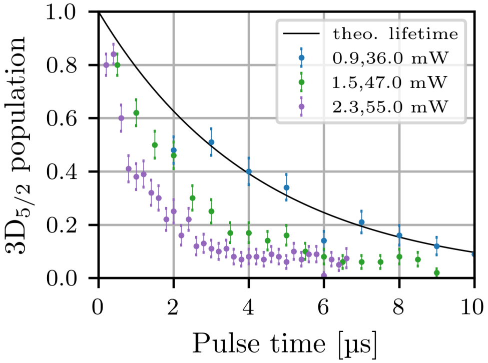

**Figure 4.10:** Depopulation of the $3D_{5/2}$ state for Rydberg excitation into $45S_{1/2}$ as a function of laser interaction time for different laser powers given in the legend as $P_{213}, P_{286}$. The laser sources deliver sufficient power to drive Rydberg transitions much shorter than the theoretical state lifetime (black), such that coherent population transfer is in reach by future reduction of the excitation linewidth.

is not homogeneously cooled by the laser near 397 nm, but has a predominantly hot mode only being suppressed by additional cooling efforts. Note, sideband cooling also affects the efficiency of state transfer between low-lying electronic states and improves the initialization into $3D_{5/2}$, thereby reducing the false positives of detecting bright ions from 15(5)% to 5(5)%.

## Excitation within the Rydberg State Lifetime

The excitation strength of the resonant two-photon process is given by equation 4.46 and depends on the two individual Rabi frequencies $\Omega_{213}$ and $\Omega_{286}$, as well as the detuning $\Delta_{213}$ from the intermediate state. The natural linewidth $\Gamma_{5P}$ due to the state's lifetime leads to unwanted scattering and loss of contrast if the detuning is too small. Typically, the latter is set by minimizing the population transfer to the $5P_{3/2}$ state for a given laser power and interaction time, such that maximally 5% off-resonant scattering is observable. Increasing the optical intensities of both UV lasers allows to reduce the laser interaction time for similar excitation strengths and off-resonant scattering. This is possible by either decreasing the beam waists at the ion or increasing the laser power. Final spot sizes below 10 µm are sufficient to excite the $45S_{1/2}$ Rydberg state within just a few µs, as presented in figure 4.10 for different combinations of laser power. Here, the detuning was chosen $\Delta_{213} \approx 60\,\text{MHz}$ and for each set of depicted laser power, population transfer into the intermediate $5P_{3/2}$ state is negligible. Since the estimation of Rabi frequency is difficult without knowledge of exact transition dipole moments or further measurements, the optical laser power $P$ in front of the vacuum vessel is given, which scales as $\Omega \propto \sqrt{P}$. Three sets of laser power, $\{P_{213}, P_{286}\} = \{0.9, 36\}, \{1.5, 47\}$ and $\{2.3, 55\}$ mW are depicted in blue, green and purple, respectively. A total laser power of $\{15, 100\}$ mW is available. The initial state population is fully excited to the Rydberg state within less than 10 µs, which is shorter than the expected lifetime $\tau_{45\mathrm{S}} = 4.3$ µs [Glu13]. Spontaneous decay from the Rydberg state is indicated by the black line as a limit for visibility of coherent population dynamics. Any excitation below this line may undergo Rabi oscillations if decoherence is suppressed. However, even the highest presented laser power does not retrieve the initial dark state of the ion within the lifetime of the Rydberg state. Further reduction of lineshape broadening by additional cooling of the axial motion and minimizing laser linewidth might lead to observation of coherent state dynamics. Already being able to drive Rydberg transitions on µs timescales - even though the linewidth is larger than 2 MHz - paves the way for observation of Rydberg-Rydberg interactions between multiple ions.

# 5

# It's Exciting I: Motional Excitation for Quantum Sensing

Highly excited ions in Rydberg states are trapped within the oscillating potential of the Paul trap even though they interact strongly with environmental electric fields. Due to the large polarizability $\mathcal{P} \propto n^7$ the quadratic Stark effect from time averaged oscillating and residual electric fields lead to a shift of energy levels and a state-dependent confinement for ions in Rydberg states. Similarly, in systems of neutral Rydberg atoms, the electric field sensitivity is employed to build accurate sensors of static and oscillating fields [Fan15]. Combining ions in a shuttling based trap architecture with electronically highly excited states allows to transfer electric field sensing into the ion trap system. Within the laboratory, external electric fields can be compensated , such that no Stark effect is present, but intrinsic energy shifts due to the state-dependent trap frequency can be further characterized. Any occupation of motional modes alters the excitation frequency of trapped ions into a high-lying Rydberg state and manifests itself in a transition lineshape depending on the phonon distribution. Specifically, designing this distribution of a trapped ion and studying the transition lineshape of various Rydberg states allows to extract the polarizability, necessary to investigate interactions between Rydberg ions and external electric fields.

The following section provides insights into various phonon distributions for trapped ion systems with the focus on preparation and characterization of coherent states of motion. Driving the harmonic oscillator by an external field resonant to the secular frequency allows for generation of large atomic wave packets with high average phonon numbers, that result in substantial Rydberg transition frequency shifts. Excitation lineshapes of ions in coherent motional states are discussed and analyzed for different principal quantum numbers and coherent state sizes. Finally, the polarizability of the corresponding Rydberg state is extracted from individual fits of the lineshape model to the data and compared with theoretical predictions. The presented experiments are further discussed in the masters thesis of Marie Niederländer [Nie21].

## 5.1 Coherent States and Rydberg Excitation of Strongly Oscillating Ions

A direct measurement of state-dependent trap frequencies is difficult due to the short lifetimes of Rydberg states, but energy conservation and large polarizability lead to changes in transition frequency dependent on the phonon number in both radial modes. The phonon statistics of a trapped ion can be engineered in various ways and different phonon distributions result in distinguishable transition lineshapes for a given Rydberg state. After Doppler cooling the ion's motion is in a thermal state with average phonon number $\bar{k}$ dependent on the vibrational frequency and ion temperature (c.f. equation 4.43). By sideband cooling on the $4S_{1/2,-1/2} \rightarrow 3D_{5/2,-5/2}$ transition the average phonon numbers can be reduced below $\bar{k}_{x,y} < 1$ along the radial directions. Thereby, the probability to find the ion in the zero-phonon state is strongly enhanced compared to only Doppler cooling.

Once the ion's oscillation is well described by the motional ground state, it is possible to engineer phonon distributions by applying laser pulses or electrical fields. One example is a Fock state, which is a pure quantum states with exactly one vibrational level $k$ occupied. A Fock state can be successively created from the motional ground state by applying the creation operator $k$ times: $|k\rangle = (a^{\dagger})^k |0\rangle_k$. Generally, the Fock states form an orthonormal basis and superpositions of these states can be used to describe any phonon distribution. Exciting the ion to a specific Fock state and probing the transition to Rydberg states does not lead to a broadened lineshape, but rather shifts the transition frequency by $k \cdot \Delta\omega$, where $\Delta\omega$ is the trap frequency difference between electronically low- and high-lying state. In practice, Fock states of motion can be created by applying laser pulses on the blue sideband of an initially ground state cooled ion and repeating the process until the desired phonon number is reached. This series of laser pulses acquires a probabilistic error for each successive blue sideband transition and the coupling strength for individual transitions has to be adjusted as the phonon number modifies the Rabi frequency. By detecting the dark ion after each individual laser pulse, which confirms successful excitation of the next Fock state, and discarding measurements with bright ion detection, the desired Fock state can be prepared with high accuracy. This leads to systematic shift of Rydberg excitation frequency [Hig19]. However, imperfect motional initialization and post-selection of the data leads to many discarded measurements, especially when aiming for high motional occupation. Therefore, a more reliable method to observe large phonon numbers and corresponding large shifts of transition frequencies is desired.

Another way of generating high phonon numbers is utilizing coherent states of motion $|\alpha\rangle$, which are given in the Fock basis as:

$$|\alpha\rangle = \exp\left(-\frac{1}{2}|\alpha|^2\right)\sum_{k=0}^{\infty}\frac{\alpha^k}{\sqrt{k!}}|k\rangle \quad . \tag{5.47}$$

This representation follows from $|\alpha\rangle = D(\alpha)|0\rangle$ with the displacement operator acting on the zero phonon state. The displacement of the ion out of the trap center by an electric field and the generation of coherent motional excitation will be derived in section 6.1, while here the properties of coherent states are only discussed qualitatively. The complex number $\alpha = |\alpha| e^{i\phi}$ describes the amount of displacement in phase space and is defined similarly to the electromagnetic field in classical optics with amplitude $|\alpha|$ and phase $\phi$. Thereby, the coherent states can be seen as wave-like states of the harmonic oscillator, e.g. the motion of the trapped ion. Note, the coherent state is defined as an eigenstate of the annihilation operator with $a|\alpha\rangle = \alpha|\alpha\rangle$, such that the phonon distribution of a coherent state needs to be Poissonian. Hence, all detections of the coherent motional state of a trapped ion are statically independent of each other and the probability of detecting $k$ phonons in a coherent state is given by:

$$p^{(\mathrm{coh})}(k) = e^{-\bar{k}}\frac{\bar{k}^k}{k!} \quad , \tag{5.48}$$

with $\bar{k} = |\alpha|^2$. Even for moderate coherent state sizes, detectable frequency shifts are expected for Rydberg excitation. If the ion is not perfectly cooled to the motional ground state before exciting the coherent state, residual temperature effects have to be considered and the phonon distribution becomes more complex. Each Fock state reacts differently on the displacement operation and a thermal coherent state is given by [Zie13]:

$$p^{(\mathrm{th,coh})}(k) = \sum_{m=0}^{\infty} p^{(\mathrm{th})}(m) e^{-|\alpha|^2} |\alpha|^{2(k+m)} m!k! \left|\sum_{l=0}^{m}\frac{(-1)^l |\alpha|^{-2l}}{l!(m-l)!(k-l)!}\right|^2 \quad . \tag{5.49}$$

For an ion initially in the vacuum state, the Fock state with zero phonons, equation 5.49 reduces to the description of a pure coherent state. Motional occupation corresponding to a finite ion temperature as well as heating of motional modes lead to a broadening of the coherent state phonon distribution. However, for cooling close to the

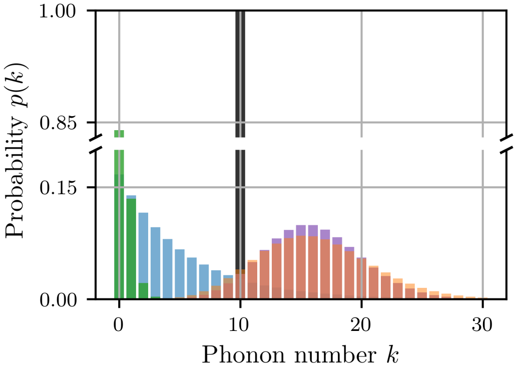

**Figure 5.1:** Phonon distributions $p(k)$ of a single trapped ion with $\omega_y = 2\pi \cdot 2.1\,\text{MHz}$ for a thermal state after Doppler cooling (blue), sideband cooling (green) to $\bar{k} = 0.2$, Fock state $k = 10$ (black), a coherent state with $\alpha = 4$ (purple) and a thermal coherent state after sideband cooling (orange).

motional ground state the temperature effects are negligible for coherent state sizes with average phonon numbers much larger than the initial phonon number. For the presented experiments, the final phonon distribution is assumed to be well approximated by a pure coherent state and a comparison of the discussed phonon distributions is given in figure 5.1. The blue data show the probability to find the ion in a certain phonon state for $\omega_y = 2\pi \cdot 2.1\,\text{MHz}$ after Doppler cooling with $\bar{k} = 5$, while the green data correspond to a sideband cooled ion with $\bar{k} = 0.2$. Purple and orange represent coherent and thermal coherent states, with $|\alpha| = 4$ and $\bar{k} = 0.2$, respectively. The Fock state $|10\rangle$ is indicated in black.

## A Driven Harmonic Oscillator

Coherent states are displaced harmonic oscillator ground states, but also solutions to the classical driven harmonic oscillator [Oh89, Kim96]. Strong coupling between an external driving field and the ionic motion can be achieved by resonantly exciting the ion's vibration. Applying an external field with frequency $\Omega_\text{ext}$ allows to individually address single oscillator modes or a superposition of modes, dependent on the direction of the external field. For instance, any radio-frequency field applied to one of the endcaps excites the axial motion of the ion. Resonant driving with $\Omega_\text{ext} = \omega_z$ excites the ion to strong oscillation along the axis and generates a coherent motional state. Analogously, the trap geometry allows for individual addressing of both radial modes via the compensation electrodes. This method is often referred to as *tickling* the ion, where the external frequency is varied and the ion's motion is observed by measuring the laser induced fluorescence. The Doppler shift of the excited motion with respect to the atomic transition allows for an extraction of the vibrational frequency. A second method to determine the vibrational frequencies of the ion utilizes sideband spectroscopy on the narrow quadrupole transition near 729 nm.

Once the secular frequencies are known, sideband cooling can be applied to initialize the ion close to the motional ground state. Afterward, coherent states might be excited by two methods: On the one hand a fast electric field kick with controlled pulse time [Alo16], which is further discussed in section 6.1 and on the other hand a resonant electric field $\Omega_{\text{ext}}$ driving the ion motion. The latter is employed by feeding 100 periods with constant amplitude of a given external drive onto one of the compensation electrodes to excite radial motion, here along $y$. The static compensation voltage, which positions the ion in the center of the oscillating trap potential, is superimposed by $\Omega_{\text{ext}}$ via various electronic components (e.g. switches, bias tee, ...). This allows for control of both static and dynamic electric field, while protecting the external field source from current spikes due to switching between different sets of compensation voltages. The geometry of the applied control voltage with respect to the ion and a spectral narrow electric field pulse with a length of 100 periods minimizes motional excitation along the directions $x$ and $z$. Driving the harmonic oscillator on resonance allows to control the coherent state size by the amplitude of the external field and the final phonon distribution can be probed by excitation probabilities of the red and blue sideband on the quadrupole transition, where the effective Rabi frequency depends on the phonon number. Figure 5.2 shows red and blue sideband of the radial mode $\omega_y = 2\pi \cdot 2.1\,\text{MHz}$ initialized by sideband cooling (triangles, left) and after coherent state excitation with frequency $\Omega_{\text{ext}} = \omega_y$ and peak-peak amplitude 30 mV (circles, right), see also figure 2.4 in section 2.3. The probability to find the ion in the dark $3\text{D}_{5/2}$ state after a laser pulse with duration $t$ can be calculated by [Roo00]:

$$p_{\text{D}}(t) = \frac{1}{2}\left(1 - \sum_{k=0}^{\infty} p(k)\cos(2\Omega_k t)\right) \quad . \tag{5.50}$$

Here, the Rabi frequency $\Omega_k$ for a given motional state and sideband transition is weighted by the phonon distribution $p(k)$, where either a thermal or coherent distribution is assumed. For very low phonon numbers the factors $\sqrt{k}, \sqrt{k+1}$ dominate the population dynamics, such that the red sideband is barely excited while the blue sideband shows Rabi oscillations with high contrast. Contrary, coherent states allow for large average phonon numbers and red and blue sidebands show similar dynamics,

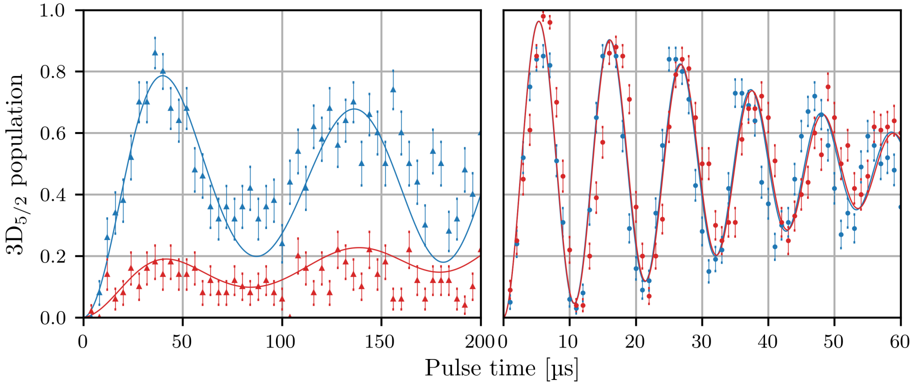

**Figure 5.2:** Population in 3D$_{5/2}$ by excitation of the red and blue sideband as a function of laser interaction time for an ion close to the motional ground state (left) and after resonant driving by an external field (right). Solid lines show correlated fits to the data yielding an average phonon number after sideband cooling $\bar{k}_y = 0.26(6)$ and a coherent state size $|\alpha| = 9.2(8)$.

as the difference in the square roots are on the level of a few percent for coherent states with $|\alpha| \geq 3$. Generally, the coupling strength of the laser field to a coherent state is much larger compared to the motional ground state due to the phonon number contribution. Solid lines in figure 5.2 show fits of the thermal and coherent state model to the data, which allows to extract an average phonon number after sideband cooling of $\bar{k}_y = 0.26(6)$ and a final coherent state size $|\alpha| = 9.2(8)$. Varying the amplitude of the external driving field, the size of the coherent state can be systematically controlled within $|\alpha| < 11$.

The stability of coherent states inside the trap field is confirmed by varying the time between motional excitation and state detection. The results indicate, that the coherent state size is unaltered within the required measurement time up to 1 ms, but the thermal contribution is increasing as discussed in section 4.3. Usually, the excitation of large coherent states with 100 periods and consecutive probe pulse or Rydberg excitation takes less than 200 µs, such that heating is negligible. Nevertheless, the motional excitation of one radial mode affects the second radial mode and a variation in phonon distribution due to the external field needs to be considered. This might originate from a non-perfect pulse shape of the excitation field or non perpendicular vibrational modes. Even though the pulse shape can be observed before the vacuum feedthrough, the electric signal is filtered again at the compensation electrode, such that the resulting field at the ion is not accessible. Measurements outside of the vacuum show alteration of pulse length and amplitude for square pulses due to the control electronics, while sine pulses deviated only little from the input shape. Applying multiple periods with less amplitude leads to even better transmission to the vacuum feedthrough. However, if the external field interacting with the ion is not resembled by a single frequency $\Omega_{\mathrm{ext}}$ but rather a superposition of multiple frequencies, the coherent excitation of the addressed mode gets reduced while off-resonant excitation of other vibrational modes arise. The same holds true, if the direction of the external field is not parallel to the desired motion and has a projection onto the other two oscillations, which could be caused by misalignment of the trap electrodes or an asymmetric trap potential. For larger separation of vibrational frequencies along the radial directions, the addressing of the desired mode by the external drive field is improved and off-resonant excitation can be further minimized by using less amplitude in individual sine pulses. Also, applying the voltage on two opposing compensation electrodes to generate a more symmetric force would be beneficial, but the frequency generator was already close to the minimal voltage settings at 100 sine pulses. Overall, the setup allows to excite coherent states of motion along a specific trap direction with only little effect on the other modes by using multiple periods of a resonant drive field with low amplitude.

The excited coherent states sizes $|\alpha| < 11$ result in average phonon numbers $\bar{k} < 121$ and can be used to study lineshape modifications of Rydberg transitions due to state-dependent trap frequencies, eventually allowing to extract the Rydberg state polarizability. To achieve higher coherent states as presented in [Alo16] the electrical connections for application of an external field have to be improved to allow for more precise control of the pulse shape and pulse direction. Also, better ground state cooling prior to the coherent excitation and larger separation of vibrational modes would reduce thermal phonon contributions to the motional states. Fortunately, the investigated coherent state sizes are large enough for an observation of Rydberg state polarizabilities, which couple the motion of the ionic core to the energy differences of high-lying Rydberg states. The expected shift of the transition frequency to $50\mathrm{S}_{1/2}$ with $|\alpha| = 10$ is $\Delta\nu \approx 3.7\,\mathrm{MHz}$ compared to the transition frequency of an ion in the motional ground state. The estimation uses literature values for the polarizability, which stem from Kratzer-Fues model potential calculations for the second-order Stark effect in Rydberg ions [Kam14].

## 5.2 Determination of the Ion's Polarizability by Enlarging the Wave Packet

Analogously to section 4.3, Rydberg transition lineshapes are probed by two-photon excitation from the metastable $3D_{5/2}$ state. The first transition laser near 213 nm is detuned several tens of MHz from the intermediate atomic resonance to minimize population loss by unwanted scattering. The second transition laser near 286 nm excites the ion to the Rydberg state and a successive decay into the electronic ground state is probed by fluorescence measurement. Varying the two-photon detuning $\Delta\nu$ by changing the laser frequency of the second deep UV laser allows to record a transition lineshape. Due to state-dependent trap frequencies, the phonon distributions along the radial oscillations of the ion prior to Rydberg excitation modifies the resulting transition lineshape. The resolution of frequency shifts is limited by the linewidth broadening from ion temperature and both deep UV lasers linewidths. Additionally, an imperfect electronic state preparation and off-resonant scattering from the intermediate $5P_{3/2}$ state diminish the contrast of the Rydberg lineshape.

Here, Rydberg $nS_{1/2}$-states with principal quantum number $n = \{49, 53, 57\}$ are probed for various initial coherent state sizes to extract the principal quantum number scaling of the polarizability. For each experiment the ion is prepared close to the motional ground state for radial oscillations and initialized in the $3D_{5/2,-5/2}$ Zeeman sub-state. Afterward, applying 100 periods of an external field with $\Omega_{\mathrm{ext}} = \omega_y$ excites a coherent motional state along $y$ without changing the electronic excitation or largely affecting phonon distributions of modes along the other directions. An excitation into Rydberg states probes the phonon distributions along both radial modes as well as Doppler and linewidth broadening, such that the resulting transition lineshape is given by multiple independent parameters. Figure 5.3 presents excitation spectra of the $57S_{1/2}$ state as a function of two-photon detuning for different coherent state sizes. To precisely determine the resonance frequency, the transition to Rydberg states for coherent motional excitation is measured simultaneously with the Rydberg excitation spectrum of a sideband cooled ion, such that the unperturbed transition frequency and the polarizability are extracted from a correlated fit of both data sets with the lineshape model. Other parameters as phonon distributions before and after coherent state excitation and vibrational frequencies are determined by independent measurements. Technically, any two Rydberg excitation spectra with known phonon distributions might be used to extract transition frequency and polarizability, but for better comparison all reference spectra were recorded with a sideband cooled ion $|\alpha| = 0$. In

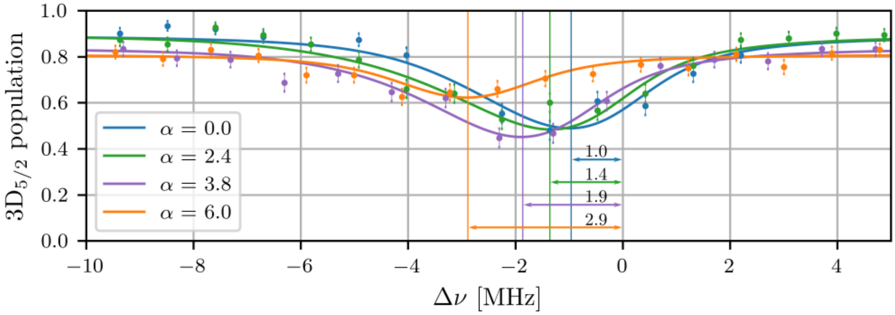

**Figure 5.3:** $3D_{5/2}$ depopulation by $57S_{1/2}$ state excitation as a function of two-photon detuning for a single ion prepared in the motional ground state (blue) and different coherent motional excitation (green, purple and orange) with $|\alpha| > 0$. Solid lines show fits with the lineshape model assuming a coherent phonon distribution along $y$ and vertical lines indicate the two-photon detuning for maximal depopulation.

figure 5.3 blue and green data points were recorded interleaved and the reference data for higher coherent states are not shown for clarity. Vertical lines denote the frequency with the highest excitation rate to the Rydberg state, which shift away from the two-photon resonance for larger coherent states. A deviation from $\Delta\nu = 0$ for the blue data points originates from residual thermal phonons in both radial modes. Different coherent state sizes are recorded within multiple measurements over the course of days, which results in varying excitation strengths and off-resonant excitation levels, nevertheless, allow to extract the polarizability as a function of principal quantum number.

For Rydberg $nS_{1/2}$-states with $n = \{49, 53, 57\}$ and coherent motional excitation $2 < |\alpha| < 10$ the obtained polarizability is presented in figure 5.4. All individual measurements of the polarizability are weighted by the respective fit error (including coherent state size and initial ion temperature) and averaged for the three principal quantum numbers. The resulting mean value is presented as green lines with shaded $1\sigma$ confidence bands and agrees with theory (purple) [Kam14], as given by:

| | This work | [Kam14] |
|---|---|---|
| $\mathcal{P}(49S_{1/2})$ $[10^{-30}\ \frac{\mathrm{Cm}^2}{\mathrm{V}}]$ | 1.3(2) | 1.24 |
| $\mathcal{P}(53S_{1/2})$ $[10^{-30}\ \frac{\mathrm{Cm}^2}{\mathrm{V}}]$ | 2.2(2) | 2.18 |
| $\mathcal{P}(57S_{1/2})$ $[10^{-30}\ \frac{\mathrm{Cm}^2}{\mathrm{V}}]$ | 3.6(3) | 3.68 |

Note, that recording transition spectra to Rydberg states requires substantial amount of time for characterization and optimization protocols to quantitatively analyze the

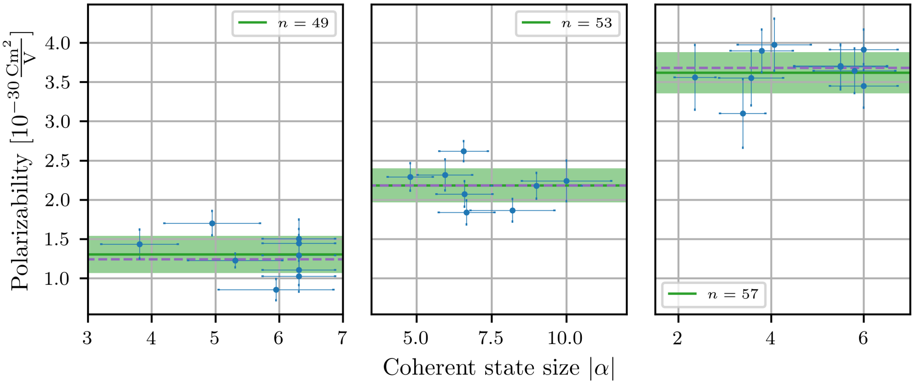

**Figure 5.4:** Extracted Rydberg state polarizabilities for different principal quantum numbers and various coherent state initializations. The weighted average (green) with $1\sigma$ confidence interval (shaded green) for each principal quantum number agrees with theory calculations (purple).

transition lineshape. A brief overview is given in the following. Typically, each data point consists of $50 - 200$ individual repetitions of the same experimental sequence and probing a full Rydberg excitation spectrum takes less than 15 minutes, depending on the frequency range and the step size. However, ion losses due to double ionization events interrupt the experiment and require to restart the measurement if ion reloading is not done within a fraction of a minute. Since potential settings for ion loading and experiment are different, a switching between these voltage sets leads to drifts of vibrational mode frequencies for some time after reloading. To provide sufficient sideband cooling and coherent motional excitation the vibrational frequencies have to be regularly measured and corresponding laser frequencies and external fields are adjusted, typically before each Rydberg excitation spectrum. Additionally, the electric field compensation, which positions the ion in the center of the oscillating quadrupole field, is employed multiple times throughout the day to minimize the quadratic Stark effect on Rydberg states. Laser sources for Doppler cooling and manipulation of low-lying electronic states are sufficiently stable, such that no regular optimization protocol is required. The Rydberg excitation lasers, however, tend to drift in frequency due to the temperature sensitivity of the optical resonator. Relative measurements between two interleaved Rydberg spectra with different parameters are more reliable than absolute frequency measurements. Though, additional measurements of Rydberg excitation spectra increase the probability of losing the ion, such that the employment of an ultra-stable reference resonator for both deep UV laser sources becomes necessary for a faster and more accurate data acquisition in the future.

Within the experimental accuracy, the extracted polarizabilities agree with theory calculations and follow the expected principal quantum number scaling as $\mathcal{P} \propto n^7$. Future improvements to the setup and initial state preparation may reduce the Rydberg transition linewidth drastically and allow for much more accurate measurements of phonon-dependent shifts of the Rydberg state energy, even for small coherent state sizes. Accessing Rydberg state polarizabilities for a variety of principal quantum numbers allows to further study the scaling laws of Rydberg properties and can be used to specifically tailor the state-dependent trap frequencies for applications in fundamental physics of structural phase transitions, quantum computation and quantum sensing. Additionally, using microwave dressing to Rydberg $n\mathrm{P}_{1/2}$-states, with opposite sign of the polarizability, enables full control of the magnitude of the polarizability, eventually leading to even larger polarizabilities and transition shifts. Overall, dedicated measurements of the Rydberg state polarizabilities lead to better understanding of quadratic Stark effects on Rydberg states and allow to use highly excited ions as accurate and sensitive detectors for electric fields.

# 6

# It's Exciting II: Fast Motional Excitation for Quantum Computing

State-dependent trap frequencies are an intrinsic feature of trapped Rydberg ions and can be engineered by dressing different angular momentum Rydberg states or by varying the trap field gradients. Already single ions experience a phonon-dependent shift of their Rydberg transition frequencies. For larger ion crystals the coupled motion within the harmonic potential can be utilized for quantum computation and simulation. The switchable interaction introduced by excitation into Rydberg states and engineering of polarizabilities extends the toolbox of manipulating the ion, typically driven by lasers. Here, the state-dependent trap frequencies of a two-ion crystal influenced by a time-dependent external field are applied to propose an ultra-fast entanglement operation without additional laser interaction.

The first part of this section describes the Hamiltonian of two trapped ions with state-dependent trap frequencies and their Coulomb interaction inside the linear Paul trap. For different electronic states the respective equilibrium positions and the coupled motion of the two ions are derived. Afterward, a displacement field is introduced and the motional state evolution of the crystal is studied with respect to its the phase space trajectory. Fine tuning of the pulse shape and the initial trap field gradient allows for generation of entanglement by implementing a controlled phase gate. A theoretical limit for the entanglement error is estimated. Finally, prospects of the scheme are given by including more complex displacements of the ion crystal, which reduce the interaction time to less than 100 ns. All theoretical calculations are performed with experimentally accessible parameters. The results are published in ”Shuttling of Rydberg Ions for Fast Entangling Operations” [Vog19]

## 6.1 Displacement of Two Ions by a Fast Electric Kick

Two ions confined in a harmonic potential are coupled by their mutual Coulomb interaction and form common vibrational modes with oscillation frequencies depending on the ionic charge, the mass and the trap field gradient. For typical operation of a linear Paul trap the motion along axial and radial directions is separable, such that for simplicity only the axial motion is considered within the following discussion. Also, it is assumed that the ions are cooled to the motional ground state, such that Rydberg excitation is not altered by phonon-dependent shifts, although generation of large coherent states of motion will be covered. Within this section $|{\downarrow}\rangle$ refers to ions in a low-lying electronic state (e.g. the $3D_{5/2}$ state for $^{40}\mathrm{Ca}^{+}$) while a Rydberg state is noted as $|{\uparrow}\rangle$. The state evolution for two ions can be effectively described by basis states consisting of $|\alpha\beta\rangle = \{|{\downarrow\downarrow}\rangle, |{\uparrow\downarrow}\rangle, |{\downarrow\uparrow}\rangle, |{\uparrow\uparrow}\rangle\}$. A combination of state-dependent confinement along the trap axis and the Coulomb interaction leads to a potential:

$$V^{\alpha\beta} = \frac{1}{2}M\left(\omega^{\alpha}\right)^2 Z_1^2 + \frac{1}{2}M\left(\omega^{\beta}\right)^2 Z_2^2 + \frac{\mathrm{C}}{|Z_1 - Z_2|} \quad . \tag{6.51}$$

Indices denote the ion with position $Z$ along the trap axis and $\mathrm{C} = {e^2}/{4\pi\epsilon_0}$ is the Coulomb constant. The interplay between confining Paul trap and Coulomb repulsion results in a steady state with fixed interparticle distance. Two vibrational modes arise along the axis, one, where both ions oscillate in-phase and one, where the ions oscillate out-of-phase. If the confinement between the two ions varies, the crystal experiences different coupling of both ions to the common motion as well as asymmetric equilibrium positions.

Displacing both ions simultaneously by an external electric field, the center-of-mass mode is excited and the ions start to oscillate around shifted equilibrium positions. Consequently, switching off the displacement field restores the initial positions. Any residual motional excitation can be controlled by the relative timing of displacement field and motional frequency. A sketch of the displacement field exciting a single ion is given in figure 6.1, where the electric field (green) generates a large amount of phonons (blue) and the evolution of the ion wave packet in the displaced harmonic oscillator is schematically shown in the upper panel. For two states with different initial confinement, the ion follows distinguishable trajectories in phase space while influenced by the electric field as presented for the gray and red wave packets corresponding to states $|{\downarrow}\rangle$ and $|{\uparrow}\rangle$, respectively. Thereby, the two states accumulate a differential phase depending on the trap frequencies (dark red). Arbitrary phase rotations are possible on a single ion, while two-ion crystals can be entangled with a controlled phase gate

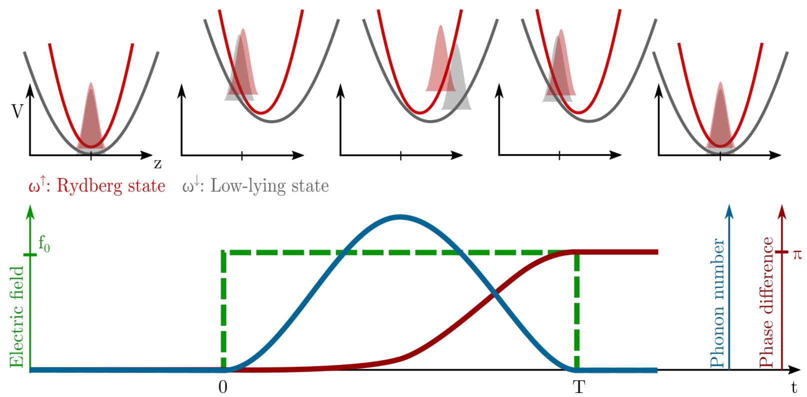

**Figure 6.1:** Scheme for a shuttle-based state-dependent phase accumulation. An ion trapped in a harmonic potential is displaced by an electric field (green), which generates a large amount of motional excitation (blue). For two different confinements (gray/red), realized by the large polarizability of Rydberg states, the ion accumulates a different phase during the evolution in the displaced potential (dark red).

utilizing this scheme. The electric field amplitude determines the size of the generated coherent state as well as the accumulated phase, while the pulse time can be chosen to minimize residual motional excitation. Optimally, the pulse time is related to the oscillation frequency and sequence durations less than one µs are possible, which is two orders of magnitude smaller compared to typical laser-driven entanglement operations for trapped ions [Ben08, Bal16, Gae16]. Also, a laser-less controlled phase gate would benefit from established control and fast switching of electric fields used anyway in current ion trap experiments [Wal12, Bow12]. Within the following section, the proposal for entangling tow ions by fast displacement pulses is discussed in detail.

## State-Dependent Equilibrium Positions

The interaction of trapped Rydberg ions with an external electric field, eventually leading to a fast entanglement operation, is discussed with respect to the state-dependent trap potential. The latter is studied for ions around their respective equilibrium positions $\bar{Z}_j^{\alpha\beta}$ and the dynamics due to the collective oscillation is accessed. Analogous to coupled oscillators with different mass, the interparticle distance in the steady state will be a function of the electronic states. The state-dependent equilibrium positions of two ions are found by the force-balance condition:

$$\left.\frac{\partial V^{\alpha\beta}}{\partial Z_1}\right|_{Z_1=\bar{Z}_1^{\alpha\beta}} = \left.\frac{\partial V^{\alpha\beta}}{\partial Z_2}\right|_{Z_2=\bar{Z}_2^{\alpha\beta}} = 0 \quad . \tag{6.52}$$

Solving equation 6.52 for the equilibrium positions yields:

$$\bar{Z_1}^{\alpha\beta} = \left[\frac{\mathrm{C}\left(\omega^{\beta}\right)^4}{M\left(\omega^{\alpha}\right)^2\left(\left(\omega^{\alpha}\right)^2+\left(\omega^{\beta}\right)^2\right)^2}\right]^{\frac{1}{3}} \quad , \tag{6.53}$$

$$\bar{Z_2}^{\alpha\beta} = -\left[\frac{\mathrm{C}\left(\omega^{\alpha}\right)^4}{M\left(\omega^{\beta}\right)^2\left(\left(\omega^{\alpha}\right)^2+\left(\omega^{\beta}\right)^2\right)^2}\right]^{\frac{1}{3}} \quad . \tag{6.54}$$

Given by the state-dependent trap frequencies the interparticle distance decreases for stronger confinement along the axis. The steady state positions are symmetric around the center of mass for identical electronic states or asymmetric for two ions with one Rydberg excitation. The centroid crystal position $Z_{\mathrm{C}}^{\alpha\beta}$ follows from:

$$Z_{\mathrm{C}}^{\alpha\beta} = \bar{Z_1}^{\alpha\beta} + \bar{Z_2}^{\alpha\beta} = \frac{\mathrm{C}^{\frac{1}{3}}\left(\left(\omega^{\beta}\right)^2-\left(\omega^{\alpha}\right)^2\right)}{\left[M\left(\omega^{\alpha}\omega^{\beta}\right)^2\left(\left(\omega^{\alpha}\right)^2+\left(\omega^{\beta}\right)^2\right)^2\right]^{\frac{1}{3}}} \quad . \tag{6.55}$$

For ions in the same electronic state, the centroid position overlaps with the center of mass. For motion of the crystal driven by residual temperature or external fields, the position of the ions is discussed with respect to their equilibrium position. Hence, equation 6.51 is expanded for small variations from the equilibrium positions $\bar{Z_j}^{\alpha\beta} + z_j$ up to second order:

$$V^{\alpha\beta} \approx \frac{Mz_1^2}{2}\left[\left(\omega^{\alpha}\right)^2+\left(J^{\alpha\beta}\right)^2\right] + \frac{Mz_2^2}{2}\left[\left(\omega^{\beta}\right)^2+\left(J^{\alpha\beta}\right)^2\right] - M\left(J^{\alpha\beta}\right)^2 z_1 z_2 + V_0^{\alpha\beta} \tag{6.56}$$

with

$$\left(J^{\alpha\beta}\right)^2 = \frac{2\left(\omega^{\alpha}\omega^{\beta}\right)^2}{\left(\omega^{\alpha}\right)^2+\left(\omega^{\beta}\right)^2} \tag{6.57}$$

and the equilibrium positions given by equations 6.53 and 6.54. The term $V_0^{\alpha\beta}$ is independent of variations in the ion position, but state dependent. This static energy should be visible as difference in the excitation energies for zero, one or two Rydberg excitations. Though, for typical experimental parameters with Calcium ions the energy shift is negligible and will not be considered further. The force-balance condition cancels linear contributions of $z_j$ within the potential $V^{\alpha\beta}$ and only quadratic terms, as well as one term mixing the positions $z_1$ and $z_2$ are present. To diagonalize the potential, it is useful to introduce relative coordinates $q_j$ for the coupled ion motion by a state-dependent mixing angle $\theta^{\alpha\beta}$ as:

$$\begin{pmatrix} z_1 \\ z_2 \end{pmatrix} = \begin{pmatrix} \cos(\theta^{\alpha\beta}) & -\sin(\theta^{\alpha\beta}) \\ \sin(\theta^{\alpha\beta}) & \cos(\theta^{\alpha\beta}) \end{pmatrix} \begin{pmatrix} q_1 \\ q_2 \end{pmatrix} \quad . \tag{6.58}$$

The relative coordinates can be related to the in-phase and out-of-phase motion, where both ions either move in the same or the opposite direction, respectively. For a mixing angle $\theta^{\alpha\beta} = \pi/4$ both ions are equally coupled to each of the two crystal vibrations. Using a state-dependent mixing angle the potential is described as:

$$\begin{aligned} V^{\alpha\beta} = & \frac{M}{2}\left(\left(\omega_1^{\alpha\beta}\right)^2 q_1^2 + \left(\omega_2^{\alpha\beta}\right)^2 q_2^2\right) \\ & + \frac{M}{2}\left[\left(\left(\omega^{\alpha}\right)^2 - \left(\omega^{\beta}\right)^2\right)\sin(2\theta^{\alpha\beta}) - 2\left(J^{\alpha\beta}\right)^2\cos(2\theta^{\alpha\beta})\right] q_1 q_2 \end{aligned} \tag{6.59}$$

with

$$\begin{aligned} \left(\omega_j^{\alpha\beta}\right)^2 = & \omega^{\alpha}\omega^{\beta}\left[\left(\frac{\omega^{\beta}}{\omega^{\alpha}}\right)^{(-1)^j}\cos^2(\theta^{\alpha\beta}) + \left(\frac{\omega^{\alpha}}{\omega^{\beta}}\right)^{(-1)^j}\sin^2(\theta^{\alpha\beta})\right] \\ & + \left(J^{\alpha\beta}\right)^2\left[1 + (-1)^j\sin(2\theta^{\alpha\beta})\right] \quad . \end{aligned} \tag{6.60}$$

Overall, equation 6.59 is similar to equation 6.56, but with relative coordinates instead of the individual ion positions. Choosing an mixing angle that depends on the electronic state of the two ions, the transformed potential can be diagonalized. Using

$$\theta^{\alpha\beta} = \frac{\pi}{4} - \frac{1}{2}\arctan\frac{\left(\omega^{\alpha}\right)^2 - \left(\omega^{\beta}\right)^2}{2\left(J^{\alpha\beta}\right)^2} \quad , \tag{6.61}$$

the difference of state-dependent trap frequencies describes the relative motion of both ions. Thereby, the potential is described by a harmonic oscillator with two vibrations of the relative coordinates $q_j$ and frequency $\omega_j^{\alpha\beta}$. The relative amplitude for each individual ion is given by the angle $\theta^{\alpha\beta}$ and leads to an unequal oscillation strength if both ions are in different electronic states.

Here, the polarizability modifies the trap frequency of Rydberg ions compared to ions in low-lying electronic states. A lower trap frequency leads to weaker coupling to the center-of-mass motion, while the amplitude in the stretch mode is larger. Contrary, if both ions are in identical electronic states with $\omega^{\alpha} = \omega^{\beta} = \omega$ the mixing angle reduces to $\pi/4$ and simplifies the potential to $V = \frac{M}{2}\left(\omega^2 q_1^2 + 3\omega^2 q_2^2\right)$. As given by typical experiments with identical trapped ions, both ions contribute equally to in-phase and out-of-phase motion. Overall, changing the polarizability of an ion inside the oscillating trap fields has the same effect on the motion as effectively changing the ion's mass.

At low temperatures, the motion within the harmonic potential can be described by phonons and the energy is quantized by the occupation of vibrational energy levels. The corresponding creation and annihilation operators from equation 2.29 and 2.30 become state dependent and are related to the relative coordinates by:

$$q_j = \frac{l_j^{\alpha\beta}}{\sqrt{2}} \left( \tilde{a}_j + \tilde{a}_j^{\dagger} \right) \quad . \tag{6.62}$$

The state-dependent operators are abbreviated by $\tilde{a} = a^{\alpha\beta}$ and the characteristic length $l_j^{\alpha\beta}$ is given by

$$l_j^{\alpha\beta} = \sqrt{\frac{\hbar}{M\omega_j^{\alpha\beta}}} \quad . \tag{6.63}$$

The characteristic length refers to the extension of the harmonic oscillator wave packet in the motional ground state. For larger vibrational frequency and corresponding stronger confinement the ion's motion is much more localized within the trap. Any thermal phonon distribution leads to a broadening of the wave packet and for coherent motional excitation the wave packet itself oscillates with an amplitude given by the coherent state size.

Expressing the interaction of two trapped ions in terms of creation and annihilation operators one finds the unperturbed Hamiltonian $H^{\alpha\beta}$. For completeness, the Hamiltonian needs to be projected by $\Pi^{\alpha\beta} = |\alpha\rangle_1 \langle\alpha|_1 \otimes |\beta\rangle_2 \langle\beta|_2$ and summed over all possible basis states to obtain:

$$H_{\text{phonon}} = \sum_{\alpha\beta=\uparrow,\downarrow} H^{\alpha\beta}\, \Pi^{\alpha\beta} \tag{6.64}$$

$$= \sum_{\alpha\beta=\uparrow,\downarrow} \left( \sum_{j=1}^{2} \hbar\omega_j^{\alpha\beta} \tilde{a_j}^{\dagger} \tilde{a_j} \right) \Pi^{\alpha\beta} \quad . \tag{6.65}$$

The ground state energy of the coupled harmonic oscillator is neglected analogously to the static energy shift $\tilde{V}_0^{\alpha\beta}$. Though, the occupation of both phonon modes is sufficient to describe the dynamics of the crystal with state-dependent vibrations. For the interaction of the ion crystal with a fast electric field kick only the motional ground state is considered in detail.

### Interaction with a Time-Dependent External Force

An external electric field acts on the ion crystal by displacing both ions from their equilibrium positions within the harmonic trap. While a static potential only shifts the equilibrium positions and does not affect the dynamics of the ion motion, a time varying field can alter the phonon evolution of the crystal. Considering a time-dependent field $f(t)$ along the trap axis generates the driving Hamiltonian

$$\begin{aligned} H_{\text{driving}} &= f(t)(Z_1 + Z_2) = f(t)\left(\bar{Z}_1^{\alpha\beta} + z_1 + \bar{Z}_2^{\alpha\beta} + z_2\right) && (6.66)\\ &= f(t)\left[\left(\cos(\theta^{\alpha\beta}) + \sin(\theta^{\alpha\beta})\right) q_1 + \left(\cos(\theta^{\alpha\beta}) - \sin(\theta^{\alpha\beta})\right) q_2 + Z_{\text{C}}^{\alpha\beta}\right] && (6.67)\\ &= \sum_{j=1}^{2} F_j^{\alpha\beta}(t)\left(\tilde{a}_j + \tilde{a}_j^\dagger\right) + f(t) Z_{\text{C}}^{\alpha\beta} \quad . && (6.68) \end{aligned}$$

Thereby, the electric field is projected onto the two oscillations of the ion crystal and a displacement of the crystal center. For clarity, the summation over all basis states is omitted. As shown in equation 6.55 the last term of the driving Hamiltonian vanishes for ions in identical electronic states as they are symmetrically positioned with respect to the center of mass. The contribution of the electric field to the crystal oscillations is scaled by the respective characteristic length and reads

$$F_j^{\alpha\beta}(t) = f(t)\frac{l_j^{\alpha\beta}}{\sqrt{2}}\left(\cos(\theta^{\alpha\beta}) - (-1)^j \sin(\theta^{\alpha\beta})\right) \quad . \tag{6.69}$$

Note, an electric field parallel to the crystal axis addresses only the center-of-mass motion, if both ions are in the same electronic state. The scaling by the state-dependent oscillator length, however, leads to distinguishable effects between two ions in electronically low-lying states compared to a crystal consisting of two Rydberg ions. For the mixed basis states $|\uparrow\downarrow\rangle, |\downarrow\uparrow\rangle$ also the stretch mode is coupled to the electric field and a contribution from asymmetric equilibrium positions is present. Thereby, the basis states of the two-ion system evolve differently depending on the number of Rydberg excitations.

## 6.2 Phase Accumulation and State-Dependent Forces for Entanglement Generation

The interaction of driving force and coupled harmonic oscillator is described by the sum of both phonon and driving Hamiltonian $H_{\text{driving}} + H_{\text{phonon}}$. Intuitively, the application of a time-dependent external electric field is studied within the interaction picture, where the driving Hamiltonian is mapped onto the energy scale of the unperturbed system. Using the commutator algebra for creation and annihilation operators, the interaction Hamiltonian reads:

$$H_{\mathrm{I}} = e^{\frac{\mathrm{i}}{\hbar} H_{\mathrm{phonon}} t} H_{\mathrm{driving}} e^{-\frac{\mathrm{i}}{\hbar} H_{\mathrm{phonon}} t} \tag{6.70}$$

$$= \sum_{\alpha\beta} \left( \sum_{j=1}^{2} \left( F_j^{\alpha\beta}(t) e^{i\omega_j^{\alpha\beta} t} \tilde{a}_j + \mathrm{h.c.} \right) + f(t) Z_{\mathrm{C}}^{\alpha\beta} \right) \Pi^{\alpha\beta} \quad , \tag{6.71}$$

where h.c. denotes the Hermitian conjugate. As the ion displacement acts on the individual vibrational modes and the phonon Hamiltonian is diagonal, also the interaction Hamiltonian does only linearly depend on creation and annihilation operators. Without specifying the pulse shape, the time dependency is governed by the oscillation of the ion crystal with vibrational frequency $\omega_j^{\alpha\beta}$ and thereby, all basis states evolve at different rates. Analogous to the discussion of the driving force, ion crystals with a single Rydberg excitation experience an interaction due to the asymmetric crystal center, which is not present for ions in identical electronic states. In this case, also the stretch mode is not addressed.

## Evolution Operator in the Interaction Picture

Overall, the interaction Hamiltonian is dependent on the number of Rydberg excitations within the crystal and the time evolution of the driven system is found by a Magnus expansion [Mag54, Bla10]. This is necessary, since the interaction Hamiltonian does not commute with itself, if evaluated at different times. A time ordering of the system is introduced by investigating corresponding commutators $[H_{\mathrm{I}}(\tau'), H_{\mathrm{I}}(\tau)]$. Then, the evolution operator can be expressed as infinite series

$$\begin{aligned} U_{\mathrm{I}}(t) = \exp \Bigg[ -\mathrm{i} \int_{t_0}^{t} H_{\mathrm{I}}(\tau) \mathrm{d}\tau - \frac{1}{2} \int_{t_0}^{t} \int_{t_0}^{\tau'} \left[ H_{\mathrm{I}}(\tau'), H_{\mathrm{I}}(\tau) \right] \mathrm{d}\tau \mathrm{d}\tau' \\ + \frac{\mathrm{i}}{6} \int_{t_0}^{t} \int_{t_0}^{\tau''} \int_{t_0}^{\tau'} \big( [H_{\mathrm{I}}(\tau''), [H_{\mathrm{I}}(\tau'), H_{\mathrm{I}}(\tau)]] \\ + [H_{\mathrm{I}}(\tau), [H_{\mathrm{I}}(\tau'), H_{\mathrm{I}}(\tau'')]] \big) \mathrm{d}\tau \mathrm{d}\tau' \mathrm{d}\tau'' + \cdots \Bigg] \quad . \end{aligned} \tag{6.72}$$

The time ordering is included by integration of the interaction Hamiltonian and its commutator for different times. Using the commutator relations $\left[\tilde{a}_i, \tilde{a}_j^{\dagger}\right] = \delta_{ij}$ and

$\left[\tilde{a}_i, \tilde{a}_j\right] = \left[\tilde{a}_i^\dagger, \tilde{a}_j^\dagger\right] = 0$, the integrand of the second term becomes:

$$[H_\mathrm{I}(\tau'), H_\mathrm{I}(\tau)] = \sum_{\alpha\beta} \left( -2\mathrm{i} \sum_{j=1}^{2} F_j^{\alpha\beta}(\tau') F_j^{\alpha\beta}(\tau) \sin\left[\omega_j^{\alpha\beta}(\tau' - \tau)\right] \right) \Pi^{\alpha\beta} \quad . \tag{6.73}$$

Since equation 6.73 is independent of creation and annihilation operators, the Magnus expansion terminates after the second term and the total time evolution of the system is fully described. One part determines the dynamics of phonon creation and annihilation, which is originating from direct integration of the interaction Hamiltonian. The other part is independent of phonons and describes the phase evolution of the system. This arises from the commutator in equation 6.73 and the displacement of the crystal center for ion crystals with a single Rydberg excitation. In total, the time evolution is given by the displacement operator (equation 2.31) acting on the coupled vibration of the two ions and a phase evolution yielding:

$$U_\mathrm{I}(t) = \sum_{\alpha\beta} \prod_{j=1}^{2} \left[\mathcal{D}\left(A_j^{\alpha\beta}(t)\right)\right] \exp\left[\mathrm{i} \sum_{j=1}^{2} \varphi_j^{\alpha\beta}(t) - \Phi_\mathrm{e}^{\alpha\beta}(t)\right] \Pi^{\alpha\beta} \tag{6.74}$$

with

$$A_j^{\alpha\beta}\left(f(t), \omega_j^{\alpha\beta}, t\right) = \int_{t_0}^{t} F_j^{\alpha\beta}(\tau) e^{-\mathrm{i}\omega_j^{\alpha\beta}\tau} \mathrm{d}\tau \quad , \tag{6.75}$$

$$\varphi_j^{\alpha\beta}\left(f(t), \omega_j^{\alpha\beta}, t\right) = \int_{t_0}^{t} \int_{t_0}^{\tau'} F_j^{\alpha\beta}(\tau') F_j^{\alpha\beta}(\tau) \sin\left[\omega_j^{\alpha\beta}(\tau' - \tau)\right] \mathrm{d}\tau \mathrm{d}\tau' \quad , \tag{6.76}$$

$$\Phi_\mathrm{e}^{\alpha\beta}\left(f(t), \omega_j^{\alpha\beta}, t\right) = \int_{t_0}^{t} f(\tau) Z_\mathrm{C}^{\alpha\beta} \mathrm{d}\tau \quad . \tag{6.77}$$

The state-dependent displacement operator for both crystal vibrations lead to a periodic generation of coherent motional states. Since the center-of-mass mode is excited for any applied field and all basis states of the ion crystal, fine tuning of the pulse shape and the state-dependent trap frequencies allow for a controlled excitation of coherent states. The average phonon number of such a displaced state is the square of the absolute argument, namely $\bar{k} = \left|A_j^{\alpha\beta}\right|^2$. Similarly, the phase factors $\Phi_\mathrm{e}^{\alpha\beta}$ and $\varphi_j^{\alpha\beta}$ lead to an accumulated phase when the ion crystal interacts with the electric field, where $\Phi_\mathrm{e}^{\alpha\beta}$ is only present for ion crystals with a single Rydberg excitation.

So far, the pulse shape is not specified and different electric fields may be considered. The most simple form is a short displacement of the ions by a square pulse with given amplitude and duration. The abrupt displacement can be seen as kicking the crystal within the harmonic potential and generating strong excitation in the center-of-mass motion. Contrary, varying the trap field gradient by pushing or pulling at the same time from both sides would be visible in the stretch mode (with adaptions to $H_{\mathrm{driving}}$). Also, the external electric field can be applied by a smooth pulse with time-dependent amplitude as this allows for more control of the motional excitation. Anyway, experimentally build in low-pass filters for noise reduction on the trap electrodes would deteriorate the voltages fed to the ion crystal and smooth pulses can be more easily transferred without deviation in pulse shape. Moreover, electrical switches have final rise and fall times depending on the amplitude of the external field [Sto21]. Another method might use multiple electric pulses with varying amplitude and duration, such that the harmonic oscillator is kicked multiple times to generate larger motional excitation. By choosing the corresponding pulse shape the driving of phonon modes can be specially engineered and allows for implementation of *bang-bang-* or *optimal-control* techniques [GR03, Can11, Alo16].

## Large Coherent States of Motion and Phase Space Trajectories

For a square pulse with amplitude $f_0$ and duration $T$ equation 6.74 is analytically solvable. More advanced pulse shapes can be investigated as well, but might require numerical integration. A constant displacement of the ion crystal is dependent on the trap field gradient and the time evolution of the crystal state is given by the corresponding trap frequencies. Within the following, the state-dependent displacement for a time $t \in [0, T]$ of two ions is described in quantities of phonon creation and phase accumulation:

$$\begin{aligned} A_j^{\alpha\beta}(f_0, \omega_j^{\alpha\beta}, T) &= \frac{f_0 l_j^{\alpha\beta}}{\sqrt{2}\omega_j^{\alpha\beta}} \left(e^{-\mathrm{i}\omega_j^{\alpha\beta} T} - 1\right) \\ &\quad \times \left[\cos\theta^{\alpha\beta} - (-1)^j \sin\theta^{\alpha\beta}\right] \quad , \qquad (6.78) \\ \varphi_j^{\alpha\beta}(f_0, \omega_j^{\alpha\beta}, T) &= \left(\frac{f_0 l_j^{\alpha\beta}}{\sqrt{2}\omega_j^{\alpha\beta}}\right)^2 \left[\omega_j^{\alpha\beta} T - \sin\left(\omega_j^{\alpha\beta} T\right)\right] \\ &\quad \times \left[\cos\theta^{\alpha\beta} - (-1)^j \sin\theta^{\alpha\beta}\right]^2 \quad , \qquad (6.79) \\ \Phi_{\mathrm{e}}^{\alpha\beta}(f_0, \omega_j^{\alpha\beta}, T) &= f_0 Z_{\mathrm{C}}^{\alpha\beta} T \quad . \qquad (6.80) \end{aligned}$$

In total, 16 evolution terms describe the phonon dynamics and the phase evolution for a two-ion crystal with four basis states and two common vibrational modes. As there

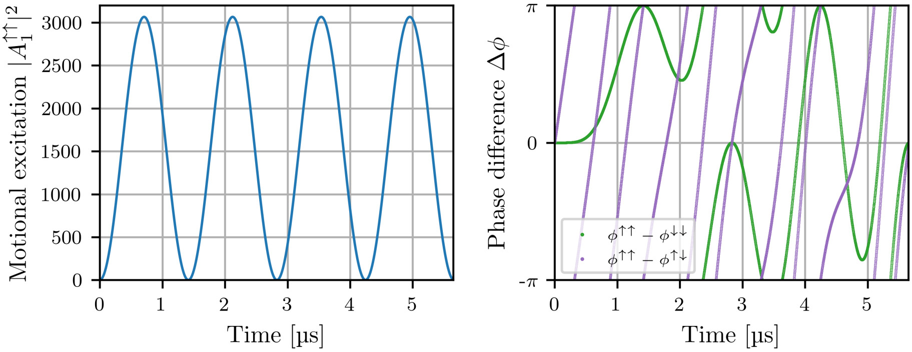

**Figure 6.2:** Generation of large coherent states of motion with average phonon number $\left|A_1^{\uparrow\uparrow}\right|^2$ (blue, left) and differential accumulated phase (green and purple, right) for a square electric field kick with duration $T$. Amplitude $f_0$ and trap frequency $\omega_1^{\uparrow\uparrow}$ are chosen to generate specific phase differences of $\Delta\phi = \pi$ between the basis states. The accumulated phase is shown modulo $2\pi$, see text for details.

is no site dependency in the calculations, basis states $|\uparrow\downarrow\rangle$ and $|\downarrow\uparrow\rangle$ are identical. Also, the stretch mode of two ions in identical electronic states is not excited. Consequently, eight terms for description of motional state and phase are nonzero. With respect to phonons, all contributions of the center-of-mass mode for different numbers of Rydberg excitations and the stretch mode for exactly one Rydberg excitation need to be considered. However, the factor $\left[\cos\theta^{\alpha\beta} - (-1)^j \sin\theta^{\alpha\beta}\right]$ leads to only small contributions of the stretch mode as long as the frequency difference between electronically low-lying and high-lying states is much smaller than the trap frequencies itself. For the center-of-mass mode, the amount of state-dependent displacement varies with $\left(\omega_1^{\alpha\beta}\right)^{-3/2}$ and periodicity of $\omega_1^{\alpha\beta}$. Thereby, generated phonons can be periodically returned to zero if the duration of the pulse matches the inverse trap frequency. A square pulse allows for addressing of just one mode at a time, but for basis states with trap frequency variations in the order of less than one percent, the residual phonon excitation of all modes can be reduced to average phonon numbers much smaller than one. Within this section the Rydberg excitation into $n\mathrm{P}_{1/2}$ states is considered, as they experience larger polarizabilities compared to $n\mathrm{S}_{1/2}$ states [Kam14]. Nevertheless, the proposed entanglement scheme is not limited by the choice of Rydberg states and different principal quantum numbers will be discussed. The excitation of the center-of-mass mode $\left|A_1^{\uparrow\uparrow}\right|^2$ for the Rydberg state $64\mathrm{P}_{1/2}$ is shown in figure 6.2 as a function of pulse time $T$ on the left. If the pulse duration equals a multiple of $2\pi/\omega_1^{\uparrow\uparrow}$ with $\omega_1^{\uparrow\uparrow} = 2\pi \cdot 706\,\mathrm{kHz}$, zero motional excitation is retrieved for the center-of-mass mode of two Rydberg ions. The vibrational frequency is experimentally accessible and the amplitude of the pulse is chosen to match a specific phase accumulation as described below.

In a quantum mechanical picture, a displacement operation leads to time varying expectation values for position and momentum operators. A coherent motional state forms a circle in phase space and the area of the enclosed phase space is equal to the accumulated phase. For a state-dependent coherent state size, the accumulated phase during a full rotation is different for all basis states. Additionally, the displacement of the crystal center for basis states $|\uparrow\downarrow\rangle$ and $|\downarrow\uparrow\rangle$ leads to a linear phase accumulation depending on pulse time. Overall, each basis state can be described by a phase $\phi^{\alpha\beta} := \varphi_1^{\alpha\beta} + \varphi_2^{\alpha\beta} + \Phi_\mathrm{e}^{\alpha\beta}$, which considers excitation of both vibrational modes and the crystal center displacement. As global phases on all basis states are irrelevant, only the phase differences for varying numbers of Rydberg excitations are studied. Moreover, any multiple of $2\pi$ is indistinguishable for phase differences and modulo $2\pi$ is used to simplify phases within this section. In figure 6.2 the accumulated phase differences $\phi^{\uparrow\uparrow} - \phi^{\downarrow\downarrow}$ and $\phi^{\uparrow\uparrow} - \phi^{\uparrow\downarrow}$ are presented on the right side as a function of pulse time in green and purple, respectively. Due to the asymmetric crystal center, state $|\uparrow\downarrow\rangle$ generates a much larger phase during the displacement pulse compared to an ion crystal with identical electronic states. Thereby, the purple phase difference contains several multiples of $\pi$ within one oscillation period. In the presented figure, the pulse amplitude $f_0$ is chosen to result in a phase difference of $\pi$ between state $|\uparrow\uparrow\rangle$ with respect to states with one or zero Rydberg excitations at the pulse time $T = {}^{2\pi}/_{\omega_1^{\uparrow\uparrow}}$.

## The Controlled Phase Gate

The state-dependent phase accumulation can be used to generate laser-less entanglement of two ions, much faster than typical laser-driven entanglement operations. For a phase gate, the electronic excitation of the ion crystal remains unchanged and one of the basis states obtains a phase shift of $\pi$. Here, the ion crystal consisting of two Rydberg ions is selected as control state to highlight the huge polarizability, which enables the proposed entangling scheme. The evolution operator of an ideal controlled phase gate on the basis states $|\alpha\beta\rangle = \{|\downarrow\downarrow\rangle, |\uparrow\downarrow\rangle, |\downarrow\uparrow\rangle, |\uparrow\uparrow\rangle\}$ reads:

$$U_\mathrm{CP} = \begin{pmatrix} 1 & 0 & 0 & 0 \\ 0 & 1 & 0 & 0 \\ 0 & 0 & 1 & 0 \\ 0 & 0 & 0 & -1 \end{pmatrix} . \tag{6.81}$$

As the ideal phase gate does not involve motional excitation, any residual phonons need to be avoided. Also, finite phase differences between the basis states (apart from the $\pi$ phase shift for state $|\uparrow\uparrow\rangle$) disagree with the ideal phase gate and limit the entangling operation. For the constant displacement pulse, four parameters allow to tune the accumulated phase and residual phonons. This are the Rydberg state, the trap frequency, the pulse amplitude and the pulse duration. Principal quantum numbers are discrete and $n\mathrm{P}_{1/2}$ states of $^{40}\mathrm{Ca}^{+}$ with $n = \{36, 50, 64\}$ are considered as states with low, medium and high polarizability, respectively. Contrary, the pulse shape (amplitude and duration) as well as the trap frequency can be continuously varied. Since equations 6.78 to 6.80 allow for multiple parameter triples that result in entanglement, the investigation of phonons and phase is structured by two constraints. Firstly, the trap frequency needs to be experimentally accessible, that is in a range of 100 kHz to a few MHz. Secondly, only phase space trajectories are investigated, in which state $|\uparrow\uparrow\rangle$ encloses a full circle in phase space to reduce residual motional excitation. This fixes the duration of the pulse to $T = {}^{2\pi}/_{\omega_1^{\uparrow\uparrow}}$. For a given Rydberg state, the phase differences between basis states can be engineered by the pulse amplitude and the trap frequency. As no constraints are given for the electric field kick, the amplitude $f_0$ is chosen to yield $\phi^{\uparrow\uparrow} - \phi^{\downarrow\downarrow} = \pi$ for any trap frequency $\omega_1^{\uparrow\uparrow}$. Both kick amplitude and kick duration are directly depending on the center-of-mass motion of two ions in the Rydberg state. Finally, the trap frequency is varied to obtain a controlled phase gate. In figure 6.3a) the phase difference $\phi^{\uparrow\uparrow} - \phi^{\uparrow\downarrow}$ is shown as a function of trap field gradient $\gamma_{\mathrm{DC}}$ with dependent values for $f_0$ and $T$ as described above to find a set of parameters leading to a controlled phase gate. To avoid confusion between vibrational frequencies of different basis states the trap field gradient (c.f. equation 2.28) is utilized. Within the displayed range of field gradients the high-lying Rydberg states allow for generation of entanglement at any odd multiple of $\pi$ given by vertical dashed lines. For states with higher principal quantum number the variation of oscillation frequencies between different basis states is larger and a larger phase difference is accumulated during the displacement.

Once a triple $(f_0, \omega_1^{\uparrow\uparrow}, T)$ yielding ideal phase differences is found, the motional excitation of the ion crystal needs to be investigated. Residual phonons limit the use of state-dependent electric kicks for entanglement generation. By loosen the constraints on the parameters, the residual excitation could be reduced by using not only the first closed trajectory in phase space, but allowing the field kick to be multiple periods of the trap frequency. This reduces the required field amplitude to generate the same phase differences and leads to smaller coherent states. Similarly, smooth driving fields

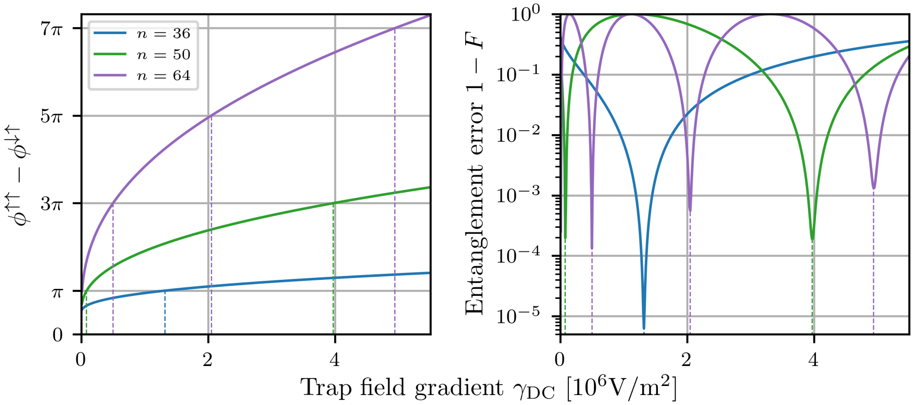

**Figure 6.3:** Left: phase difference between $|\uparrow\uparrow\rangle$ and $|\uparrow\downarrow\rangle$ for optimized electric pulse shapes as function of the trap field gradient. Odd multiples of $\pi$ yield entanglement and are marked by vertical dashed lines for each Rydberg state, where $n = 36$ is depicted in blue, $n = 50$ in green and $n = 64$ in purple. Right: resulting entanglement error $1 - F$ for the same parameters. The presented minimum for the $36\mathrm{P}_{1/2}$ Rydberg state is $1 - F = 6.3 \cdot 10^{-6}$.

might be able to reduce the residual phonon numbers.

## 6.3 Entanglement Error and Experimental Challenges

To quantify the limits of the proposed entangling gate as a function of trap field gradient and Rydberg state, the overlap integral between the state evolution of equation 6.74 with the ideal target state is studied. Therefore, a two-ion superposition state $|\Psi(0)\rangle = {}^1\!/\!_2\,[(|\downarrow\rangle + |\uparrow\rangle) \otimes (|\downarrow\rangle + |\uparrow\rangle)]$, initially prepared in the motional ground state, determines a fidelity $F$ of:

$$F = \left| \langle \Psi(0) |\, U_{\mathrm{CP}} U_{\mathrm{I}}(f_0, \omega_j^{\alpha\beta}, T)\, |\Psi(0)\rangle \right|^2 \quad . \tag{6.82}$$

Both evolution operators $U_{\mathrm{CP}}$ and $U_{\mathrm{I}}$ are diagonal and do not change the electronic state of the ion crystal. By normalization of the superposition state the fidelity ranges between $F = 1$, which depicts an ideal phase gate and $F = 0$, if the triple $(f_0, \omega_j^{\alpha\beta}, T)$ yields no overlap to the target state at all. For the discussed square electric driving field follows:

$$F = \frac{1}{16}\left|\exp\left[-\frac{\left|A_1^{\downarrow\downarrow}\right|^2}{2} + \mathrm{i}\varphi_1^{\downarrow\downarrow}\right] - \exp\left[\mathrm{i}\varphi_1^{\uparrow\uparrow}\right]\right.$$
$$\left. + 2\exp\left[-\frac{\left|A_1^{\uparrow\downarrow}\right|^2}{2} - \frac{\left|A_2^{\uparrow\downarrow}\right|^2}{2} + \mathrm{i}\left(\varphi_1^{\uparrow\downarrow} + \varphi_2^{\uparrow\downarrow} + \Phi_\mathrm{e}^{\uparrow\downarrow}\right)\right]\right|^2 \quad . \tag{6.83}$$

Each basis state contributes to the fidelity by the residual coherent state sizes and the total accumulated phase. Evaluating the absolute square allows to cancel any global phase and only phase differences between basis states are relevant. The entanglement error is defined as $1-F$ and shown on the right hand side in figure 6.3 as a function of trap field gradient. Whenever the phase differences between the basis states match the conditions for a controlled phase gate, the entanglement error is drastically reduced as highlighted by the vertical dashed lines. The parameters in figure 6.3 are not specifically chosen to minimize the entanglement error but rather introduce a systematic procedure to realize the desired phase differences. Nevertheless, the calculation shows a minimal entanglement error of $1 - F = 6.3 \cdot 10^{-6}$ for Rydberg state $36\mathrm{P}_{1/2}$ with a trap frequency of $\omega_1^{\uparrow\uparrow} = 2\pi \cdot 567\,\mathrm{kHz}$, an electric kick duration $T = 1.8\,\mu\mathrm{s}$ and an electric field amplitude of $E_\mathrm{kick} = 29\ ^\mathrm{V}/_\mathrm{m}$, which is feasible with current experimental setups.

For large principal quantum numbers or high trap field gradients, the frequency difference between high-lying electronic state and their low-lying counterpart increases. Hence, the required phase differences are more easily generated, while residual motional excitation contributes more to the entanglement error. As shown in figure 6.3, the entanglement error with respect to the minimal error of the $36\mathrm{P}_{1/2}$ state increases for larger principal quantum numbers. Also, the presented curve for $n = 64$ shows three times a low entanglement error, which increases as a function of trap field gradient. To further reduce the entanglement error by the same strategy, the pulse shape of the electric field kick needs to be adapted. Fast switching of an electric field is sensitive to the exact control of pulse time and amplitude, requiring dedicated electronics and precise knowledge of the motional frequencies for minimal residual excitation. For small variations in the pulse shape, also related to an experimental realization, a smooth electric field as e.g. a Gaussian-shaped pulse might be more stable with respect to the resulting entanglement error.

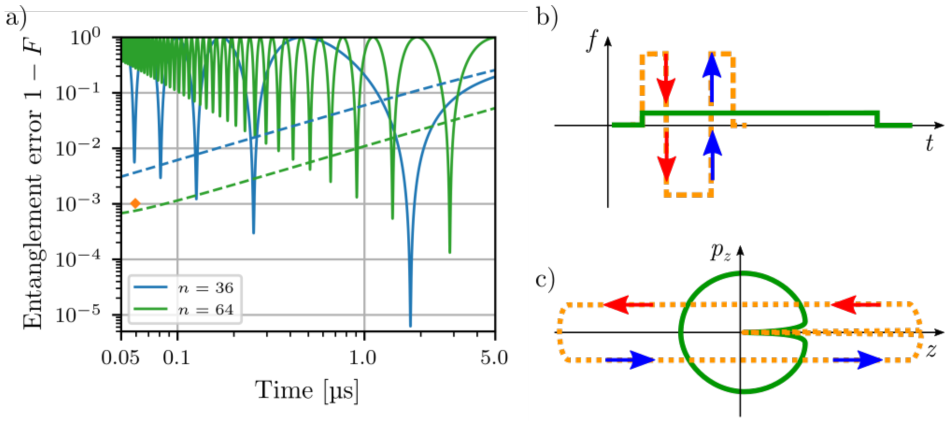

**Figure 6.4:** a) Entanglement error as a function of gate time (solid) and Rydberg state lifetime (dashed) for states $36P_{1/2}$ (blue) and $64P_{1/2}$ (green). b) And c) show the bang-bang electric field control and the trajectory in phase space given by three consecutive kicks (orange) compared to the single square electric field pulse (green). The resulting entanglement error can be reduced to reach the lifetime limit for ultra-short pulse durations as given by the orange diamond in a).

## Lifetime Limited Fidelity and Bang-Bang Control

State-dependent vibrational frequencies enable a controlled phase gate on timescales of 1 µs and show promising fidelity for feasible experimental parameters. Due to the large polarizability, the basis states are distinguishable by the number of Rydberg excitations in a two-ion crystal. Advanced state excitation schemes using sequences of STIRAP pulses [Hig17] allow for coherent population transfer of the trapped ion to Rydberg states and back, such that initial state preparation is not identified as fundamental limitation for the entanglement error. Contrary, the Rydberg state lifetime of low angular momentum states require interaction times well below one µs to overcome spontaneous decay. The lifetime of Rydberg states scales with principal quantum number $n^3$ and ranges for the investigated $nP_{1/2}$ states from $70 \cdots 400\,\mu\mathrm{s}$ [Glu13]. Hence, a single ion in the $36P_{1/2}$ state decays with 2.5% for a pulse duration of $T = 1.8\,\mu\mathrm{s}$, which does not compete with state-of-the-art fidelity [Hil21]. Choosing $64P_{1/2}$ the lifetime limited decay of a single ion reduces below 1%, but is more than one order of magnitude larger compared to the entanglement error of a gate with infinite state lifetime as shown in figure 6.4a). Here, the entanglement error without state decay is given in solid curves for $n = 36$ (blue) and $n = 64$ (green), while the additional lifetime error is indicated by dashed lines as a function of the gate duration on a log-log scale. Including the lifetime into the evaluation of entanglement error needs to account for decay of each individual ion on the three basis states with Rydberg excitation.

Intuitively, the combined entanglement error of residual phonons and state lifetime can be improved in two ways. On the one hand Rydberg states with longer lifetimes can be employed by exciting much higher principal quantum numbers or utilizing circular states with suppressed decay channels [Sig17, CM20]. On the other hand shorter gate sequences can be engineered. Ultra fast kicks might be readily employed by adapting the pulse shape of the electric kick and repeatedly displacing the ion as shown in figure 6.4b). The green line depicts the previously discussed single electric pulse and the orange dashed line excites the ion motion in a threefold way. First the ion is displaced similar to the single pulse but with much larger amplitude and afterward the electric field is inverted, which kicks the ion into the opposite direction. After an evolution time the second field pulse is switched of, such that the initial displacement is retrieved. The ion is returned to the motional ground state by designing the pulse duration of each kick. Since the accumulated phase is dependent on the displacement, the entanglement operation can be made arbitrary short for multiple kicks, eventually limited by the required electric field amplitudes. In figure 6.4c) the phase space trajectory of the two presented kick schemes is shown (not to scale), where the green line shows the evolving coherent state due to a single displacement and the orange line rather shows a rapid movement of the ion crystal within the trap. Red and blue arrows are a guide to the eye, to relate electric field displacement to the motion in phase space. The orange illustrations in b) and c) demonstrate, how multiple ultra-fast kicks on the two-ion crystal are able to generate an entanglement error $1 - F = 0.1\%$ for Rydberg state $64\mathrm{P}_{1/2}$ within just $T = 59.6$ ns as shown with the orange diamond in figure 6.4a). This kick scheme utilizes equal-strength electric field amplitudes $\{f_0', -f_0', f_0'\}$ with $E_{\mathrm{kick}} = 2060$ V/m for durations around $\{T'/4, T'/2, T'/4\}$ at a trap frequency of $\omega_z = 2\pi \cdot 1.5$ MHz. These parameters for ultra-fast entangling of two ions are not optimized with the current experimental setup in mind. Nevertheless, more complex pulse shapes extend the entanglement scheme of shuttling Rydberg ions to faster operations, which are not limited by the lifetime of accessible Rydberg states.

## Prospects of Shuttling Rydberg Ions

Note, that electric bang-bang control of single ions has been demonstrated with up to 10000 phonons and displacement pulses of sub-ns resolution [Alo16], experimental parameters that even exceed the requirements for the proposed operation. Also, coherent states were successfully excited within this thesis (c.f. 5.1). Aiming for faster operations with higher fidelity, more complex phase space trajectories of the wave packet can be explored with the additional benefit of robustness against imperfections of the driving kick waveform. A closed trajectory in phase space allows to reduce the motional state excitation to the initial value. With an external field, that extends the time in which the phase space trajectory is approximately closed, a nonperfect calibration in pulse time of the entanglement waveform can be compensated for. At the same time, this external field might reduce residual motional excitation of all contributing modes by a time-dependent pulse amplitude. In this context, optimal control theory may deliver optimized electric field waveforms [Can11, Fü14, Rac15].

For ion crystals of more than two ions, the shuttle-based entanglement scheme needs to be evaluated for more than two vibrational modes. In a linear ion crystal the oscillations are separable along axial and radial directions, such that the discussion is analogously. However, already for three ions the oscillation along the trap axis can not be described by one in-phase and one out-of-phase motion, but a third mode arises, where the central ion is out-of-phase compared to the outer two ions (c.f. section 7.1). The center of mass remains at rest for the additional oscillation and does not contribute to the phase accumulation, but residual motional excitation contributes to the entanglement error. The mode structure becomes even more complex for ion crystals, which are not arranged in a linear string but ions are off the RF null. Hence, the oscillations are not separable along the trap directions and coupling between axial and radial modes occur. This might even lead to site-dependent electric kicks and could be used to control the entanglement operation not only by the number of Rydberg excitations but also the position of the highly excited ions.

The experimental realization of shuttle-based entanglement using Rydberg ions requires the coherent control of the ion's electronic states. To coherently excite an ion to a $n\mathrm{P}_{1/2}$ state, the two-photon excitation needs to be combined with a microwave photon. The two-photon excitation experiences transition shifts due to state-dependent trap frequencies along the radial modes and residual Doppler broadening along the axial direction. Moreover, the laser linewidths of both Rydberg excitation lasers prohibit coherent state excitation at the current experimental setup, although sufficiently high laser powers are available to excite the ion within the Rydberg state lifetime. Cooling the ion crystal to the motional ground state of all modes and stabilizing the deep UV lasers to high finesse cavities allow for coherent excitation of $n\mathrm{S}_{1/2}$ Rydberg states. Application of advanced excitation schemes, as e.g. STIRAP, can enhance the state excitation. Including a microwave source into the excitation scheme, the high polarizability and long lifetimes of Rydberg $n\mathrm{P}_{1/2}$ states can be utilized.

# 7

# Counting Dark Ions: Van-der-Waals Forces between Trapped Rydberg Ions and Search for Correlated Quantum Jumps

If many ions are loaded into a linear Paul trap they form three-dimensional crystals, which shape is determined by the confinement along the trap directions. For sufficiently high radial trap frequencies, the ions form a linear string along the trap axis with interparticle distances of a few µm. Exciting Rydberg states allows to create additional interactions based on the state-dependent trap frequencies or large rotating dipole moments of microwave dressed states, where the dipole-dipole interaction depends on the interparticle distance $R_{ij}^{-3}$. The latter facilitates the Rydberg-blockade [Wil10] and fast entangling of trapped ions [Zha20]. Without additional microwave dressing, Rydberg states of ions do not exhibit a permanent dipole moment and the interaction between Rydberg ions is dominated by the Coulomb force. Nevertheless, the extension of the electronic wave packet can become orders of magnitude larger for highly excited ions compared to ions in low-lying electronic states. Two extended electronic wave functions at a given distance interact by the Van-der-Waals force, which scales by $R_{ij}^{-6}$. With experiments becoming more and more sensitive, magnetic dipole interaction between two trapped ions even in low-lying electronic states of $^{88}\mathrm{Sr}^+$ are measured at orders of mHz [Kot14]. Here, the corresponding electric Van-der-Waals force between trapped Rydberg ions is studied, where much larger energy shifts up to 100 kHz are expected [Mü08, Li13b].

Within this section, linear Coulomb crystals of three and four ions are discussed in terms of interparticle distance and coupled oscillations. To observe energy shifts which scale by the interparticle distance $R_{ij}^{-6}$, an optimal ion crystal geometry is identified with respect to the current experimental limitations. Afterward, single shot correlations for site-selective excitations of low-lying electronic states are evaluated and compared to excitation of Rydberg states. The obtained results are interpreted within the current understanding of Rydberg excitation lineshape, occupation of normal modes and long term laser stability. Finally, the required sensitivity for a quantitative measurement of Van-der-Waals interaction between Rydberg ions is estimated.

## 7.1 Coulomb Crystals Interacting with a Laser

The Hamiltonian of a single ion and two ions confined in a Paul trap are intensively discussed in section 2.1 and 6.1, respectively. Adding more ions further increases the complexity due to the all-to-all connectivity of the ions by the Coulomb interaction and the coupled harmonic motion. At low temperature the ions arrange in crystals, where the interparticle distances are determined by the interplay of Coulomb force and axial trap potential. A large ratio of both radial trap frequencies compared to the axial confinement leads to formation of linear ion strings, but also 2D and 3D crystals are possible. Especially the transition from a linear string of ions to a 2D zigzag crystal is intensively studied by varying the trap field gradients [Cam10, Ulm13], or utilizing state-dependent trap frequencies by Rydberg excitation [Li13a]. Here, excitation of Rydberg states in a linear Coulomb crystal are used to observe a variation of nearest neighbor interaction apart from the state-dependent confinement, although the large polarizability of Rydberg states manifests itself in the excitation lineshape. Correlating the site-dependent transition probabilities for Rydberg excitation allows for a discussion of Van-der-Waals interaction between Rydberg ions.

### Normal Modes and Interparticle Distance

The critical asymmetry parameter $\mathcal{A} = ({}^{\omega_z}/_{\omega_r})^2 \approx 2.53N^{-1.73}$ introduced in section 2.1 relates the ion number $N$ to axial and radial field gradients $\gamma_{\mathrm{DC}}$ and $\gamma_{\mathrm{RF}}$, respectively. For trap frequencies above the critical parameter the crystal structure changes from a linear string to a two-dimensional zigzag crystal. Here, $\omega_{z,r}$ depict the frequency of the axial and radial center-of-mass modes, which correspond to the trap frequencies of a single ion. Generally, mode frequencies and equilibrium positions of Coulomb crystals with $N > 2$ are obtained by numerical solving the force-balance conditions between all ions. Successively, the Eigenvalues and the Eigenvectors of the Hessian matrix are found. Ion crystals oriented along the RF null with $N > 3$ arrange in a non-equidistant pattern and the spacing between ions increases further away from the

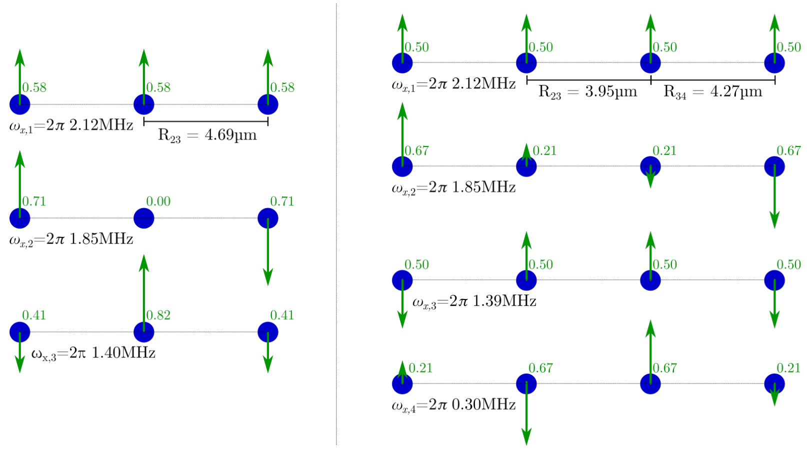
0.58
0.58
0.58
$\omega_{x,1}$=2π 2.12MHz
$R_{23}$ = 4.69µm
0.71
0.00
0.71
$\omega_{x,2}$=2π 1.85MHz
0.41
0.82
0.41
$\omega_{x,3}$=2π 1.40MHz
0.50
0.50
0.50
0.50
$\omega_{x,1}$=2π 2.12MHz
$R_{23}$ = 3.95µm
$R_{34}$ = 4.27µm
0.67
0.21
0.21
0.67
$\omega_{x,2}$=2π 1.85MHz
0.50
0.50
0.50
0.50
$\omega_{x,3}$=2π 1.39MHz
0.21
0.67
0.67
0.21
$\omega_{x,4}$=2π 0.30MHz

**Figure 7.1:** Common oscillations of a linear three-ion (left) and four-ion (right) crystal along radial direction $x$ with center-of-mass mode frequency $\omega_{x,1} = 2\pi \cdot 2.12$ MHz. Calculated vibrational frequencies and interparticle distances are given. Green arrows and green numbers indicate relative oscillation amplitude of individual ions within the respective mode (quadratically normalized).

crystal center. Motion along the trap axes are decoupled and $N$ common modes for each direction are present, in which the coupling of individual ions to the motion is site dependent. Figure 7.1 shows the common modes for three ions (left) and four ions (right), respectively, along one radial mode with center-of-mass mode frequency $\omega_{x,1} = 2\pi \cdot 2.12\,\mathrm{MHz}$ obtained by analysis of the Hessian matrix. Green arrows and green numerical values indicate the relative oscillation of the ions within the corresponding mode, where the sum of the squared values is normalized for each mode. Note, only for the center-of-mass mode all ions oscillate in-phase with the same amplitude, whereas the center of mass remains at rest for all other modes due to relative phase and amplitude differences between the ions. This is especially important for crystals with an odd number of ions, where the central ion is not moving in the mode with frequency $\omega_{x,2} = 2\pi \cdot 1.85\,\mathrm{MHz}$ as shown on the left of figure 7.1.

The oscillation frequencies and interparticle distances are related to the trap field gradients, which are determined by the applied voltages and the trap geometry. Within this thesis, the oscillation frequencies are measured either by spectroscopy or tickling the ion with an external RF field and observing the motion of the ion on the camera. For two identical ions the measured axial center-of-mass mode frequency $\omega_z$ yields an

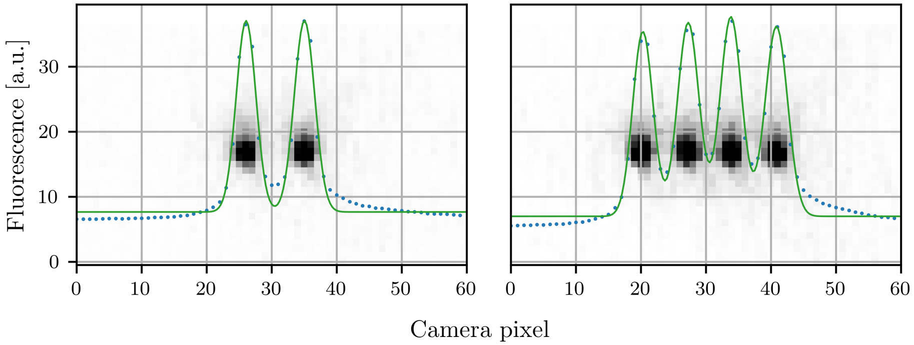

**Figure 7.2:** Fluorescence images to extract the imaging magnification of the experimental setup with a two-ion crystal at center-of-mass mode frequency $\omega_z = 2\pi \cdot 0.54$ kHz (left) and consecutive determination of interparticle distances in a four-ion string within the same trap potential (right). Blue data points are integrated fluorescence counts along columns of the presented crystal image with Gaussian fits in green.

interparticle distance (see equations 6.52 - 6.55) of

$$|Z_1 - Z_2| = \left[\frac{2\mathrm{C}}{M\omega_z^2}\right]^{\frac{1}{3}} \quad . \tag{7.84}$$

Relating the fluorescence image to the axial trap frequency allows for the calibration of the objective magnification and consecutive measurements of ion displacements or distances between multiple ions in a linear string. Two pictures of ion crystals with center-of-mass mode frequency $\omega_z = 2\pi \cdot 0.54$ kHz are investigated as presented in figure 7.2. The camera image is integrated along the vertical direction to find the fluorescence as a function of horizontal camera pixel, such that a single one-dimensional Gaussian can be fitted to each individual ion. Following equation 7.84 for the two ions on the left hand side, the achieved experimental resolution is 0.91(2) µm/pixel on an EMCCD chip with pixels of $16 \cdot 16\ \mu\mathrm{m}^2$ size, which results in a magnification of 18.1(2). Thereby, the equilibrium positions of linear ion crystals can be experimentally determined as shown in figure 7.2 for four ions on the right hand side. The inner ions are spaced by 6.15(8) µm, while the distance between the outer-most ions and their nearest neighbor is 6.55(8) µm. Within the accuracy of the experiment, the interparticle distances agree with numerical calculations of 6.08 µm and 6.57 µm, respectively [Jam98].

Van-der-Waals forces between two ions scale with the interparticle distances $R_{ij}^{-6}$ and hence require large trap frequencies to generate substantial energy shifts. The current trap geometry and voltage control allows for axial trap frequencies $\omega_z < 2\pi \cdot$

1.2 MHz yielding a distance of 5 µm in between two ions. Adding more ions to the same harmonic potential decreases the distance between the central ions but also reduces the critical anisotropy parameter to obtain linear ion strings. Although the radial trap frequencies can be independently tuned from the axial field gradient by varying the RF drive amplitude, a maximum radial trap frequency of $\omega_y < 2\pi \cdot 2.4\,\mathrm{MHz}$ was found before the trap operation became unstable. This was noticed by observing large unsystematic drifts in the optimal compensation voltages and time varying radial trap frequencies, which both could be explained by thermal heating of the trap and surrounding material due to dissipated RF power. The loading of ions in dedicated zones of the trap with successive transport requires switching of the RF amplitude. As the thermalization within timescales of ion losses by Rydberg excitation seems not possible, the radial trap frequencies are limited. Nevertheless, four ions are linearly trapped for axial frequencies up to $\omega_z < 2\pi \cdot 1.15\,\mathrm{MHz}$, but the presence of low frequency radial modes challenges ion cooling. Close to the phase transition between a 1D and 2D crystal some of the radial modes approach a vanishing frequency (c.f. $\omega_{x,4}$ in figure 7.1) and are very sensitive to low frequency noise (such as mechanical or electrical noise) on the experimental setup. Finally, axial frequencies up to $\omega_z = 2\pi \cdot 1.03\,\mathrm{MHz}$ have been chosen for the presented experiments.

## Site-Selective Rabi Frequencies in Thermal Ion Crystals

After Doppler cooling with projection onto all modes, residual phonons are thermally distributed and dependent on the mode frequency. Sideband cooling can further reduce the kinetic energy of the ions, but for a crystal consisting of four ions, twelve modes need to be individually addressed. The resulting number of laser pulses and pulse timings, however, is counteracted by a mode-dependent heating rate and prevents preparation of the motional ground state for all modes simultaneously. The radial center-of-mass mode $\omega_{x,1}$ was found to have the highest heating rate (compare section 4.3) and a high number of sideband cooling pulses is required to reduce the average phonon number below the Doppler limit. Hence, sideband cooling is employed only on this mode, while all other modes are assumed to be cooled to the Doppler limit. Residual phonons modify the coupling of a laser to the ion and lead to frequency shifts for Rydberg excitation as well as a decreased coupling strength for the quadrupole transition given by equation 2.33. For more than two ions, each ion oscillates with varying amplitude and give rise to site-dependent Lamb-Dicke factors

$$\eta_{i,j} = \sqrt{\frac{\hbar}{2M\omega_j}}\,\mathbf{k}\cdot\mathbf{e}_{i,j} \quad . \tag{7.85}$$

Here, the Lamb-Dicke factor contains a scalar product of the wavevector $\mathbf{k}$ with amplitude and direction $\mathbf{e}_{i,j}$ of ion $i$ and mode $j$. This means, that excitation of the quadrupole transition is independent of modes, which oscillate perpendicular to the laser direction. Ions at rest do not contribute. Consequently, a site-dependent Rabi frequency for the carrier transition is found by the product of Lamb-Dicke factors and phonon numbers of each mode, weighted by the phonon distributions:

$$\Omega_i = \Omega_0 \prod_{j=1}^{3N} \sum_{k=0}^{\infty} p_j^{(\mathrm{th})}(k)\left(1 - \eta_{i,j}^2 k_j\right) \quad . \tag{7.86}$$

Higher order terms of $\eta$ are not necessary for ions in low thermal states. If the angle between laser and oscillation direction is known, the site-dependent Rabi frequency can be calculated. Two experimental setups can be realized, where the laser near 729 nm is either parallel to the trap axis and addresses axial motion or perpendicular to the trap axis with 45° angle to both radial modes. Since the Rydberg excitation lineshape is strongly modified by phonons in radial modes, sideband cooling of the center-of-mass mode along $x$ is employed, such that the radial laser is used. Trap field gradients that result in center-of-mass mode frequencies of $\{\omega_x, \omega_y, \omega_z\} = 2\pi \cdot \{2.12, 2.35, 1.03\}$ MHz allow for numerical calculation of all mode frequencies for linear three- and four-ion crystals and the corresponding site-dependent oscillation direction and amplitude. For a three-ion crystal, cooled to the Doppler limit, the site-dependent Rabi frequency of the outer ions is modified to $\Omega^{(3)}_{\mathrm{outer}} = 0.97\ \Omega_0$ and for the central ion $\Omega^{(3)}_{\mathrm{inner}} = 0.96\ \Omega_0$. Similarly, four ions lead to $\Omega^{(4)}_{\mathrm{outer}} = 0.94\ \Omega_0$ and $\Omega^{(4)}_{\mathrm{inner}} = 0.70\ \Omega_0$, with much larger site dependency due to the presence of low frequency modes (e.g. $\omega_{x,4} = 2\pi\cdot 0.30$ MHz) that have high number of average phonons after Doppler cooling. By the use of amplitude modulated laser pulses, e.g. RAP pulses, the site-dependent Rabi frequency on the transition $4\mathrm{S}_{1/2} \rightarrow 3\mathrm{D}_{5/2}$ can be partially compensated for.

## 7.2 Search for Correlated Quantum Jumps

Manipulating the electronic states of all ions in a linear crystal by a global laser beam allows to investigate site-dependent excitation probabilities. Typically, the excitation

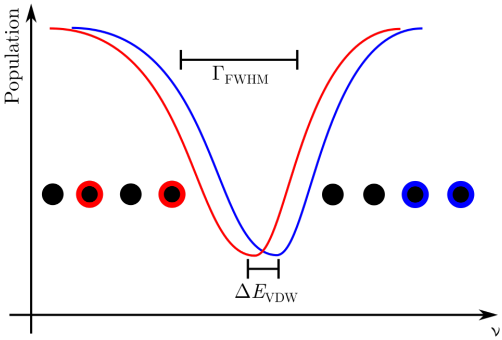

**Figure 7.3:** Sketch of the Van-der-Waals interaction, which shifts Rydberg transition frequencies. The excitation lineshape of two ions excited next to each other to Rydberg states (blue) is shifted by $\Delta E_{\text{VdW}}$ compared to the unperturbed lineshape of two ions excited apart from each other (red). The shift can be resolved as a function of the transition linewidth $\Gamma_{\text{FWHM}}$.

of ions in a crystal is uncorrelated. For highly excited states, however, the dipole-dipole interaction enables strong distance-dependent correlations, which can be used for quantum simulations [Ber17]. Ions in low-lying electronic states do not inhibit dipole moments, such that excitation of two ions is uncorrelated to their relative position within the linear crystal. This will be presented in the following and serves as a guide for measurements of Van-der-Waals interaction between Rydberg ions. Here, the extension of the electronic wave function becomes orders of magnitude larger compared to electronically low-lying states and two ions excited next to each other experience an energy shift $\Delta E_{\text{VdW}} \approx 50$ kHz. Observing the transition lineshape for Rydberg excitation of larger ion crystals, the energy shift is related to the experimentally accessible transition linewidth, as shown in section 7.4. A sketch of the assumed transition frequency shift of two ions next to each other compared to two ions apart is given in figure 7.3.

For transitions into Rydberg states the modulation of local confinement needs to be considered additionally. The measurements of Van-der-Waals forces between Rydberg ions correlates the transition energy shift to their position within the ion crystal. Once multiple Rydberg excitations are present one can compare if the corresponding excitation probabilities differ for ions, which are closer to each other compared to ions further away. Prior to investigating Van-der-Waals forces between Rydberg ions, initial measurements on the coherent state transfer $4S_{1/2,-1/2} \rightarrow 3D_{5/2,-5/2}$ are discussed in terms of site-dependent Rabi frequencies for three- and four-ion crystals.

## Experimental Realization of Correlation Measurements

The analysis of ion-ion correlations requires a discussion in the crystal basis states. The electronic ground state (all ions in state $4S_{1/2}$) of a three-ion crystal is labeled $|000\rangle$ and full population in the metastable $3D_{5/2}$ state is denoted as $|111\rangle$. A site-dependent Rabi frequency given in equation 7.86 allows to calculate excitation probabilities for each basis state, but additional effects need to be considered for an experimental verification of the final states probabilities. Initially, the ion crystal is Doppler cooled by a laser with projection onto all motional modes and the residual ion temperature is close to the Doppler limit. Sideband cooling is applied to the center-of-mass mode along $x$ to counteract unsystematic heating and reduce the occupation of $\omega_{x,1}$ below or close to the Doppler limit. Since the Zeeman sub-levels of the electronic ground state are statistically populated, frequency selective pumping on the $4S_{1/2,+1/2} \rightarrow 3D_{5/2,-3/2}$ transition with a consecutive quench near 854 nm is employed up to eight times. This initializes the ion in the $4S_{1/2,-1/2}$ ground state with probability $> 99\%$. The latter is validated for a single ion by a RAP pulse on the $4S_{1/2,+1/2} \rightarrow 3D_{5/2,-3/2}$ transition showing no notable excitation probability. Although working with multiple trapped ions, the initialization scheme is the same compared to Rydberg excitation of single ions presented in section 4.3 and 5.2, where a final RAP pulse $4S_{1/2,-1/2} \rightarrow 3D_{5/2,-5/2}$ prepares the ion in the dark state. To measure site-dependent correlations on this last coherent state transfer itself, not all ions in a crystal need to be excited and a $\pi/2$-pulse is employed instead, such that on average 50% of all ions are excited. Here, each individual realization of the experiment is studied in the crystal basis states, where the final electronic state of each ion is determined by spatially resolved fluorescence. The probability to detect a final basis state is then correlated to the interparticle distance between excited ions.

## Minimal Case Study - 3 Ions

In principle, two ions would be sufficient to probe distance-dependent Van-der-Waals forces by measuring the energy shift of a given transition and compare it to individual excitation of both ions. However, the spacing of two ions is limited by the maximal trap field gradient along the axis and at least three ions are required to find interparticle distances $R_{i,j} \approx 4\,\mu\mathrm{m}$. For $N = 3$ the ions arrange equidistant along the RF null and the external dynamics are given by nine common vibrations. Here, the central ion is especially interesting, as it remains at rest in three of these oscillations, while both outer ions oscillate. After Doppler cooling the modes are thermally occupied and

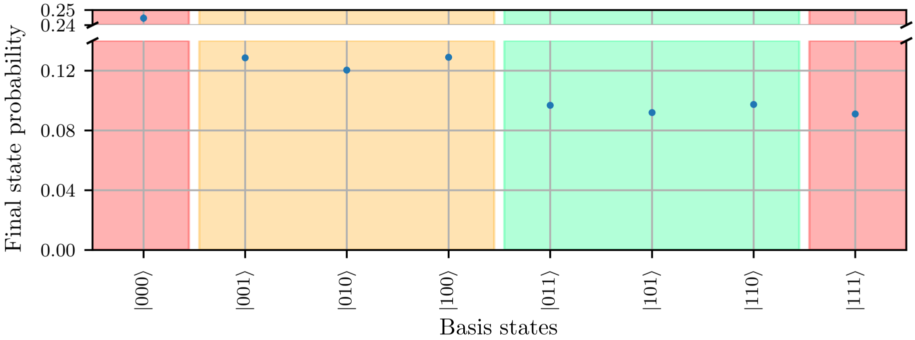

**Figure 7.4:** Final state probabilities for a three-ion crystal illuminated with a global $\pi/2$-pulse, where $|0\rangle$ ($|1\rangle$) denote ions in the $4S_{1/2}$ ($3D_{5/2}$) state. Shaded regions with different colors indicate different number of excitations from zero (left) to three (right). Due to a site-dependent Rabi frequency, the central ion experiences a different excitation probability compared to the outer two ions. Error bars are smaller than the marker size.

the site-dependent Rabi frequency can be transferred to a site-dependent excitation probability shown in figure 7.4. Here, three ions at a distance of 5.6 µm are illuminated with a $\pi/2$-pulse from the axial laser near 729 nm. In total, results from more than $7 \cdot 10^4$ experimental cycles are evaluated with respect to the crystal basis states. The states, where all ions are either dark or bright with probabilities of $p(111) = 0.091(1)$ and $p(000) = 0.244(1)$ disagree with an individual ion excitation of 50% ($p = 0.125$ for both), which indicates deviation from an optimal $\pi/2$-pulse for state excitation. On average, the ions are excited within 40% of the experimental realizations with differences depending on the position inside the crystal. Here, the excitation probability of the central ion is $p(010) = 0.120(1)$ compared to the mean of one outer ion excited $1/2[p(100) + p(001)] = 0.129(1)$ and shows site-dependent variation in the Rabi-frequency due to the presence of thermal motion. However, if a single excitation in the center of the crystal is less likely, one would expect that exciting the two outer ions $p(101) = 0.092(1)$ is more probable compared to excitation of one outer ion and the central ion, given by $1/2[p(110) + p(011)] = 0.097(1)$. This discrepancy between theory and experiment shows, that additional effects apart from site-dependent Rabi frequencies need to be considered. Since the measurements are recorded by illuminating the ion crystal with an axial beam, variation of the laser focus for the different ion positions is negligible. Also the modulation of the light-matter coupling due to micromotion should be similar for all ions as the crystal is oriented along the RF null and axial micromotion does not vary over the size of the ion crystal. Anyway, if axial micromotion would be present and symmetric around the crystal center, the outer ions would be excited less likely compared to the central ion, which disagrees with the observations. A systematic detection error of state $|010\rangle$, where both outer ions are not excited to the dark state and emit fluorescence light during the detection sequence is conjectured as the cause of this observation. The inner ion, which should be dark, might be identified as bright as well, if the fluorescence is spatially not well resolved or the ion crystal moves with respect to the imaging system during the experiment. Thereby, the ion crystal with dark ion in the center might be detected as three bright ions and the discrepancy between observation and theory can be explained. For the subsequent measurements, the detection of individual ion fluorescence is enhanced by selecting only small, non-overlapping regions for discrimination of ion bright and dark states on the camera chip as well as by a twofold increased detection time of 4 ms.

Even with special care on detection and constant laser powers, the occupation of thermal modes results in systematically differing excitation probabilities for basis states with varying spacing between the individual excitations. Especially, final states with two excited ions could be used to study Van-der-Waals forces, but the differences in the excitation probabilities are strongly dependent on laser parameters and may vary for large numbers of experimental cycles. To perform a similar amount of experimental cycles including Rydberg excitation, the measurement time will increase from a few hours (for quadrupole excitation) to several days due to ion losses, frequency drifts of Rydberg lasers and repeated electric field compensation. Keeping laser cooling and excitation rates constant over this extended time to extract the estimated Van-der-Waals energy shifts is hardly possible.

To address the challenges of the underlying systematic issues for a measurement of distance-dependent Van-der-Waals forces, the following discusses the test case of four ions excited on the $4S_{1/2} \rightarrow 3D_{5/2}$ transition.

## Minimizing Systematic Errors with Four Ions

The findings of the previous discussion holds for any odd number of ions within the crystal, as the ion at the crystal center oscillates differently than all other ions. Contrary, for even ion numbers each ion has an opposing counterpart for all modes. Also, laser intensities and residual electric field can be overlapped with the crystal center and evenly affect the excitation strengths of two ions on either side of the crystal. As a minimal example of a crystal with even number of ions and sufficiently small interparticle distances, four ions are studied with respect to its 16 basis states and 12 vibrational modes. For an axial center-of-mass mode frequency

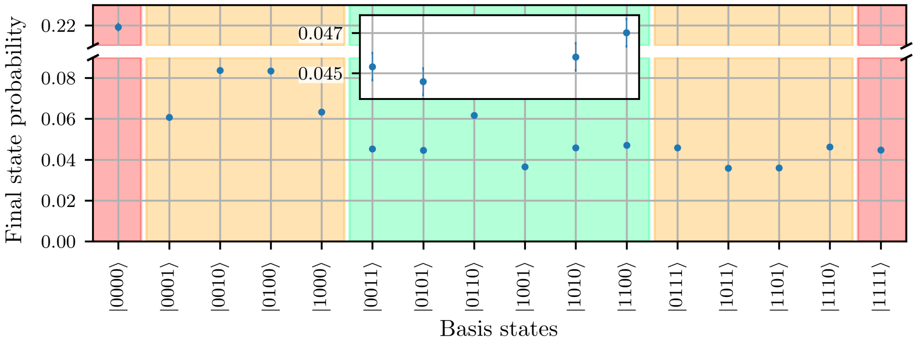

**Figure 7.5:** Site-dependent excitation of a linear four-ion crystal analogously to figure 7.4. As systematic variation of Rabi frequency and residual electric field affect the ion crystal symmetrically, there are four basis states, which allow for an extraction of position-dependent energy shifts, highlighted in the inset.

$\omega_{z,1} = 2\pi \cdot 0.78$ MHz the spacing between the inner ions is 4.7 µm and an outer ion is separated by 5.2 µm from the neighboring ion. The final state probability of a four-ion crystal after a global excitation pulse with an axial laser beam is depicted in figure 7.5, analogously to the three-ion crystal. In total, $10^5$ experimental cycles were performed with an average excitation of 45% for each individual ion into the $3D_{5/2}$ state. The site-dependent modulation of the Rabi frequency leads to an enhanced excitation of the inner ions compared to the outer ions. This is visible for final states with one, two or three ions in the dark state and agrees with a site-dependent Rabi frequency for excitation along the axis. For a single excitation within the crystal, the probability to find one of the inner ions in the dark state is $^1/_2[p(0010) + p(0100)] = 0.0836(8)$ and more than 2% larger compared to a single excitation among the outer ions, given by $^1/_2[p(1000) + p(0001)] = 0.0621(8)$. The difference between inner and outer ions for three excitations is not as pronounced, but the site-dependent Rabi frequency is observed between $^1/_2[p(1011) + p(1101)] = 0.0359(6)$ and $^1/_2[p(0111) + p(1110)] = 0.0460(7)$ with one ion remaining in the electronic ground state.

The site-dependent Rabi frequency becomes most visible for final states with exactly two dark ions, where 2.5% difference between the basis states $|0110\rangle$ and $|1001\rangle$ is measured. However, the final states with exactly two excitations, which show no substantial probability differences are the most promising for measuring distance-dependent forces. The states $|1010\rangle$, $|1100\rangle$, $|0101\rangle$ and $|0011\rangle$ each show strictly identical systematic modulations of excitation strengths as they all correspond to ion crystals with one inner and one outer ion excited. The observed excitation probabilities are $p(0011) = 0.0453(7)$, $p(0101) = 0.0446(7)$, $p(1010) = 0.0458(7)$ and $p(1100) = 0.0470(7)$, as given by the inset in figure 7.5. As long as there are no distance-dependent forces, the probability to find the ion crystal after a given laser pulse in any of these states is identical. Residual site-dependent differences might be driven by non-perfect compensation of axial and radial micromotion, but with the given number of repetitions the data agrees within their respective $3\sigma$ confidence intervals. If the presence of one ion in a given electronic state manifests itself in the energy shift for a second excitation by the Van-der-Waals force, the final basis states can be compared with respect to the distance between two excitations.

Since the Van-der-Waals interaction scales with the square of the electric polarizability it is negligible for low-lying electronic states. For large principal quantum numbers energy shifts in the order of 100 kHz may arise [Mü08, Li13b]. The realizable distances within this setup of 4.27 µm and 8.22 µm to the nearest and the next-to-nearest neighbor of an outer ion, respectively, promise a 45-fold enhanced strength of the Van-der-Waals interaction for basis states $|0011\rangle$ and $|1100\rangle$. Recording basis-state-dependent lineshapes of Rydberg transitions the center frequency including Van-der-Waals energy shifts and site-dependent variations in excitation strength can be extracted. The initial measurements on the $4S_{1/2,-1/2} \rightarrow 3D_{5/2,-5/2}$ transition yield an optimal ion number of four for the following experiments with Rydberg ions, since less ions do not allow a direct comparison between basis states.

A cold ion crystal is a prerequisite for the measurement of Van-der-Waals forces between Rydberg ions, as the Rydberg transition lineshape and the initialization pulse depend on the phonon distributions along all radial modes. To be less sensitive to site-dependent Rabi frequencies, the $3D_{5/2}$ state initialization is replaced by a RAP pulse. A statistical analysis of more than $2.6 \cdot 10^5$ experimental shots of the initialization pulse on a four-ion crystal leads to a probability of 86.0(2)% to find all four ions excited. Averaging over all ions yields an individual success rate for coherent state transfer of 96.29(8)%. Deviations from a perfect initialization might still be explained by the susceptibility of the RAP pulse on residual phonons in the vibrational modes and the long measurement time, recorded over 14 h. During this time the magnetic field and corresponding transition frequencies, laser amplitudes or cooling parameters may vary. Unlike in figure 7.5, the excitation probabilities for state initialization with RAP pulses of the outer ions is larger compared to the ones for the inner ions. This might hint to too much laser power leading to an additional decrease in excitation probability.

## 7.3 Rydberg Excitation of Linear Ion Strings

To directly measure the interaction of two highly excited ions it is necessary, that both ions populate the same electronic state for a given time. Within this section, the basis states represent a low-lying electronic state and the Rydberg state of each ion, where the $3D_{5/2}$ state of a ion is consistently referred to as $|1\rangle$ and the Rydberg state denoted as $|0\rangle$. Hence, an ion in $|1\rangle$ remains dark during state detection, while subsequent decay from the Rydberg state leads to bright ion detection for state $|0\rangle$. Aiming for strong interactions between neighboring ions, a principal quantum number of $n = 60$ compromises between Van-der-Waals forces and coupling strengths of laser beams. Coherent state excitation to an electronically high-lying level and consequent state retrieval is out of the scope of the thesis. Ideally, $\pi$-pulses would be applied on the Rydberg transition, which could not be achieved with the current laser frequency stabilization, but is aimed for, see section 4.3. Nevertheless, the lifetime of Rydberg states allows to excite multiple ions at the same time. Increasing the two-photon laser power yields sufficient state transfer for interaction times below the Rydberg state lifetime of $\tau(60\mathrm{S}) \approx 15\,\mu\mathrm{s}$ [Glu13]. If two ions are detected in the bright state after a two-photon excitation pulse with $10\,\mu\mathrm{s}$ duration, both ions were most likely excited at the same time and would have interacted. The required laser powers for short excitation times on a four-ion crystal limits utilization of higher principal quantum numbers within the current experimental setup.

When exciting Rydberg states in linear ion strings, two effects alter the transition properties. Both, the site-dependent Rabi frequency as well as the state-dependent trap frequency contribute to the transition lineshape due to the thermal distributions of phonons. Here, the laser source for state initialization is oriented along the radial direction with an expanded focus of approximately $20\,\mu\mathrm{m}$ waist to homogeneously illuminate the crystal and to cool the mode $\omega_{x,1}$ below the Doppler limit. Residual phonons in each radial oscillation mode modify the Rydberg transition lineshape, which becomes sensitive on the ion's position and motion.

### Site-Dependent Excitation Lineshape

Exciting Rydberg states in systems of more than one ion leads to broader transition lineshapes, since generally more oscillations contribute to the phonon-dependent shifts. These become negligible only for ion crystals close to the motional ground state along radial directions. Especially oscillations with low frequency are occupied by a high average number of phonons after Doppler cooling. This can lead to large shifts of

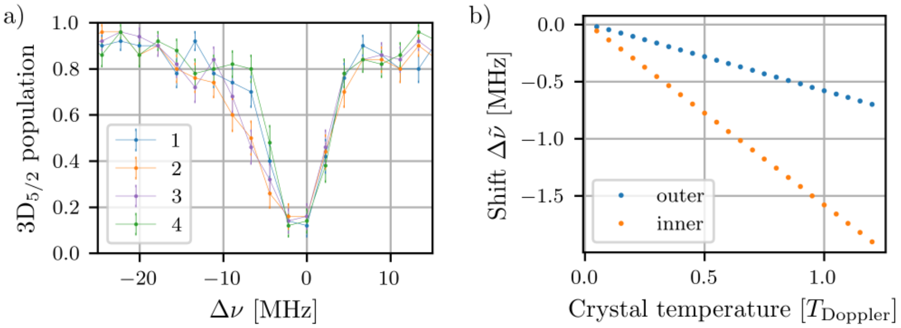

**Figure 7.6:** a) Depopulation of $3D_{5/2}$ via excitation into $55S_{1/2}$ for a four-ion crystal as a function of two-photon detuning. The inner two ions show strong phonon-dependent shifts of the transition lineshape towards negative detuning $\Delta\nu$. Numbers indicate the position of the ion inside the crystal and points are connected as a guide to the eye. b) Average phonon-dependent shift for inner and outer ions as a function of cooling temperature in units of the Doppler limit. A larger shift relates to a broadening of the transition lineshape.

the transition frequency and also results in a broadened transition lineshape due to a large variance in phonon numbers. For instance, in a four-ion crystal with center-of-mass mode frequencies $\{\omega_x, \omega_y, \omega_z\} = 2\pi \cdot \{2.12, 2.35, 1.03\}$ MHz, the lowest frequency oscillation is $\omega_{x,4} = 2\pi \cdot 0.295$ MHz (c.f. figure 7.1). After Doppler cooling the average phonon number is $\bar{k}_{x,4} = 38$, almost 4 times larger compared to all other radial modes. The inner ions of the linear string are oscillating three times stronger within this mode compared to the outer ions and hence generate a significant broader Rydberg transition lineshape for the inner ions, as depicted in figure 7.6a) for the excitation spectrum into $55S_{1/2}$ of four ions. Inner ions (2, orange and 3, purple) experience larger phonon-dependent shifts compared to the outer ions (1, blue and 4, green), despite being cooled with the same laser beam. The excitation itself is symmetric over the length of the ion crystal and the transition probabilities for both outer ions and both inner ions agree with each other. Figure 7.6b) shows calculated shifts $\Delta\tilde{\nu}$ of the transition frequency for inner (orange) and outer ions (blue) as a function of crystal temperature in units of the Doppler limit. Here, the state-dependent variation in trap frequency for each vibrational mode is multiplied by the respective average phonon number to estimate the difference in linewidth for inner and outer ions. Although this analysis allows to qualitatively explain the site-dependent broadening of the Rydberg transition, not considering the full thermal phonon distribution prohibits quantitative studies of the lineshape model, which becomes computationally heavy for the given number of phonon modes. Note, that only for very low temperatures of the ion crystal, which would require sideband cooling of all radial modes, the Rydberg transition lineshape of inner and outer ions will become indistinguishable within the experimental accuracy.

### Off-Resonant Excitation for Measurements of Rydberg-Rydberg Correlations

While the transition lineshape at positive two-photon detuning is similar for inner and outer ions of a four-ion string, for negative detuning strong variations in excitation probabilities are observed. Here, the interaction between two excitations next to each other is of interest, such that each individual experimental cycle is evaluated in the crystal basis states. A correlation of Rydberg excitations on the ion positions will be visible by an energy shift on the transition frequency. Measuring a small energy shift with statistical relevance is experimentally challenging, as many parameters are unstable over the course of a few hours. Aiming for an experimental sensitivity of relative excitation rates between basis states $< 0.1\%$, several thousand experimental cycles are necessary. A measurement of the full asymmetric lineshape should use frequency steps that resolve the expected shift. However, the frequency drifts of the fundamental laser sources for two-photon excitation prevents a short term stability longer than 20 minutes, due to temperature drifts of the optical resonator. Additionally, vibrational frequencies and electric field compensation vary on timescales of hours.

Rydberg states of ions are often affected by black body radiation induced ionization, an effect increasing with larger principal quantum numbers, such that the doubly charged $\mathrm{Ca}^{2+}$ remains trapped but is inaccessible for laser fields. Thus, exciting four ions at the same time requires frequent reloading of the trap. The EMCCD camera automatically detects the number of ions inside the trap and determines, whether ions are loaded and transferred to the experimental region. Too many ions in the experimental region are reduced to exactly four ions by fast reconfiguration of trap voltages. Alternatively, all ions are thrown out when detecting a doubly ionized Calcium atom as a dark site in the crystal. Since ion reloading requires to switch RF amplitudes between a high voltage for the experiments and a low voltage for reliable loading and transport, every loading cycle is followed by a short period of waiting to stabilize the heat load on the ion trap. Typically, a single ion loss pauses the measurement for at least half a minute before the next excitation cycle is started, but additional drift compensation measurements (e.g. transition frequencies or electric fields) are included on a regular basis. To gather sufficient statistics for a direct measurement of position-dependent excitation strengths, either a four-ion excitation spectrum is measured with several thousand count cycles or multiple spectra are recorded and overlapped later. Both methods do not account for the described drifts and would be extremely challenging to analyze.

Here, a more simplistic approach is followed, where the excitation probabilities for positive and negative detunings from the two-photon resonance are compared. If the resonance spectrum of one or two basis states is systematically shifted with respect to another basis state, but otherwise unchanged, a measurement with fixed detuning results in differences of the excitation probability between these basis states. Using the opposite detuning should invert the final state differences. For maximum sensitivity on shifts of the excitation frequency, the detuning with highest gradient of the transition lineshape on either side is optimal. Small deviations from this optimal detunings are still sufficient to measure excitation differences, but with reduced visibility. In general, the excitation differences are dependent on principal quantum number, trap field gradients and crystal temperature, such that a systematic calibration method is required to find optimal detuning on either side. Throughout the measurement, the two-photon detuning is regulated to yield $\approx 40\%$ Rydberg excitation rate of individual ions on one side of the resonance, which corresponds to half the maximal excitation strength set by appropriate laser power and detuning from the intermediate state. Fast, less sensitive scans are regularly used to identify resonance frequency and lineshape for crosschecks on ion temperature, initialization efficiency and electric field compensation. This method allows for a reliable way to compare measurements of individual experiments over various days and experimental conditions, where interparticle distance and probed Rydberg state are kept constant. A total of several ten thousand individual experimental cycles for both positive and negative detunings is presented in figure 7.7 for the basis states with two Rydberg excitations.

The most obvious change in excitation probabilities is found between states $|0110\rangle$ and $|1001\rangle$, where either both inner or both outer ions are excited to the Rydberg state. For the left side with negative detuning, ions in the center of the crystal are less likely excited with $p_{-}(0110) = 0.0340(8)$ compared to $p_{-}(1001) = 0.0548(10)$ for excitation of both outer ions. Contrary, for positive detuning this is inverted and $p_{+}(0110) = 0.0629(8)$ and $p_{+}(1001) = 0.0269(5)$ are observed. Combined, the excitation probabilities show the site-dependent modulation of transition lineshape, where thermal phonons along the radial modes shift the transition frequency. Evaluating final state probabilities without these obvious changes for different detunings could possibly show distance-dependent interactions between Rydberg ions. The average of

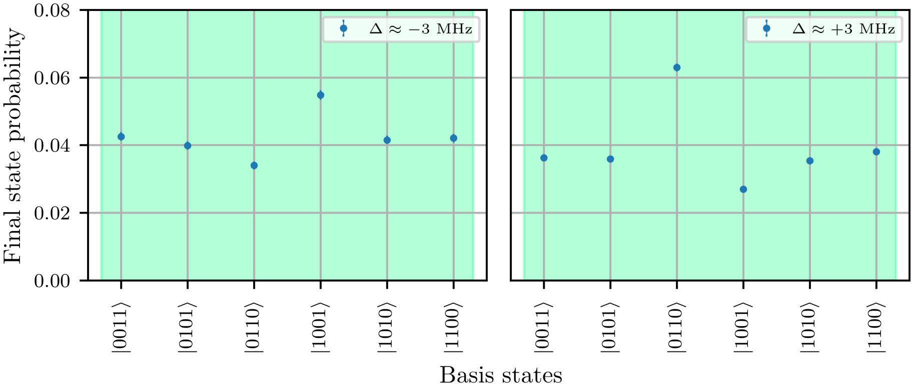

**Figure 7.7:** Probability to find two Rydberg excitations for negative (left) and positive (right) detuning from two-photon resonance as a function of four-ion basis states. For each detuning more than 50 000 experimental cycles were performed and error bars are smaller than the presented data. Apart from a systematic excitation difference between inner and outer ions no distance-dependent forces are observed within the experimental uncertainties, see text for details.

two ions excited next to each other or with one ion in between is given by

$$\begin{aligned}
{}^1\!/_2[p_-(1010) + p_-(0101)] &= 0.0407(9) \quad , \\
{}^1\!/_2[p_-(1100) + p_-(0011)] &= 0.0423(9) \quad , \\
{}^1\!/_2[p_+(1010) + p_+(0101)] &= 0.0356(6) \quad , \\
{}^1\!/_2[p_+(1100) + p_+(0011)] &= 0.0372(6) \quad .
\end{aligned}$$

For both detunings, the data agrees within their $3\sigma$ statistical uncertainty and no Van-der-Waals interaction between two Rydberg ions at a distance of 4.3 µm is observed. An estimation of excitation probabilities for an ideal experiment is given below. Note, for both detunings ions close to each other seem to be excited more likely compared to two ions apart from each other. This hints to a systematic error during the detection process as a Rydberg excitation is indirectly measured observing fluorescence. A four-ion crystal with interparticle spacing of a few µm requires good spatial resolution to identify the fluorescence counts of each individual ion and good discrimination between different basis state detections is probed by independent measurements. Shifts of the imaging objective with respect to the crystal position due to mechanical vibrations may cause the fluorescence of a bright ion to be partly observed in a neighboring pixel and might thereby falsely be counted as two bright ions next to each other.

Generally, the indirect detection of Rydberg excitations is very sensitive to readout and initialization errors.

## 7.4 Sensitivity for Measurements of Distance-Dependent Forces between Rydberg Ions

To classify the results of the presented correlation measurements of distant-dependent Rydberg excitations, all statistical and systematic error sources need to be discussed. A promising approach to mitigate initialization error was an intermediate state detection to probe the ion crystal prior to Rydberg excitation. A short detection cycle would read out the crystal state after the initialization pulse and only correctly initialized crystals are considered in later analysis of Rydberg-Rydberg correlations. This selection would only work, if all ions are correctly initialized in the dark $3D_{5/2,-5/2}$ state, as they are not interacting with the detection lasers and do not scatter photons. However, if a single ion of the crystal is not correctly initialized, the scattering process will lead to an increase in crystal temperature and thereby, heat all common modes. Typically, the laser parameters for state detection are tuned to yield maximum fluorescence with saturated laser intensity and are not suitable to reach the Doppler limit when cooling the ion. But even if no light is scattered and the ion crystal is not interacting during the detection time, heating due to electrical noise takes place and affects all crystal vibrations, such that Rydberg excitation is broadened compared to an instant excitation. As long as the experimental setup prohibits low heating rates, the initial state detection does not enhance the sensitivity for Rydberg-Rydberg correlation without introducing further site-dependent variation in excitation strengths due to residual phonons. In the future a reduction of detection time by the use of a photomultiplier can effectively reduce the state initialization error onto the level of the state detection error.

### Systematic and Statistical Uncertainties

The overall error budget is dominated by three error sources, which are state initialization, Rydberg excitation and state detection. Since the measurement reduces to bright and dark ions, all error sources are projected onto the same experimental result and independent measurements are required to estimate the magnitude of the stated error sources. For detection of the final state the fluorescence counts of individual ions are recorded by non-overlapping regions of interest on the EMCCD camera.

The detection threshold, where a given fluorescence count is attributed to a bright or dark ion, is post selected out of the raw data for every correlation measurement and crosschecked by observing the four-ion crystal with and without repump laser near 866 nm. The extraction of detection thresholds on the raw data has the advantage, that systematic errors as overspilling fluorescence counts from a neighboring region of interest or time-dependent variations of total fluorescence are suppressed, but several hundred detection cycles with each bright and dark detection events are necessary for a good discrimination. Increasing the detection time and the laser power of light near 397 nm during state detection allows to separate average fluorescence count rates for the dark and bright state, such that detection uncertainty is $< 1\%$.

For state initialization the ions are cooled close to the Doppler limit before coherent manipulation of internal and external states prepare the $|1111\rangle$ state with additional sideband cooling of the center-of-mass mode along $x$. Site-dependent modulation of the transition strength limit state preparation to 86.0(2)%, although RAP pulses are used to mitigate variations among the ion positions. The radial beam waist of $\approx 20\,\mu$m spans the whole crystal and the focus position is regularly checked by adjusting to a symmetric transition strength with respect to the crystal center. Geometry of laser and trap orientation allows for addressing of all eight radial modes, which also largely influence Rydberg transition lineshapes. Additionally, the excitation strength of the four-ion crystal is modified by axial and radial micromotion, as for the latter RF null and trap axis might not be perfectly overlapped. Similar to the measurement of the laser focus, the compensation voltages for axial and radial micromotion are set by symmetrically minimizing the residual electric fields with respect to the crystal center. Nevertheless, laser focus and residual electric fields lead to a systematic reduction of excitation strength with the laser near 729 nm for both outer ions compared to the inner ions. Statistical uncertainties in initialization efficiency stem from day to day variations in - among others - magnetic field strength, trap frequencies, laser frequencies and laser powers, such that phonon distributions differ between experiments and frequent recalibration of the given parameters is necessary. Any ion, which remains in the electronic ground state after the initialization pulse will be detected bright and reduces the visibility of actual Rydberg excitation. In terms of basis states this loss of contrast affects all ions and is symmetric with respect to the crystal center, such that relative measurements between basis states are unaffected. However, a large number of falsely identified Rydberg excitations would increase the amount of experimental cycles needed to obtain statistical significance for distance-dependent differences between basis states. To improve the initialization efficiency a better trap, which allows for larger radial mode frequencies with reduced heating rates and ground state cooling of all motional modes, or the intermediate state detection by a photomultiplier needs to be implemented.

The last dominant error source originates from the two-photon Rydberg excitation itself. Especially frequency stability of the two deep UV lasers, phonon-dependent lineshapes and off-resonant scattering from the intermediate state lead to a variation in Rydberg excitation probabilities. The initial transition $3\mathrm{D}_{5/2,-5/2} \rightarrow 5\mathrm{P}_{3/2,-3/2}$ underlies the same site-dependent variations in coupling strength compared to the quadrupole transition and leads to site-dependent scattering to the electronic ground state. This can be reduced by larger detuning of the light near 213 nm for the expense of lower excitation rates into Rydberg states. Since the laser interaction time is limited by the Rydberg state lifetime, a compromise between low off-resonant scattering and Rydberg excitation strength is necessary. Here, the probability to detect a bright ion without Rydberg excitation is kept below 5%, similar to experiments conducted with single ions. The final basis states for detecting two Rydberg excitations might be corrupted by either two off-resonantly scattered photons or by one ion decaying via $5\mathrm{P}_{3/2}$ and one ion excited to the Rydberg state, resulting in 2% false positives ($\approx 0.33\%$ per state).

Moreover, Rydberg excitation comes with uncertainties due to frequency stabilization and a phonon-dependent lineshape. The relative shift between interacting basis states and non-interacting basis states compared to the linewidth decreases with increasing ion temperature. A variation of the ion temperature modifies the transition lineshape on timescales of hours and leads to a loss in contrast for measurements of the Van-der-Waals interaction. Additionally, the laser sources for excitation of Rydberg states tend to drift several tens of MHz within a day, due to temperature fluctuations in the low finesse resonator. This leads to inconsistencies of the used one- and two-photon detunings for transitions to the $5\mathrm{P}_{3/2}$ and Rydberg state and influences rates for off-resonant scattering and total Rydberg excitation as well as fluctuations around the optimal detuning for the presented measurements. However, the laser frequency drifts are compensated for by continuously monitoring the excitation rate of individual ions and readjusting the corresponding detunings during measurements.

In total, the comparison of basis states with exactly two Rydberg excitations is impeded by various aspects and needs careful optimization of all involved parameters. For instance a measurement where two ions are detected as bright might be the result of multiple scenarios. In an ideal experiment both bright ions would coincide with two successful Rydberg excitations, but statistically one or two ions decaying via off-resonant scattering from the $5P_{3/2}$ state or one or two ions in the $4S_{1/2}$ state by imperfect initialization contribute as well. Moreover, false positive detection of a dark ion as bright is possible and limited by the imaging resolution for ion crystals with small interparticle distance. In the following, the number of experimental cycles to obtain statistically significant differences between basis states is estimated for ideal experimental conditions.

## Estimations on Rydberg-Rydberg Correlations

Within a four-ion crystal, inner and outer ions need to be treated separately in a lineshape analysis, since different coupling strength to the crystal vibrations lead to variations of excitation probabilities into Rydberg states. The Van-der-Waals interaction shifts the transition frequency of two Rydberg ions excited next to each other by $\Delta E_{\mathrm{VdW}} \approx 50 - 100\,\mathrm{kHz}$ [Li13b] and ions further apart only experience a negligible shift (c.f. figure 7.3). If all systematic shifts between the compared lineshapes are constant and only a variation of the centroid frequency is assumed, a relative measurement of excitation strengths at two different frequencies is sufficient to obtain the magnitude of the energy shift related to the Van-der-Waals interaction. By comparing transition lineshapes of basis states $|1010\rangle$ and $|1100\rangle$ with the given relative shift, optimal experimental parameters to be maximally sensitive are found and discussed in terms of the current setup and future improvements.

Initially, the transition lineshape of individual ions into the $60S_{1/2}$ Rydberg state is given by experimental parameters with a combined laser linewidth of 2 MHz and thermal motion at the Doppler limit at center-of-mass mode frequencies $\{\omega_x, \omega_y, \omega_z\} = 2\pi \cdot \{2.12, 2.35, 1.03\}$ MHz. Due to the state-dependent trap frequencies, the transition lineshape is asymmetrically broadened to a modeled linewidth of 7 MHz and differs between inner and outer ions (c.f. figure 7.6). The basis states, where exactly one outer ion and one inner ion are excited are of interest. Figure 7.8a) shows the probability to find the four-ion crystal in a state with $N$ excitations into the Rydberg state as a function of two-photon detuning. The overall excitation rate was chosen to yield 60% excitation of single ions and leads to an excitation of all four ions (orange) with 12% at resonance given by the temperature-dependent frequency shifts. Ion crystals with 2 (green) and 3 (purple) excitations are found in 35% of all detections on resonance, but differ for off-resonant excitation with larger probability to find two ions excited. The overall excitation rate to Rydberg states is chosen to yield maximal probability to detect two bright ions at the detunings for highest sensitivity regarding transition frequency shifts.

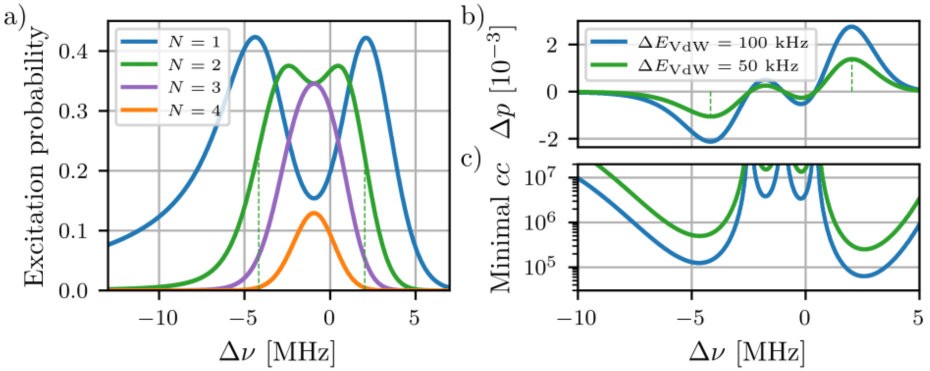

**Figure 7.8:** a) Probability to find a four-ion crystal with $N$ Rydberg excitations as a function of two-photon detuning, where the individual excitation rate of a single ion is 60%. The transition lineshape is modeled by thermal phonons at the Doppler limit and the polarizability of the $60S_{1/2}$ Rydberg state. b) Probability difference between basis states $|1010\rangle$ and $|1100\rangle$ for Van-der-Waals interaction shifts of 50 kHz (blue) and 100 kHz (green) and c) corresponding estimated number of experiments to resolve differences in excitation probabilities with statistical significance.

If two excited ions next to each other interact by the distance-dependent Van-der-Waals force, the centroid frequency of transition lineshapes for final states $|1100\rangle$ and $|0011\rangle$ compared to $|1010\rangle$ and $|0101\rangle$ would be shifted. The magnitude of excitation probabilities at a given detuning can be varied by the ratio of energy shift and excitation linewidth, that is the interparticle distance, Rydberg state and thermal phonon distributions. Here, the transition lineshapes of four-ion crystals, where one of the outer ions and one of the inner ions is excited, is shifted by $\Delta E_{\mathrm{VdW}}$ and compared to the unperturbed transition lineshape, as shown in figure 7.8b). It is assumed, that ions excited next to each other experience a varying excitation probability given by

$$\Delta p = \frac{1}{2}\left[p(1100) + p(0011)\right] - \frac{1}{2}\left[p(1010) + p(0101)\right] \quad . \tag{7.87}$$

For the modeled lineshape of two Rydberg excitations within the crystal, one finds largest probability differences (marked by green dashed lines) and thereby optimal detunings of $\Delta^- = -4.2\,\mathrm{MHz}$ and $\Delta^+ = 2.0\,\mathrm{MHz}$ on the lower and higher frequency side of the resonance, respectively. Note, the detuning for resolving the largest probability difference is not depending on the energy shift, but rather on the total linewidth and excitation strength of the Rydberg transition. For a minimal frequency shift of $\Delta E_{\mathrm{VdW}} = 50\,\mathrm{kHz}$, the modeled excitation probabilities for the relevant final states are given by:

$$
\begin{aligned}
{}^1\!/_2[p_-(1010) + p_-(0101)] &= 0.0393 \quad , \\
{}^1\!/_2[p_-(1100) + p_-(0011)] &= 0.0404 \quad , \\
{}^1\!/_2[p_+(1010) + p_+(0101)] &= 0.0370 \quad , \\
{}^1\!/_2[p_+(1100) + p_+(0011)] &= 0.0356 \quad .
\end{aligned}
$$

In general, the probabilities for optimal detunings on either side differ due to the asymmetric lineshape in the presence of thermal phonons and the probability to excite Rydberg states is larger for negative detuning. A shift in the excitation energy by Van-der-Waals interaction enhances the probability difference between positive and negative frequency detunings, such that relative measurements of the excitation probabilities allow for a more precise measurement. Since the Rydberg excitation of individual ions is projected onto bright and dark states, the statistical error on the measured probabilities follows a ${}^1\!/\sqrt{cc}$ dependency, where $cc$ is the number of individual measurements (count cycles). To observe a statistical significant difference in final state probabilities, the uncertainty needs to be smaller than half the expected probability difference and the minimal number of individual measurements can be estimated, as shown in figure 7.8c). For the current experimental setup with excitation linewidths of 7 MHz, at least $cc^+ = 7.5 \cdot 10^4$ measurements are necessary at positive detuning and almost twice as much for negative detuning $cc^- = 1.4 \cdot 10^5$ to resolve interaction shifts of 100 kHz. Note, that slightly less count cycles are required for larger detunings on either side, as the uncertainty for the excitation probability decreases with the square root of the probability itself. Nevertheless, performing the experiment at parameters leading to largest probability differences is crucial, as systematic uncertainties (detection, state preparation or scattering from the intermediate state) lead to a loss of contrast, which is constant and less crucial for larger excitation probabilities at the optimal detunings. Unfortunately, the frequency stability of the two-photon excitation laser sources seems to be insufficient to reliably measure final state probabilities at the desired detunings and the experimental setup needs to be improved for extraction of Van-der-Waals interaction strengths.

Although the interaction of neighboring Rydberg ions scales with the principal quantum number and the interparticle distance, the limiting factor for observation of Van-der-Waals interaction is the linewidth of Rydberg transitions, which can be reduced in two ways: First, the ion crystal needs to be cooled to the motional ground state to reduce phonon-dependent shifts of the transition frequency as well as residual Doppler broadening along the direction of both excitation lasers. Secondly, the linewidth of the deep UV laser source needs to be improved, eventually below the natural linewidth of the Rydberg state. Since the current ion trap geometry and misalignment during fabrication limit the use of larger RF amplitudes for higher radial confinement, the heating rate along the center-of-mass motion $\omega_{x,1}$ prohibits effective motional ground state preparation. However, exchanging the ion trap to achieve motional ground state cooling of all radial oscillations would reduce the Rydberg transition linewidth to 2.5 MHz with the current low finesse resonator for fundamental Rydberg excitation laser sources. At this linewidth, the minimal number of count cycles to resolve a frequency shift of $\Delta E_{\mathrm{VdW}} = 100$ kHz would be $cc^{+} = 1.7 \cdot 10^{4}$, which seams feasible with respect to the experimental stability. Further, a reduction of the laser linewidth to a few kHz reduces the transition linewidth to Doppler limited 1 MHz and requires $cc^{+} = 2.5 \cdot 10^{3}$ experimental cycles to resolve Van-der-Waals energy shifts. With full motional ground state cooling and a reduced laser linewidth only $cc^{+} \approx 60$ count cycles are required to observe statistically different excitation probabilities. Hence, it would be possible to resolve the full transition lineshape and extract the Van-der-Waals energy shift out of the center frequency for different crystal states. For an energy shift of $\Delta E_{\mathrm{VdW}} = 50$ kHz approximately four times the number of individual measurements are required compared to the given values.

Finally, the distance-dependent force between two trapped Rydberg ions changes its nature by introducing rotating dipole moments via microwave dressed Rydberg states. The dipole-dipole interaction scales with the interparticle distance $R_{ij}^{-3}$, which becomes orders of magnitude larger compared to the Van-der-Waals interaction and can be used for quantum computation and simulation [Mü08, Li13b, Zha20]. Including microwave transitions into the excitation scheme to probe Van-der-Waals forces allows to tune the interaction strength and explore the crossover of two different scaling laws with interparticle distance.

# 8

# Outlook

This thesis introduces trapped Rydberg ions as a platform for quantum computing and sensing, where either interaction between Rydberg states of ions and the electric field, or interactions between neighboring Rydberg ions are studied. Trapped within the harmonic potential of a Paul trap, ions are coherently manipulated by optical fields and excited by a resonant two-photon process into states with high principal quantum number. Thereby, the electronic wave function extends much further from the ionic core compared to the electronic ground states, resulting in a large polarizability. A polarizable ion, that probes the oscillating trap field, obtains a state-dependent trap frequency. Any motional occupation modifies the Rydberg state energy and can be probed by observing the spectral lineshape of the two-photon excitation.

## Conclusion

After introducing the theoretical foundations and the experimental setup, the two-photon excitation of single $^{40}\mathrm{Ca}^+$ ions to Rydberg states with principal quantum numbers $n \in [38, 65]$ was presented and the lineshape of Rydberg excitation evaluated in terms of laser linewidth and ion temperature. Specifically, the understanding of lineshape altering effects as phonon distributions and quadratic Stark shifts allowed to extract the principal quantum number scaling of the depopulation rate, a combined measure of transition dipole moment, radiative lifetime and polarizability driven broadening. The introduced model for transition lineshapes was further used to determine the polarizability of Rydberg states by two-photon excitation of strongly oscillating ions. Here, the ion was radially sideband cooled before an external electric field excites the harmonic oscillator into a coherent motional state with large average phonon number, which led to significant shifts of the transition frequency for Rydberg excitation. Probing the polarizability for different principal quantum numbers $n = 49, 53, 57$ showed good agreement with literature values.

State-dependent trap frequencies, however, enable laser-less entangling of two ions by ultra fast electric pulses exciting the center-of-mass motion of the ion crystal. Thereby, a phase accumulation dependent on the number of Rydberg excitations can be utilized to generate a differential phase between the two-ion basis states with almost negligible residual motional excitation; all with accessible experimental parameters. The achievable fidelity is limited by a deviation from the motional ground state after the entanglement operation, but even unsophisticated electric square pulses allow for entanglement errors below the error arising from lifetime limited state decay. With small variations of the pulse sequence and three consecutive kicks on the ion crystal, ultra-fast entangling gates with fidelity $F = 99.9\%$ and total duration $T = 60$ ns are possible.

Without any displacement field, Rydberg ions interact with each other by distance-dependent Van-der-Waals forces, which were probed with four ions in a linear string along the trap axis. Thermal motion of the crystal resulted in a variation of Rabi frequencies for different ion sites, such that initialization and excitation probabilities were altered with respect to a single ion. Combined with the phonon-dependent transition lineshapes, inner and outer ions experienced different frequency shifts and restricted the analysis of excitation probabilities to only four basis states, in which exactly one inner and one outer ion were excited to the Rydberg state. However, to resolve the expected Van-der-Waals energy shifts with the presented experimental setup, a total number of measurements around $10^5$ would have been necessary and impeded by the time and stability requirements of such an experiment.

## Outlook

In future, a single trapped Rydberg ion can make an efficient sensor of electric fields with spatial resolution, if the ion is shuttled within a segmented ion trap. Using multiple ions can enhance the sensitivity even further, as shown for ions in low-lying electronic states [Rus17]. Systematic uncertainties will be minimized by relative measurements between two Rydberg ions at different trap positions and entangling two ions at the central trap segment with consecutive splitting and shuttling will allow to probe the electric field at a distant location. A broad application of Rydberg ions for electric field sensing requires the ion to be shuttled from one trap to another. This is not yet shown, such that the sensing applications are limited to the trap volume. The state-dependent trap frequencies and their effects on larger ion crystals, however, can be employed to study fundamental physics as well as promise application of Rydberg ions for scalable quantum computing [Li12, Li13a].

Depending on the angular momentum of the Rydberg state and, thereby, the sign of the polarizability, the state-dependent trap frequencies become larger (positive sign) or smaller (negative sign) for highly excited ions compared to the low-lying electronic state. Hence, ion crystals of more than two ions might rearrange in shape, if the ratio of axial to radial trap frequencies cross the critical asymmetry parameter $\mathcal{A}$ for the number of ions. Exciting the central ion out of three ions in a zigzag configuration to a $n\mathrm{P}_{1/2}$ state with positive polarizability enables the crystal to undergo a phase transition into a linear crystal for the duration of the Rydberg state lifetime [Li12]. Using negative polarizability and probing the phase transition from linear to zigzag is technically more challenging, since the zigzag crystal does not overlap with the RF null and second order Stark shifts need to be considered for Rydberg excitation. Direct observation of the crystal shape by imaging with the current camera is not possible as the lifetime of the accessible Rydberg states is typically below 100 µs and fluorescence detection lasts several ms. Moreover, the camera would require a high spatial resolution to detect ions off the RF null. To overcome these issues an intensified CCD camera will be implemented, which allows to gate and to accumulate ultra-short exposure times down to 2 ns with reduced pixel size compared to the current EMCCD camera. Thereby, the experimental sequence can be split into detections shorter than the Rydberg state lifetime with laser pulses for cooling, initialization and excitation in between. The on-chip accumulation of recorded fluorescence allows to mitigate read-out noise and to resolve the ion's position accurately.

Similarly, larger ion crystals may undergo phase transitions within one, two and three dimensional crystals, where defect formation is intensively studied in terms of the Kibble-Zurek scaling law [Ulm13, Par15]. Here, the control voltages of the ion trap are varied to introduce a phase transition from an initial linear string of ions and the final crystal structure is observed. Rydberg excitation of a few ions within the crystal can lead to much faster reorganization of the crystal [Kee19]. Moreover, even without structural changes to the ion crystal, Rydberg excitation of long ion strings offers scalability for quantum computing as vibrational modes can be engineered [Li13a]. Ions trapped within a single harmonic potential oscillate together, where the number of modes equals three times the number of ions. For larger crystals the mode spacing becomes too small to externally address vibrational modes and entanglement operations relying on the common motion of the ions become impractical. High-lying electronic states at dedicated positions in the linear string of ions decouple the sub-crystal between two Rydberg ions and allow for laser driven gates within the individually trapped sub-crystal.

Enabling quantum computing with Rydberg ions, that utilize either the proposed laser-less entangling gate or the interaction between Rydberg ion and trap field for traditional laser-driven gates, requires high control of internal and external degrees of freedom of all trapped ions. The heating rates of the current ion trap effectively limit the number of ions for Rydberg excitation to only one, since sideband cooling requires many laser pulses, yet does not reach the motional ground state for motion along $x$.

Along the improvements on the existing apparatus, installation of a new microfabricated trap with 200 µm wide segments and an ion to electrode distance of 335 µm should allow for more control of the trap potentials and increased radial mode frequencies to reduce the heating rates. Also, the small segments enable fine tuning of the axial trap frequency for transport, split and merge operations. Thereby, laser excitation can be performed within reconfigurable ion crystals and may generate non-local entanglement. High radial trap frequencies in combination with flexible axial trap frequencies allow for the formation of long linear ion strings to measure distance-dependent forces with smaller interparticle distance as well as with improved accuracy. The trap will provide optical access along the trap direction for the deep UV lasers and radially for collection of fluorescence light analogously to the current setup. Further improvements to the trap and vacuum setup may include the application of a flow-cryostat to reach environment temperatures $< 10$ K. Thereby, the electronic noise will be reduced. Also the background pressure inside the vacuum chamber should benefit from the cryogenic environment. Much more important, however, will be the reduction of blackbody induced ionization events of Rydberg ions, leading to longer lifetimes of Rydberg states and better stability of Rydberg ions within the Paul trap.

A high finesse cavity with $\mathcal{F} > 10^6$ allows for linewidths $\approx 1\,\text{kHz}$ for both fundamental infrared laser sources, as given in section 3.2. Thereby, a combined deep UV laser linewidth below 10 kHz after frequency quadrupling can be achieved. This laser setup enables coherent excitation of Rydberg states, a requirement for application in quantum computation and simulation. Moreover, stabilizing the laser frequencies within the natural linewidth of the Rydberg state enhances the coupling to the Rydberg state and might lead to ultra-fast excitation of the electronic state on timescales much shorter than µs. As the two-photon process relies on resonant coupling to the intermediate $5\mathrm{P}_{3/2}$ state, the excitation of Rydberg ions can be further optimized by application of stimulated rapid adiabatic passage to mitigate off-resonant scattering [Ber19]. Here, the modulation of both deep UV AOMs in frequency and amplitude prevents a population transfer to the $5\mathrm{P}_{3/2}$ state, which would decay to the electronic ground state and consequently lose all quantum information.

Finally, transitions between neighboring Rydberg states can be employed by resonant microwave fields, to generate rotating dipole moments of the trapped Rydberg ions [Li13b]. The microwave dressing has two main applications. Firstly, the polarizability of the final state might be engineered by, for example, dressing of a positive polarizability state with states of negative polarizability. Hence, a Rydberg ion with zero polarizability can be obtained, which does not show state-dependent trap frequencies and does not require motional ground state cooling for coherent Rydberg excitation [Pok20]. For typical entanglement operations in trapped ions, however, sequences consists of multiple laser transitions, which all depend on the phonon distribution, such that ions close to the motional ground state are desired. A second use of microwave dressing is the long range dipole-dipole interaction, which two dressed Rydberg ions experience and which can be used for generating entanglement at operation speeds below 1 µs [Zha20]. Since this interaction does not rely on the coupled motion of ions and the operation time is given by the power of the driving field, further improvements on the gate duration are possible and microwave dressed Rydberg states extend the possibilities for fast, tunable quantum gates. Within the current setup a first microwave transition between the $49S_{1/2} \rightarrow 49P_{1/2}$ Rydberg states was observed and the method for extraction of polarizability by coherent motional state excitation was applied. Although first signatures of varying polarizability for dressed states with different amount of $49P_{1/2}$-state admixture are visible, a detailed and more accurate data analysis is required to confirm a systematic polarizability tuning within this setup.

# List of Figures

1.1 Schematic length scale of Rydberg atoms compared to the electronic ground state . . . . 4

2.1 Radial electric field to trap a single Ion . . . . 8
2.2 Structural phase transition by Rydberg excitation . . . . 21
2.3 Mode shaping with Rydberg excitation . . . . 22
2.4 Rabi oscillations on carrier and sideband transitions . . . . 25

3.1 Segmented ion trap . . . . 31
3.2 The vacuum vessel with relevant electrical connections . . . . 33
3.3 Level scheme of $^{40}\mathrm{Ca}^+$. . . . . 34
3.4 Laser setup at the ion trap. . . . . 35
3.5 Characterization of the high finesse cavity . . . . 40

4.1 Stabilization of external magnetic fields . . . . 45
4.2 Excitation probability of a radial motional sideband as a function of time for varying RF drive amplitude . . . . 47
4.3 Compensation of electric fields along axial and radial direction . . . . 49
4.4 Excitation spectra of the intermediate $5\mathrm{P}_{3/2}$ state . . . . 52
4.5 Rydberg excitation spectrum of $55\mathrm{S}_{1/2}$ . . . . 54
4.6 Schematic view of motion-dependent Rydberg excitation . . . . 56
4.7 Rydberg state-dependent excitation linewidth . . . . 58
4.8 Depopulation rate as function of principal quantum number . . . . 60
4.9 Rydberg excitation of a sub-Doppler cooled ion . . . . 64
4.10 Rydberg excitation within the state's lifetime . . . . 65

5.1 Phonon distribuitions . . . . 70
5.2 Charcterization of coherent states by probing the motional excitation . 72
5.3 Rydberg spectra of an ion in different coherent motional states . . . . 75
5.4 Rydberg state polarizability and comparison to theory . . . . 76

6.1 Scheme for a shuttle-based state-dependent phase accumulation. . . . 81
6.2 Average phonon numbers and phase differences as a function of kick duration . . . . 89
6.3 Phase accumulation and entanglement error for different Rydberg states 92

6.4 Lifetime limited fidelity and ultra-fast phase accumulation by three consecutive kicks. . . . . . . . . . . . . . . . . . . . . . . . . . . . 94

7.1 Normal modes of three- and four-ion crystals . . . . . . . . . . . . . . . 99
7.2 Ion crystal imaging and calibration of interparticle distance . . . . . . 100
7.3 Sketch of the Van-der-Waals interaction, which shifts Rydberg transition frequencies . . . . . . . . . . . . . . . . . . . . . . . . . . . . 103
7.4 Correlation between low-lying electronic states in a three-ion crystal . 105
7.5 Correlation between low-lying electronic states in a four-ion crystal . . 107
7.6 Rydberg spectroscopy of a four-ion crystal . . . . . . . . . . . . . . . . 110
7.7 Site-dependent Rydberg excitation in a linear four-ion crystal . . . . . 113
7.8 Estimation of sensitivity for four-ion Van-der-Waals interactions . . . 118

# Bibliography

[Alo16] J. Alonso, F. M. Leupold, Z. U. Solèr, M. Fadel, M. Marinelli, B. C. Keitch, V. Negnevitsky, and J. P. Home, *Generation of large coherent states by bang–bang control of a trapped-ion oscillator*, Nature Communications **7** (2016).

[And21] J. Andrijauskas, J. Vogel, A. Mokhberi, and F. Schmidt-Kaler, *Rydberg Series Excitation of a Single Trapped $^{40}Ca^{+}$ Ion for Precision Measurements and Principal Quantum Number Scalings*, Physical Review Letters **127**, 203001 (2021).

[Bac16] P. Bachor, T. Feldker, J. Walz, and F. Schmidt-Kaler, *Addressing single trapped ions for Rydberg quantum logic*, Journal of Physics B: Atomic, Molecular and Optical Physics **49**, 154004 (2016).

[Bal16] C. Ballance, T. Harty, N. Linke, M. Sepiol, and D. Lucas, *High-Fidelity Quantum Logic Gates Using Trapped-Ion Hyperfine Qubits*, Physical Review Letters **117**, 060504 (2016).

[Ben08] J. Benhelm, G. Kirchmair, C. F. Roos, and R. Blatt, *Experimental quantum-information processing with $^{43}Ca^{+}$ ions*, Physical Review A **77**, 062306 (2008).

[Ber98] D. J. Berkeland, J. D. Miller, J. C. Bergquist, W. M. Itano, and D. J. Wineland, *Minimization of ion micromotion in a Paul trap*, Journal of Applied Physics **83**, 5025 (1998).

[Ber17] H. Bernien, S. Schwartz, A. Keesling, H. Levine, A. Omran, H. Pichler, S. Choi, A. S. Zibrov, M. Endres, M. Greiner, V. Vuletić, and M. D. Lukin, *Probing many-body dynamics on a 51-atom quantum simulator*, Nature **551**, 579 (2017).

[Ber19] K. Bergmann, H.-C. Nägerl, C. Panda, G. Gabrielse, E. Miloglyadov, M. Quack, G. Seyfang, G. Wichmann, S. Ospelkaus, A. Kuhn, S. Longhi, A. Szameit, P. Pirro, B. Hillebrands, X.-F. Zhu, J. Zhu, M. Drewsen, W. K. Hensinger, S. Weidt, T. Halfmann, H.-L. Wang, G. S. Paraoanu, N. V. Vitanov, J. Mompart, T. Busch, T. J. Barnum, D. D. Grimes, R. W. Field, M. G. Raizen, E. Narevicius, M. Auzinsh, D. Budker, A. Pálffy, and C. H. Keitel, *Roadmap on STIRAP applications*, Journal of Physics B: Atomic, Molecular and Optical Physics **52**, 202001 (2019).

[Bla10] S. Blanes, F. Casas, J. A. Oteo, and J. Ros, *A pedagogical approach to the Magnus expansion*, European Journal of Physics **31**, 907 (2010).

[Bow12] R. Bowler, J. Gaebler, Y. Lin, T. R. Tan, D. Hanneke, J. D. Jost, J. P. Home, D. Leibfried, and D. J. Wineland, *Coherent Diabatic Ion Transport and Separation in a Multizone Trap Array*, Physical Review Letters **109**, 080502 (2012).

[Bro20] A. Browaeys and T. Lahaye, *Many-body physics with individually controlled Rydberg atoms*, Nature Physics **16**, 132 (2020).

[Cam10] A. del Campo, G. D. Chiara, G. Morigi, M. B. Plenio, and A. Retzker, *Structural Defects in Ion Chains by Quenching the External Potential: The Inhomogeneous Kibble-Zurek Mechanism*, Physical Review Letters **105**, 075701 (2010).

[Can11] T. Caneva, T. Calarco, and S. Montangero, *Chopped random-basis quantum optimization*, Physical Review A **84**, 022326 (2011).

[Cir00] J. I. Cirac and P. Zoller, *A scalable quantum computer with ions in an array of microtraps*, Nature **404**, 579 (2000).

[CM20] T. Cantat-Moltrecht, R. Cortiñas, B. Ravon, P. Méhaignerie, S. Haroche, J. M. Raimond, M. Favier, M. Brune, and C. Sayrin, *Long-lived circular Rydberg states of laser-cooled rubidium atoms in a cryostat*, Physical Review Research **2**, 022032 (2020).

[Coo85] R. J. Cook, D. G. Shankland, and A. L. Wells, *Quantum theory of particle motion in a rapidly oscillating field*, Physical Review A **31**, 564 (1985).

[Dal89] J. Dalibard and C. Cohen-Tannoudji, *Laser cooling below the Doppler limit by polarization gradients: simple theoretical models*, Journal of the Optical Society of America B **6**, 2023 (1989).

[Die89] F. Diedrich, J. C. Bergquist, W. M. Itano, and D. J. Wineland, *Laser Cooling to the Zero-Point Energy of Motion*, Physical Review Letters **62**, 403 (1989).

[Dje91] M. T. Djerad, *Atomic parameters for transitions involving Rydberg states of singly ionized alkaline earths*, Journal de Physique II **1**, 1 (1991).

[Dre83] R. W. P. Drever, J. L. Hall, F. V. Kowalski, J. Hough, G. M. Ford, A. J. Munley, and H. Ward, *Laser phase and frequency stabilization using an optical resonator*, Applied Physics B **31**, 97 (1983).

[Esc03] J. Eschner, G. Morigi, F. Schmidt-Kaler, and R. Blatt, *Laser cooling of trapped ions*, Journal of the Optical Society of America B **20**, 1003 (2003).

[Fac16] A. Facon, E.-K. Dietsche, D. Grosso, S. Haroche, J.-M. Raimond, M. Brune, and S. Gleyzes, *A sensitive electrometer based on a Rydberg atom in a Schrödinger-cat state*, Nature **535**, 262 (2016).

[Fan15] H. Fan, S. Kumar, J. Sedlacek, H. Kübler, S. Karimkashi, and J. P. Shaffer, *Atom based RF electric field sensing*, Journal of Physics B: Atomic, Molecular and Optical Physics **48**, 202001 (2015).

[Fel15] T. Feldker, P. Bachor, M. Stappel, D. Kolbe, R. Gerritsma, J. Walz, and F. Schmidt-Kaler, *Rydberg Excitation of a Single Trapped Ion*, Physical Review Letters **115**, 173001 (2015).

[Fel16] T. Feldker, *Rydberg Excitations of Trapped Ions*, Ph.D. thesis, Johannes Gutenberg-Universität Mainz (2016).

[Fil21] J. P. Filling, *Aktive 3-Achsen Stabilisierung des magnetischen Feldes zur Verbesserung der Spektroskopie an Rydberg-Ionen*, Bachelor's thesis, Johannes Gutenberg-Universität Mainz (2021).

[Fis08] S. Fishman, G. D. Chiara, T. Calarco, and G. Morigi, *Structural phase transitions in low-dimensional ion crystals*, Physical Review B **77**, 064111 (2008).

[Fle05] M. Fleischhauer, A. Imamoglu, and J. P. Marangos, *Electromagnetically induced transparency: Optics in coherent media*, Reviews of Modern Physics **77**, 633 (2005).

[Fü14] H. A. Fürst, M. H. Goerz, U. G. Poschinger, M. Murphy, S. Montangero, T. Calarco, F. Schmidt-Kaler, K. Singer, and C. P. Koch, *Controlling the transport of an ion: classical and quantum mechanical solutions*, New Journal of Physics **16**, 075007 (2014).

[Gaë09] A. Gaëtan, Y. Miroshnychenko, T. Wilk, A. Chotia, M. Viteau, D. Comparat, P. Pillet, A. Browaeys, and P. Grangier, *Observation of collective excitation of two individual atoms in the Rydberg blockade regime*, Nature Physics **5**, 115 (2009).

[Gae16] J. Gaebler, T. Tan, Y. Lin, Y. Wan, R. Bowler, A. Keith, S. Glancy, K. Coakley, E. Knill, D. Leibfried, and D. Wineland, *High-Fidelity Universal Gate Set for* $^9Be^+$ *Ion Qubits*, Physical Review Letters **117**, 060505 (2016).

[Gal88] T. F. Gallagher, *Rydberg atoms*, Reports on Progress in Physics **51**, 143 (1988).

[Gal94] T. F. Gallagher, *Rydberg Atoms*, Cambridge University Press, 1994.

[Gal20] G. Galzerano, E. Suerra, D. Giannotti, F. Canella, E. Vicentini, and S. Cialdi, *Accurate Measurement of Optical Resonator Finesse*, IEEE Transactions on Instrumentation and Measurement **69**, 9119 (2020).

[Gam20] F. M. Gambetta, C. Zhang, M. Hennrich, I. Lesanovsky, and W. Li, *Long-Range Multibody Interactions and Three-Body Antiblockade in a Trapped Rydberg Ion Chain*, Physical Review Letters **125**, 133602 (2020).

[Glu13] I. L. Glukhov, E. A. Nikitina, and V. D. Ovsiannikov, *Lifetimes of Rydberg states in ions of the group II elements*, Optics and Spectroscopy **115**, 9 (2013).

[GR03] J. J. García-Ripoll, P. Zoller, and J. I. Cirac, *Speed Optimized Two-Qubit Gates with Laser Coherent Control Techniques for Ion Trap Quantum Computing*, Physical Review Letters **91**, 157901 (2003).

[Het15] M. Hettrich, T. Ruster, H. Kaufmann, C. Roos, C. Schmiegelow, F. Schmidt-Kaler, and U. Poschinger, *Measurement of Dipole Matrix Elements with a Single Trapped Ion*, Physical Review Letters **115**, 143003 (2015).

[Hig17] G. Higgins, W. Li, F. Pokorny, C. Zhang, F. Kress, C. Maier, J. Haag, Q. Bodart, I. Lesanovsky, and M. Hennrich, *Single Strontium Rydberg Ion Confined in a Paul Trap*, Physical Review X **7**, 021038 (2017).

[Hig19] G. Higgins, F. Pokorny, C. Zhang, and M. Hennrich, *Highly Polarizable Rydberg Ion in a Paul Trap*, Physical Review Letters **123**, 153602 (2019).

[Hil21] J. Hilder, D. Pijn, O. Onishchenko, A. Stahl, M. Orth, B. Lekitsch, A. Rodriguez-Blanco, M. Müller, F. Schmidt-Kaler, and U. Poschinger, *Fault-tolerant parity readout on a shuttling-based trapped-ion quantum computer*, arXiv:2107.06368 (2021).

[Jam98] D. James, *Quantum dynamics of cold trapped ions with application to quantum computation*, Applied Physics B: Lasers and Optics **66**, 181 (1998).

[Kam14] A. A. Kamenski and V. D. Ovsiannikov, *Formal approach to deriving analytically asymptotic formulas for static polarizabilities of atoms and ions in Rydberg states*, Journal of Physics B: Atomic, Molecular and Optical Physics **47**, 095002 (2014).

[Kau17a] H. Kaufmann, T. Ruster, C. Schmiegelow, M. Luda, V. Kaushal, J. Schulz, D. von Lindenfels, F. Schmidt-Kaler, and U. Poschinger, *Scalable Creation of Long-Lived Multipartite Entanglement*, Physical Review Letters **119**, 150503 (2017).

[Kau17b] H. Kaufmann, T. Ruster, C. T. Schmiegelow, M. A. Luda, V. Kaushal, J. Schulz, D. von Lindenfels, F. Schmidt-Kaler, and U. G. Poschinger, *Fast ion swapping for quantum-information processing*, Physical Review A **95**, 052319 (2017).

[Kau20] V. Kaushal, B. Lekitsch, A. Stahl, J. Hilder, D. Pijn, C. Schmiegelow, A. Bermudez, M. Müller, F. Schmidt-Kaler, and U. Poschinger, *Shuttling-based trapped-ion quantum information processing*, AVS Quantum Science **2**, 014101 (2020).

[Kee19] A. Keesling, A. Omran, H. Levine, H. Bernien, H. Pichler, S. Choi, R. Samajdar, S. Schwartz, P. Silvi, S. Sachdev, P. Zoller, M. Endres, M. Greiner, V. Vuletić, and M. D. Lukin, *Quantum Kibble–Zurek mechanism and critical dynamics on a programmable Rydberg simulator*, Nature **568**, 207 (2019).

[Kel15] J. Keller, H. L. Partner, T. Burgermeister, and T. E. Mehlstäubler, *Precise determination of micromotion for trapped-ion optical clocks*, Journal of Applied Physics **118**, 104501 (2015).

[Kie02] D. Kielpinski, C. Monroe, and D. J. Wineland, *Architecture for a large-scale ion-trap quantum computer*, Nature **417**, 709 (2002).

[Kim96] H.-C. Kim, M.-H. Lee, J.-Y. Ji, and J. K. Kim, *Heisenberg-picture approach to the exact quantum motion of a time-dependent forced harmonic oscillator*, Physical Review A **53**, 3767 (1996).

[Kor83] H. J. Korsch and R. Mühlenkamp, *Field ionization of Rydberg atoms: A semiclassical treatment of complex energy states in intense electric fields*, Zeitschrift für Physik A Atoms and Nuclei **314**, 267 (1983).

[Kot14] S. Kotler, N. Akerman, N. Navon, Y. Glickman, and R. Ozeri, *Measurement of the magnetic interaction between two bound electrons of two separate ions*, Nature **510**, 376 (2014).

[Lab16] H. Labuhn, D. Barredo, S. Ravets, S. de Léséleuc, T. Macrì, T. Lahaye, and A. Browaeys, *Tunable two-dimensional arrays of single Rydberg atoms for realizing quantum Ising models*, Nature **534**, 667 (2016).

[Lei03] D. Leibfried, R. Blatt, C. Monroe, and D. Wineland, *Quantum dynamics of single trapped ions*, Reviews of Modern Physics **75**, 281 (2003).

[Li12] W. Li and I. Lesanovsky, *Electronically Excited Cold Ion Crystals*, Physical Review Letters **108**, 023003 (2012).

[Li13a] W. Li, A. W. Glaetzle, R. Nath, and I. Lesanovsky, *Parallel execution of quantum gates in a long linear ion chain via Rydberg mode shaping*, Physical Review A **87**, 052304 (2013).

[Li13b] W. Li and I. Lesanovsky, *Entangling quantum gate in trapped ions via Rydberg blockade*, Applied Physics B **114**, 37 (2013).

[Li21] W. Li, S. Wolf, L. Klein, D. Budker, C. E. Düllmann, and F. Schmidt-Kaler, *Robust Polarization Gradient Cooling of Trapped Ions*, arXiv:2109.00575 (2021).

[Mag54] W. Magnus, *On the exponential solution of differential equations for a linear operator*, Comm. Pure Appl. Math. **7**, 649 (1954).

[Mal15] K. M. Maller, M. T. Lichtman, T. Xia, Y. Sun, M. J. Piotrowicz, A. W. Carr, L. Isenhower, and M. Saffman, *Rydberg-blockade controlled-not gate and entanglement in a two-dimensional array of neutral-atom qubits*, Physical Review A **92**, 022336 (2015).

[Mar11] R. Marskar and U. Österberg, *Multilevel Maxwell-Bloch simulations in inhomogeneously broadened media*, Optics Express **19**, 16784 (2011).

[Met99] H. J. Metcalf and P. van der Straten, *Laser Cooling and Trapping*, Springer New York, 1999.

[Mok19] A. Mokhberi, J. Vogel, J. Andrijauskas, P. Bachor, J. Walz, and F. Schmidt-Kaler, *Determination of quantum defect for the Rydberg P series of Ca II*, Journal of Physics B: Atomic, Molecular and Optical Physics **52**, 214001 (2019).

[Mok20] A. Mokhberi, M. Hennrich, and F. Schmidt-Kaler, *Trapped Rydberg ions: A new platform for quantum information processing*, in: *Advances In Atomic, Molecular, and Optical Physics*, 233–306, Elsevier, 2020.

[Møl99] K. Mølmer and A. Sørensen, *Multiparticle Entanglement of Hot Trapped Ions*, Physical Review Letters **82**, 1835 (1999).

[Mol19] R. Moller, *Stabilisierung von Laserlichtquellen zur Anregung von Rydbergzuständen*, Bachelor's thesis, Johannes Gutenberg-Universität Mainz (2019).

[Mor00] G. Morigi, J. Eschner, and C. H. Keitel, *Ground State Laser Cooling Using Electromagnetically Induced Transparency*, Physical Review Letters **85**, 4458 (2000).

[Mü08] M. Müller, L. Liang, I. Lesanovsky, and P. Zoller, *Trapped Rydberg ions: from spin chains to fast quantum gates*, New Journal of Physics **10**, 093009 (2008).

[Nat15] R. Nath, M. Dalmonte, A. W. Glaetzle, P. Zoller, F. Schmidt-Kaler, and R. Gerritsma, *Hexagonal plaquette spin–spin interactions and quantum magnetism in a two-dimensional ion crystal*, New Journal of Physics **17**, 065018 (2015).

[Nie21] M. C. Niederländer, *Determination of Polarisabilities by Laser Spectroscopy of Rydberg Transitions in Trapped Ions*, Master's thesis, Johannes Gutenberg-Universität Mainz (2021).

[Nä00] H. Nägerl, C. Roos, H. Rohde, D. Leibfried, J. Eschner, F. Schmidt-Kaler, and R. Blatt, *Addressing and Cooling of Single Ions in Paul Traps*, Fortschritte der Physik **48**, 623 (2000).

[Oh89] H. G. Oh, H. R. Lee, T. F. George, and C. I. Um, *Exact wave functions and coherent states of a damped driven harmonic oscillator*, Physical Review A **39**, 5515 (1989).

[Ost99] A. Osterwalder and F. Merkt, *Using High Rydberg States as Electric Field Sensors*, Physical Review Letters **82**, 1831 (1999).

[Ovs11] V. D. Ovsiannikov, I. L. Glukhov, and E. A. Nekipelov, *Rates of blackbody radiation-induced transitions from Rydberg states of alkali atoms*, Journal of Physics B: Atomic, Molecular and Optical Physics **44**, 195010 (2011).

[Par15] H. L. Partner, R. Nigmatullin, T. Burgermeister, J. Keller, K. Pyka, M. B. Plenio, A. Retzker, W. H. Zurek, A. del Campo, and T. E. Mehlstäubler, *Structural phase transitions and topological defects in ion Coulomb crystals*, Physica B: Condensed Matter **460**, 114 (2015).

[Pau90] W. Paul, *Electromagnetic traps for charged and neutral particles*, Reviews of Modern Physics **62**, 531 (1990).

[Paw20] M. Pawlak and H. R. Sadeghpour, *Rydberg spectrum of a single trapped Ca$^+$ ion: A Floquet analysis*, Physical Review A **101**, 052510 (2020).

[Pen36] F. Penning, *Die Glimmentladung bei niedrigem Druck zwischen koaxialen Zylindern in einem axialen Magnetfeld*, Physica **3**, 873 (1936).

[Pij21] D. Pijn, O. Onishchenko, J. Hilder, U. G. Poschinger, F. Schmidt-Kaler, and R. Uzdin, *Detecting heat leaks with trapped ion qubits*, arXiv:2110.03277 (2021).

[Pog21] I. Pogorelov, T. Feldker, C. D. Marciniak, L. Postler, G. Jacob, O. Krieglsteiner, V. Podlesnic, M. Meth, V. Negnevitsky, M. Stadler, B. Höfer, C. Wächter, K. Lakhmanskiy, R. Blatt, P. Schindler, and T. Monz, *Compact Ion-Trap Quantum Computing Demonstrator*, PRX Quantum **2**, 020343 (2021).

[Pok20] F. Pokorny, C. Zhang, G. Higgins, and M. Hennrich, *Magic trapping of a Rydberg ion with a diminished static polarizability*, arXiv:2005.12422 (2020).

[Rac15] N. Rach, M. M. Müller, T. Calarco, and S. Montangero, *Dressing the chopped-random-basis optimization: A bandwidth-limited access to the trap-free landscape*, Physical Review A **92**, 062343 (2015).

[Rei02] D. Reiß, K. Abich, W. Neuhauser, C. Wunderlich, and P. E. Toschek, *Raman cooling and heating of two trapped Ba$^+$ ions*, Physical Review A **65**, 053401 (2002).

[Rit08] W. Ritz, *On a New Law of Series Spectra*, The Astrophysical Journal **28**, 237 (1908).

[Roo00] C. F. Roos, *Controlling the quantum state of trapped ions*, Ph.D. thesis, Leopold-Franzens-Universität Innsbruck (2000).

[Rus14] T. Ruster, C. Warschburger, H. Kaufmann, C. T. Schmiegelow, A. Walther, M. Hettrich, A. Pfister, V. Kaushal, F. Schmidt-Kaler, and U. G. Poschinger, *Experimental realization of fast ion separation in segmented Paul traps*, Physical Review A **90**, 033410 (2014).

[Rus17] T. Ruster, H. Kaufmann, M. Luda, V. Kaushal, C. Schmiegelow, F. Schmidt-Kaler, and U. Poschinger, *Entanglement-Based dc Magnetometry with Separated Ions*, Physical Review X **7**, 031050 (2017).

[Saf10] M. Saffman, T. G. Walker, and K. Mølmer, *Quantum information with Rydberg atoms*, Reviews of Modern Physics **82**, 2313 (2010).

[Saf11] M. S. Safronova and U. I. Safronova, *Blackbody radiation shift, multipole polarizabilities, oscillator strengths, lifetimes, hyperfine constants, and excitation energies in Ca$^+$*, Physical Review A **83**, 012503 (2011).

[Sch93] J. P. Schiffer, *Phase transitions in anisotropically confined ionic crystals*, Physical Review Letters **70**, 818 (1993).

[Sch18] V. M. Schäfer, C. J. Ballance, K. Thirumalai, L. J. Stephenson, T. G. Ballance, A. M. Steane, and D. M. Lucas, *Fast quantum logic gates with trapped-ion qubits*, Nature **555**, 75 (2018).

[Sed18] J. A. Sedlacek, J. Stuart, W. Loh, R. McConnell, C. D. Bruzewicz, J. M. Sage, and J. Chiaverini, *Method for determination of technical noise contributions to ion motional heating*, Journal of Applied Physics **124**, 214904 (2018).

[Sig17] A. Signoles, E. K. Dietsche, A. Facon, D. Grosso, S. Haroche, J. M. Raimond, M. Brune, and S. Gleyzes, *Coherent Transfer between Low-Angular-Momentum and Circular Rydberg States*, Physical Review Letters **118**, 253603 (2017).

[SK01] F. Schmidt-Kaler, J. Eschner, G. Morigi, C. Roos, D. Leibfried, A. Mundt, and R. Blatt, *Laser cooling with electromagnetically induced transparency: application to trapped samples of ions or neutral atoms*, Applied Physics B **73**, 807 (2001).

[SK11] F. Schmidt-Kaler, T. Feldker, D. Kolbe, J. Walz, M. Müller, P. Zoller, W. Li, and I. Lesanovsky, *Rydberg excitation of trapped cold ions: a detailed case study*, New Journal of Physics **13**, 075014 (2011).

[Sta14] J. Stark, *Beobachtungen über den Effekt des elektrischen Feldes auf Spektrallinien. I. Quereffekt*, Annalen der Physik **348**, 965 (1914).

[Sto21] F. Stopp, L. G. Ortiz-Gutiérrez, H. Lehec, and F. Schmidt-Kaler, *Single ion thermal wave packet analyzed via time-of-flight detection*, New Journal of Physics (2021).

[Ulm13] S. Ulm, J. Roßnagel, G. Jacob, C. Degünther, S. T. Dawkins, U. G. Poschinger, R. Nigmatullin, A. Retzker, M. B. Plenio, F. Schmidt-Kaler, and K. Singer, *Observation of the Kibble–Zurek scaling law for defect formation in ion crystals*, Nature Communications **4** (2013).

[Vit01] N. V. Vitanov, T. Halfmann, B. W. Shore, and K. Bergmann, *Laser-induced Population Transfer by Adiabatic Passage Techniques*, Annual Review of Physical Chemistry **52**, 763 (2001).

[Vog19] J. Vogel, W. Li, A. Mokhberi, I. Lesanovsky, and F. Schmidt-Kaler, *Shuttling of Rydberg Ions for Fast Entangling Operations*, Physical Review Letters **123**, 153603 (2019).

[Wal01] J. Walz, A. Pahl, K. Eikema, and T. Hänsch, *The first continuous coherent Lyman-$\alpha$ source*, Nuclear Physics A **692**, 163 (2001).

[Wal12] A. Walther, F. Ziesel, T. Ruster, S. T. Dawkins, K. Ott, M. Hettrich, K. Singer, F. Schmidt-Kaler, and U. Poschinger, *Controlling Fast Transport of Cold Trapped Ions*, Physical Review Letters **109**, 080501 (2012).

[WC17] J. Wong-Campos, S. Moses, K. Johnson, and C. Monroe, *Demonstration of Two-Atom Entanglement with Ultrafast Optical Pulses*, Physical Review Letters **119**, 230501 (2017).

[Wer74] G. K. Wertheim, M. A. Butler, K. W. West, and D. N. E. Buchanan, *Determination of the Gaussian and Lorentzian content of experimental line shapes*, Review of Scientific Instruments **45**, 1369 (1974).

[Wil10] T. Wilk, A. Gaëtan, C. Evellin, J. Wolters, Y. Miroshnychenko, P. Grangier, and A. Browaeys, *Entanglement of Two Individual Neutral Atoms Using Rydberg Blockade*, Physical Review Letters **104**, 010502 (2010).

[Wol19] S. Wolf, *Ion Crystals for Fundamental Research on Matter-Antimatter Symmetry and on Photon statistics*, Ph.D. thesis, Johannes Gutenberg-Universität Mainz (2019).

[Zha20] C. Zhang, F. Pokorny, W. Li, G. Higgins, A. Pöschl, I. Lesanovsky, and M. Hennrich, *Submicrosecond entangling gate between trapped ions via Rydberg interaction*, Nature **580**, 345 (2020).

[Zie13] F. Ziesel, T. Ruster, A. Walther, H. Kaufmann, S. Dawkins, K. Singer, F. Schmidt-Kaler, and U. G. Poschinger, *Experimental creation and analysis of displaced number states*, Journal of Physics B: Atomic, Molecular and Optical Physics **46**, 104008 (2013).

*Hans-Böckler-Str. 71*
*55128 Mainz*
☎ *+49 (0) 17638241716*
✉ *vogel@uni-mainz.de*

# Jonas Vogel

## Personal Information

| | |
|---|---|
| Date and place of birth | August 01, 1992, Köln, Germany |
| Nationality | German |
| Marital status | Single |

## Education and Academic Background

| | |
|---|---|
| since 04/2017 | **Ph.D. in Physics**, Johannes Gutenberg-Universität Mainz. |
| since 04/2017 | **Research Assistant**, Johannes Gutenberg-Universität Mainz. |
| 04/2019–06/2019 | **Research Assistant**, Universität Stockholm. |
| 10/2014–10/2016 | **Master of Science in Physics**, Universität Siegen. |
| 10/2011–07/2014 | **Bachelor of Science in Physics**, Universität Siegen. |
| 07/2011 | **General Higher Qualification for University Entrance**, Städtisches-Gymnasium Kreuztal. |

## Master's thesis

| | |
|---|---|
| Title | **Limits for X-ray nanowire diffraction with synchrotron radiation** |
| Supervisor | **Prof. Dr. Dr. Ullrich Pietsch** |
| Grade | **very good** |

## Bachelor's thesis

| | |
|---|---|
| Title | **Untersuchung zur temperaturabhängigen Interdiffusion in einem [CoFeB/Mn/CoFeB/MgO] Schichtsystem mittels pnCCD** |
| Supervisor | **Prof. Dr. Dr. Ullrich Pietsch** |
| Grade | **very good** |

## Publications

**Precision measurement of the ionization energy of a single trapped $^{40}$Ca$^{+}$ ion by Rydberg series excitation**
J. Andrijauskas, J. Vogel, A. Mokhberi and F. Schmidt-Kaler
*Phys. Rev. Lett.* ***127****, 203001 (2021)*

**Shuttling of Rydberg ions for fast entangling operations**
J. Vogel, W.Li, A. Mokhberi, I. Lesanowsky and F. Schmidt-Kaler
*Phys. Rev. Lett.* ***123****, 153603 (2019)*

**Determination of quantum defect for the Rydberg P series of Ca II**
A. Mokhberi, J. Vogel, J. Andrijauskas, J. Walz and F. Schmidt-Kaler
*J. Phys. B* ***52****, 214001 (2019)*